Sol-gel routes to nanostructured bifunctional catalysts for the direct conversion of (bio)ethanol to 1,3-butadiene

Denis D. DOCHAIN

Thèse présentée en vue de l'obtention du grade de docteur en sciences agronomiques et ingénierie biologique

Faculté des Bioingénieurs

UCLouvain

Examining board :

Prof. Damien DEBECKER (UCLouvain)	Supervisor
Prof. Eric GAIGNEAUX (UCLouvain)	Chairperson
Prof. Michel Devillers (UCLouvain)	Secretary
Prof. Stéphanie LAMBERT (ULiège, Belgium)	
Prof. Mickael CAPRON (Université de Lille, Françe)	
Dr. Ales STYSKALIK (Masaryk University, Czech Republic)	

REMERCIEMENTS

I would like to start off by thanking my supervisor and the main contributor to this work, Damien. From the numerous courses he gave when I was a student to the comments and corrections he suggested in this document, he has always been a true inspiration and motivation anchor for me. His professionalism, his immense knowledge combined with kindness and true leadership set for me the standards to surpass myself and finish this PhD thesis.

Furthermore, I would like to express my gratitude to all the members of the jury for their advice and inputs during the PhD and the private defence that undoubtedly helped improved the quality of this document. Special thanks to Professor Michel Devillers for the time he took from his busy schedule to discuss in-depth chemical behaviour that helped me understand key concepts for this work.

I want to warmly thank Ales for his guidance throughout these five years. From teaching me the basics of non-hydrolytic sol-gel during my master thesis to showing me around the Czech countryside, I deeply cherish these memories and I'm honoured to have worked alongside him. Moc vám děkuji, příteli! My thanks also go to the researchers at Masaryk University for their good humour and warm welcome during my research trips to Brno. It was an amazing experience to collaborate and interact with all the people there.

Of course, I also want to thank all the people from the C2 and C3 lab: Damien, Eric, Françoise, Nathalie, François, Jean-Charles, Arnaud, Christine, Margot, Fanny, Juliette, Sophie, Hippolyte, Sebastian, Marty, Giovanni, Valentin, Corentin, Aurélien, Noé, Ali, Plaifa, Maximiliano, Isaac, Ian, Cédric, Alexis, Benjamin. The working atmosphere is just unmatched, and I recognize how lucky I am to have experienced such chemistry. From a professional point of view, I was amazed to witness every day for five years the collaboration and mutual aid everyone displayed. Huge thanks to François and Jean-Charles for their daily good mood and immense expertise. In a research environment, I value this immensely and it cannot be overlooked.

And naturally, I cannot forget about all the extra time we all spent together, from the good laughs during the lunches to the many drinks we had after work at the Cabane (Onlywood in our hearts forever). Special thanks to Fanny, Hippolyte, Marty and Margot for those weekends at De Haan and Hatrival and all those special Jeudredi moments.

D’un point de vue plus personnel, je remercie tous les potes du bachelier de Ciney. Je retiens cet esprit de camaraderie et cette bonne ambiance constante qui ont régné pendant ces 3 ans et qui continuent jusqu’à aujourd’hui. Je remercie particulièrement Carine Hansenne qui m’a motivé et convaincu de faire une passerelle vers un master universitaire. Je ne serai indéniablement pas là actuellement sans ses enseignements et ses conseils !

Parlant de ce master universitaire, je remercie aussi tous les potes de bioingénieurs. L’ambiance survoltée des soupers de cours restent des souvenirs incroyables de ces années de Master. Je retiens aussi les parties endiablées de Mario Kart au Croustikot, les apéros ensoleillés sur notre terrasse home-made et ces nombreux weekends passés à bosser sur nos mémoires ou nos stages. Merci à Gaétane, Margaux, Marion, Arnaud et Corentin pour ces moments !

Bien sûr, je remercie chaleureusement Caroline, François, Antoine, Tanguy et Maxime pour leur longue amitié et soutien important depuis tant d’années. Toutes nos soirées jeux de société, weekends randonnées et voyages remplis de bons moments et de discussions super intéressantes sont autant de bons souvenirs que je chéris particulièrement.

Ensuite, je souhaite remercier ma famille, qui a fait preuve d’un soutien infaillible pendant l’entièreté de mes études supérieures, malgré mon parcours plus que tumultueux. De mes échecs en BAC1 jusqu’à l’annonce de l’obtention de la bourse FRIA, mes grands-parents, mes parents et mon frère ont toujours été présents pour m’encourager, me soutenir, m’écouter, me remotiver et bien sûr me féliciter. Ils restent pour moi un exemple d’implication et de passion du travail et je leur dois énormément.

And last but not least, un immense merci à Margot. Merci pour sa compréhension, son écoute et sa patience durant ces années de thèse. Nos longs échanges (scientifiques ou pas) m’ont toujours remis sur la bonne voie et effacé ces doutes ou incertitudes que je pouvais avoir. Elle a toujours réussi à faire en sorte que je donne le meilleur de moi-même en toutes circonstances et ce document n’aurait probablement pas vu le jour sans ce boost constant mais nécessaire. C’est un véritable cadeau d’avoir quelqu’un avec qui partager autant de moments de qualité. Des discussions sérieuses et existentielles jusqu’aux fous rires dont nous seuls avons le secret, ces moments sont pour moi inoubliables et inestimables.

ABSTRACT

Heterogeneous catalysis can become the pivotal point to shift from petro-based to renewable bio-based resources as feedstocks for those chemical processes. 1,3-butadiene, a key monomer in the tyre industry, attracts a lot of research attention due to a fore coming market instability. In parallel, the production of bioethanol is expected to reach 150 billion litres in 2032. Thus, the catalytic conversion of ethanol to 1,3-butadiene is under extensive research. To maximize the industrial viability, the synthesis of these catalysts must be straight-forward and should consist of as few steps as possible. Furthermore, the ethanol-to-butadiene reaction requires bifunctional catalysts with highly dispersed Lewis acid sites and metal nanoparticles as redox sites. These challenges are discussed in this thesis and addressed via the use of innovative sol-gel techniques.

In the first half of this thesis, an aerosol-assisted sol-gel approach is used to synthesize Ag-Ta and Cu-Ta-based catalysts with advantageous mesoporous texture preventing mass transfer limitations, inserted Ta atoms inside the silica matrix serving as Lewis acid sites and well dispersed small Ag or Cu nanoparticles as redox sites. Understanding the catalyst properties and tuning them allow us to obtain remarkable catalytic performance.

In the second half, the non-hydrolytic sol-gel approach is leveraged for the synthesis of Cu-Ta-based catalysts. First, two different synthesis routes, the ether route and the acetamide elimination route, are compared to better understand the active sites speciation, their proximity and the influence of those characteristics on catalytic properties. The acetamide elimination route is deemed more appropriate for the ethanol-to-butadiene reaction. The mixing of both routes in a so-called “delayed addition” of a fraction of precursors yield bifunctional materials with properties originating from both distinct synthesis routes and reasonable catalytic performance.

TABLE OF CONTENTS

CHAPTER 1: GENERAL INTRODUCTION

GENERAL INTRODUCTION

1.1 Context

Heterogeneous catalysis currently occupies a central place in our modern society. The vast majority (ca. 90 %) of chemical processes in our industrial world relies on heterogeneous catalysts. With the climate change related challenges and the demonstrated responsibility of the petrochemical industry in this matter, the field of heterogeneous catalysis can now become more than ever the driving force of this industrial shift from petro-based resources to renewable bio-based resources as feedstocks for chemical processes.

To make this shift possible, new and effective heterogeneous catalysts must be designed. In addition to their catalytic performance, the synthesis process must be straight-forward and should involve as few steps as possible. The combination of an easy and short synthesis process and an effective performance would maximize the chances of a heterogeneous catalyst viable at an industrial scale.

More specifically, the production of 1,3-butadiene, a pivotal monomer in the tyre and nylon industry, is currently dominated by the steam cracking of naphtha, a heavily polluting and energy consuming process. Furthermore, the emergence of shale gas and its cracking is believed to bring insecurity and instability over the 1,3-butadiene market, from a supply and pricing point of view.[1] Thus, these two elements justify the ongoing intensive research on an alternative sustainable production pathway.

A notable solution might be to use bioethanol as a feedstock for its catalytic conversion to 1,3-butadiene. As its production is already applied at an industrial scale,[2] the supply of bioethanol is expected to increase in the coming years all around the world due to political incentives, making it an ideal candidate to complement or even supplant the steam cracking process.[3] Consequently, catalysts development for the ethanol-to-butadiene has witnessed an increased appeal in the academic research world over the last 15 years.[4-6]

A common ground found in the scientific literature is the need for a bifunctional catalyst combining both acid and redox active sites with open textural properties to run the ethanol-to-butadiene reaction.[7] However, current best catalysts have long and intricate synthesis procedure or simpler procedures that limit the control on key factors like active sites dispersion. Hence the need for an easy to apply, straight-forward approach that would

allow the synthesis of such a catalyst in a one-pot fashion, with an extensive control on the determining properties of the active material.

The framework of this thesis is thus the development of innovative synthesis techniques that can combine all these requirements to synthesize a catalyst with high selectivity towards our product of interest and high stability all along the reaction process.

1.2 1,3-Butadiene as a crucial C4 platform chemical for the industry

1.2.1 1,3-Butadiene in modern society

The polymer industry is constantly evolving, facing numerous challenges in the current transition to a more sustainable society. More specifically, the tyre and nylon sectors heavily depend on 1,3-butadiene (BD) as a monomer.[8] Figure I.1 describes the repartition of BD final purpose in 2015, vastly composed of polymers and resins. Among them, styrene butadiene rubber (SBR), polybutadiene rubber (PBR) and acrylonitrile butadiene styrene resins (ABS) account for almost 70 % of the BD derivatives and are mainly used by the automotive industry. Other BD applications are summarized in Table I.1 With such a high contribution to the automotive industry, the demand towards BD is expected to gradually increase with the projected increase of car ownership in the coming years.[1,9]

The global production of butadiene is rising steadily and sat at around 12,000 kT in 2015.[3] In 2021, the 1,3-butadiene market was valued at around 35 billion USD and is forecasted to reach 56 billion USD by 2029, which translates to a Compound Annual Growth Rate of 6.0 % for the 2022-2029 period.[1] BD market is currently driven by 3 factors: diversity in industrial applications, rapid industrialization in developing countries and the constantly increasing demand in styrene-butadiene rubber.[1] Out of those 3 sectors, the automotive industry and more specifically the tyres manufacturing is expected to drive this growth during the forecast period.[1]

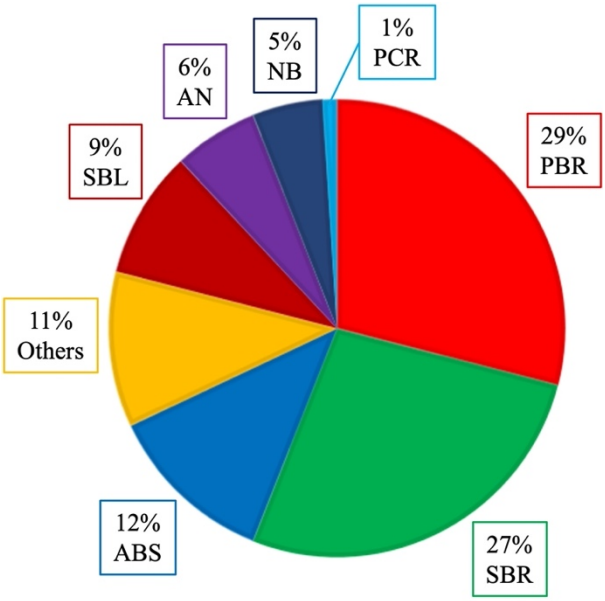

Figure I.1: Repartition of 1,3-butadiene uses in the polymer industry.[9] Abbreviations are detailed in Table I.1.

Table I.1: Main 1,3-butadiene applications in the polymer industry.[9]

Abbreviation	Full Name	Applications
PBR	Polybutadiene Rubber	Tyres, plastics
SBR	Styrene Butadiene Rubber	Tyres, rubber articles
ABS	Acrylonitrile Butadiene Styrene Resins	Auto parts, telephones, office machines
SBL	Styrene Butadiene Latex	Foam Rubber, adhesives, sealants
AN	Adiponitrile	Nylon resins, fibers, fabrics
NB	Nitrile Rubber	Hoses, fuel lines, autopats
PCR	Polychloroprene Rubber	Gloves, coating, adhesives, tyres
Others		Lube oil additives, auto parts, medical devices

1.2.2 Butadiene in history

Butadiene, a key monomer in the manufacture of synthetic rubber, has attracted the attention of the scientific community since first being isolated by Caventou in 1863.[10,11] However, its structure was only elucidated in 1895 by Ciamician and Magnaghi, leading to an increased attention drawn to this compound.[10,11] Notably, Lebedev discovered its potential to be converted into rubber-like polymers in 1910, which initiated significant research endeavours in this field.[12-14]

GENERAL INTRODUCTION

During the Second Industrial Revolution (1870–1914), the vulcanization of natural rubber was the main means of elastomer production. Although natural rubber offers several advantages, its properties cannot be controlled and tailored. This led the scientific community to develop synthetic rubber, especially in countries without rubber plantations. In contrast to natural rubber, the characteristics of these rubbers can be adjusted to meet specific requirements (i.e. temperature resistance, abrasion, strength). Although Armstrong and Miller discovered butadiene in the products of petroleum cracking in 1886, gaseous ethanol has always been the primary feedstock for the early manufacture of polybutadiene rubber. The pioneering work by Nef (1901) and Ipatiev (1903) reported the conversion of ethanol to butadiene using different catalysts.[15,16] Later, Ostromislensky's used a mixture of ethanol and acetaldehyde to achieve industrially viable yields (1915).[17] Following these discoveries, the work of Lebedev on $ZnO–Al_2O_3$ catalysts, reported in a 1928 patent, eventually led to large-scale 1,3-butadiene industrial processes.[15] Both technologies were applied industrially: the Ostromislensky process in the USA and the Lebedev process in the Soviet Union.[15] The two technologies will be described more in-depth in Section 1.4.1.

During World War II, rubber shortages posed a significant threat to the Allies victory, surpassing steel, aluminium, and gasoline in strategic importance. Consequently, the United States heavily invested in synthetic rubber research.[14,18-20] The American government initiated a synthetic rubber program in 1939, collaborating with industry and academia to expand the U.S. synthetic rubber industry. In this context, the catalytic conversion of ethanol to butadiene gained prominence to meet the demand for this crucial monomer. Researchers at the Carbide and Carbon Chemicals Corporation and the Mellon Institute played a key role in advancing the research for the ethanol-to-butadiene reaction. Pioneering work on high-throughput catalyst screening, process optimization, and mechanistic studies paved the way for efficient butadiene production from ethanol.[19,20] By the end of the war, the U.S. had built three plants with a combined yearly production capacity of 220,000 tons of butadiene.[15]

After World War II, the production of less expensive butadiene from oil cracking rendered the ethanol route obsolete.[8] Simultaneously, scientific interest in the ethanol-to-butadiene reaction declined, and publications on the subject were sparse from the 1960s to the 2000s.[21-26] However, in recent years, economic and environmental factors have reignited interest in the development of bio-based production processes, and thus on the ethanol-to-butadiene reaction, described as a renaissance by Angelici *et al.*[27] A 2011

publication by Jones *et al*.'s is considered as a significant milestone in this resurgence, shedding light on the reaction mechanism and presenting more efficient catalysts for butadiene production.[28] Furthermore, the petroleum cracking now faces a tense situation with the growing exploitation of other cracking feedstocks such as shale gas in North America and liquefied petroleum gas in Europe.[9,29,30] Since these alternatives feedstocks produce much lower proportions of butadiene, their exploitation will increase the instability in the butadiene market. These constrains on the butadiene (BD) market are the main reasons why alternative (more sustainable) ways of producing this important C4 platform chemical are needed.

The historical development of butadiene production, from early discoveries to World War II applications and the shift towards petroleum cracking, has shaped the research landscape for the catalytic conversion of ethanol to butadiene. To this day, the petrochemical industry still represents the predominant way of butadiene production.

1.2.3 Petro-based 1,3-butadiene

Butadiene is commonly produced by three processes: (i) steam cracking of paraffinic hydrocarbons (as a co-product of ethylene manufacturing); (ii) catalytic dehydrogenation of *n*-butane and *n*-butene (Houdry process); and (iii) oxidative dehydrogenation of *n*-butene (Oxo-D or O-X-D process).[3]

- Steam cracking of naphtha

The vast majority (ca. 95%) of the global butadiene production comes from the steam cracking of naphtha (Scheme I.1), where BD is a co-product of ethylene production.[4]

During the steam cracking process, naphtha is fed to a pyrolysis furnace where they are “cracked” at temperatures around 800 °C.[31] This process produces pyrolysis products composed of hydrogen, ethylene, propylene, butadiene and other co-products. The pyrolysate is then quenched to remove the heavy fractions; compressed to remove the C5s and higher components; and then dried. The resulting mixture goes through a series of distillation tanks to separate the hydrogen, methane, ethane, ethylene, propane and propylene from the crude C4s or crude butadiene (containing mainly 1,3-butadiene with other C4s such as isobutylene and butenes). On

average, the BD yield is estimated around 4.5 wt.%, meaning that 22.2 tons of naphtha are required to produce 1 ton of BD.[3,32]

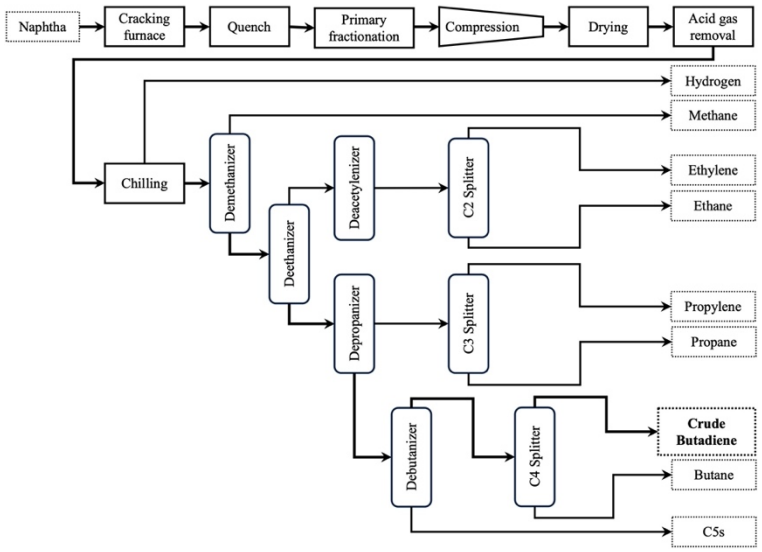

Scheme I.1: Process scheme of the steam cracking of naphtha, adapted from Haribal *et al*.[33]

- Catalytic dehydrogenation of *n*-butane and *n*-butene (Houdry process)

The Houdry process consists of the conversion of *n*-butane to *n*-butenes and butadiene (Eq. 1 and 2) over a Cr/Al_2O_3 catalyst that operates between 600 and 680 °C and between 0.15 and 0.20 atm.[34,35] Scheme I.2 describes the different steps of the Houdry process for the on-purpose production of butadiene.

$$C_4H_{10} \rightarrow C_4H_8 + H_2 \quad \text{(Eq. 1)}$$

$$C_4H_8 \rightarrow CH_2 = CHCH = CH_2 + H_2 \quad \text{(Eq. 2)}$$

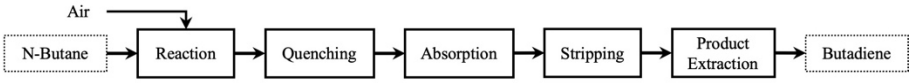

Scheme I.2: Process scheme of the Houdry process.[34]

- Oxidative dehydrogenation of *n*-butene (Oxo-D process)

Scheme I.3 summarizes the Oxo-D process, where a mixture of steam, air and *n*-butenes is converted (Eq. 3) over a catalyst at low pressure

(between 0.2 and 2 atm) and at 500–600 °C.[34,35] Typical catalysts used in this process include iron oxide with bauxite or chromium oxide and calcium-nickel phosphate stabilized with chromium oxide.[34,35]

$$C_4H_8 + \frac{1}{2}O_2 \rightarrow CH_2 = CHCH = CH_2 + H_2O \qquad \text{(Eq. 3)}$$

Scheme I.3: Process scheme of the Oxo-D process.[34]

As explained above, BD is traditionally obtained through the steam cracking of naphtha as a by-product of ethylene production.[34] Since ethylene is considered the most important olefin in the world, its output maximisation remains the priority for crackers in the near future, hence the emergence of alternative lighter feedstocks such as shale gas that intrinsically yields a smaller BD-ethylene production ratio compared to naphtha. Indeed, shale gas typically contains between 4 and 10 vol % of ethane.[36,37] In fact, the weight ratio butadiene/ethylene sits at around 0.02 for ethane cracking, compared to 0.13 for naphtha cracking or even 0.26 for gas oil cracking (Figure I.2).[8,30] This difference could lead to a further unbalance in the BD market. As a result, BD shortages and price increases will become more and more likely in the future, leading to a potential need for plants for the on-purpose synthesis of BD.

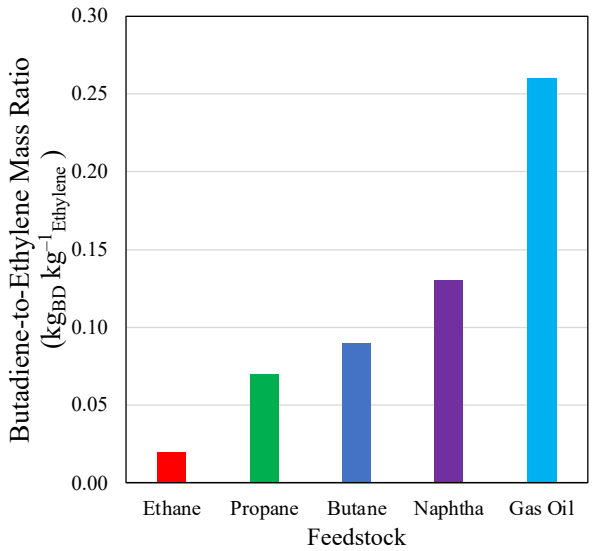

Figure I.2: Butadiene-to-ethylene mass ratio for different petro-based feedstocks.[12,38]

Furthermore, the steam cracking process is characterised by an extremely high energy consumption (8 % of the worldwide consumed energy

in 2015) and responsible for the release of more than 180 million tons of CO_2.[7,32,39,40] Recent report from IPPC has showed us how urgent it is to reduce our greenhouse gas emissions to face climate change and limit the global warming to 2 °C by 2050,[41] further fuelling the need for sustainable and on-purpose production of BD.

1.2.4 Alternative 1,3-butadiene production pathways

The catalytic conversion of some C4 alcohols, such as 1-butanol, 2-butanol, 1,3-, 2,3-, 1,4-, and 1,2-butanediols, represent viable alternative paths to produce BD. These alcohols already have a C4 skeleton, which eliminates the need for a C-C bond formation, and could be the most suitable raw materials for the synthesis of BD. Conveniently, these C4 alcohols can all be produced from biomass via microbial fermentation processes.[42-44] Cobalt Technologies, which has developed a fermentation platform for biobutanol claimed that 1-butanol became a good alternative to obtain butadiene.[45,46] Thus, there would be a great prospect to produce BD from butanols.[45]

- Dehydration of 1,3-butanediol into 1,3-butadiene

1,3-butanediol (1,3-BDO) can be produced via biocatalytic hydrogenation of 4-hydroxy-2-butanone (4H2B)[42] or by the catalytic hydrogenation of 4H2B over a modified Raney Ni catalyst.[47]

For the conversion of 1,3-BDO to BD, Table I.2 summarizes the most active catalysts developed in recent years,[48-50] with the generally accepted reaction mechanism depicted on Scheme I.4. Overall, better performance are achieved at reaction temperatures above 350 °C,[48] and heavily depend on the quality and quantity of acid sites, ideally targeting Bronsted sites of medium strength.[50-52]

Table I.2: Recent catalytic systems active in the conversion of 1,3 butanediol to 1,3-butadiene.

Catalyst	T (°C)	WHSV (h^{-1})	TOS (h)	$X_{1,3\text{-BDO}}$ (%)	Y_{BD} (%)	$P_{1,3\text{-BD}}$ ($g_{1,3\text{-BD}}$ g_{cat}^{-1} h^{-1})
$Y_2Zr_2O_7$[48]	375	0.4	30	100	87	0.21
H-ZSM-22[49]	300	1.39	10	95	65	0.54
ZSM-5[50]	300	0.23	8	>95	60	0.083

WHSV = Weight Hourly Space Velocity (h^{-1}) ; TOS = Time-on-stream (h)

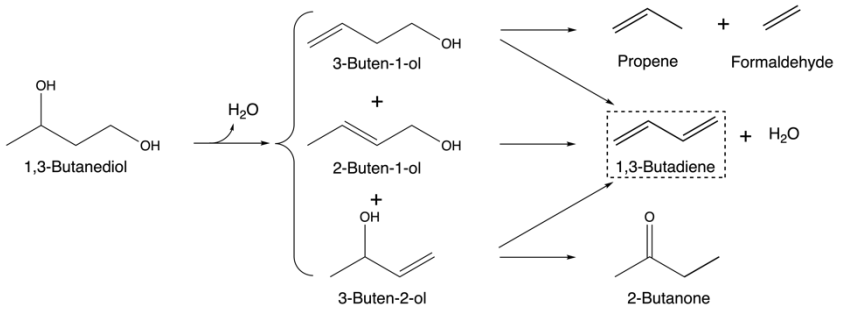

Scheme I.4: Reaction mechanism of the conversion of 1,3-butanediol to 1,3-butadiene.[49,51]

- Dehydration of 2,3-butanediol into 1,3-butadiene

Recently, attention towards the production of 2,3-BDO is increasing thanks to its large number of industrial applications.[42,53] Microbial production of 2,3-BDO from sugars has been known for more than 100 years and high yields to 2,3-BDO have been reported.[8,54,55]

Table I.3 gives a sample of how 2,3-BDO can be converted into BD by catalytic dehydration using silica-supported H_3PO_4 derivatives, notably modified with Cs[56] or other alkali metals such as Na and K.[57] More exotic metals such as Yb have been tested, although poor catalytic performance were obtained.[58] The mechanism of the reaction is straight-forward and is depicted on Scheme I.5.

Table I.3: Recent catalytic systems active in the conversion of 2,3-butanediol to 1,3-butadiene.

Catalyst	**T (°C)**	**WHSV (h^{-1})**	**TOS (h)**	**$X_{1,3\text{-BDO}}$ (%)**	**Y_{BD} (%)**	**$P_{1,3\text{-BD}}$ ($g_{1,3\text{-BD}}$ g_{cat}^{-1} h^{-1})**
CsH_2PO_4[56]	400	0.99	8	100	92	0.55
Sc_2O_3[59]	411	0.4	10	100	80	0.19
γ-Al_2O_3[60]	350	2.37	–	99	21	0.30

WHSV = Weight Hourly Space Velocity (h^{-1}) ; TOS = Time-on-stream (h)

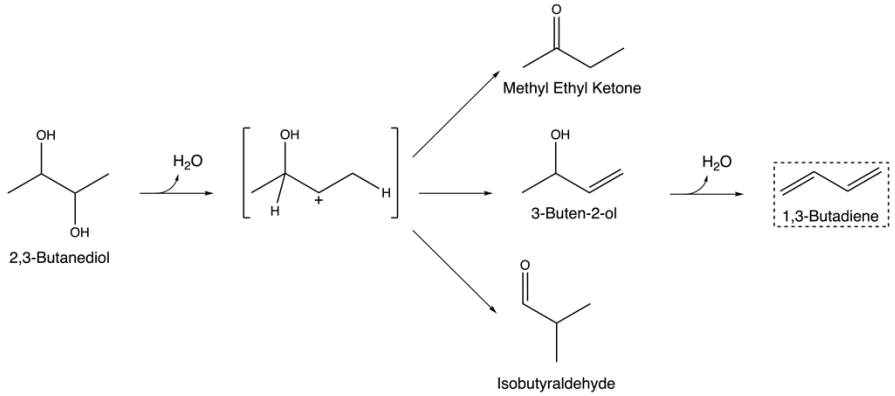

Scheme I.5: Reaction pathway for the conversion of 2,3-butanediol to 1,3-butadiene.[53,56]

Although these alternatives can seem attractive from a sustainability point of view, they are not yet feasible at an industrial scale. The economic viability of the dehydration of 2,3-butanediol was assessed by Song *et al.* In their work, they estimated that such process at the industrial scale would only be viable at a 2,3-butanediol cost below 0.991 $/kg – which can currently not be attained with the fermentation process to bio-based C4.[61]

1.3 Why use bioethanol?

Bio-based feedstocks are currently emerging as attractive candidates to substitute the current petro-based resources in various industrial processes. In this matter, bioethanol is of particular interest, as it holds great potential to be further transformed into BD.[3,62-65] It is noted that ethanol can be synthesized via direct hydration of ethylene, but represents a minor fraction (less than 7 % in 2012).[66,67]

1.3.1 Production methods

Already well established in the industrial landscape, bioethanol is obtained from the fermentation of agricultural biomass.[3,68] Currently, starch and sugar crops account for about 60% and 40% of ethanol production, respectively.[2] By region, corn is the main industrial feedstock in the USA, sugar cane in Brazil and sugar beet in Europe.[2,63]

Bioethanol can be used in the pharmaceutical (as disinfectant), the automotive (as biofuel) and chemical industry (as solvent and feedstock). Due

to government incentives to promote biofuels, the bioethanol production is already implemented at the industrial scale. The global supply ranges in 100s of billions of litres annually and is projected to grow in the coming years.[3] More precisely, the production of bioethanol reached 120 billion litres in 2017 and is expected to rise above 130 billion litres by 2024 (Figure I.3).[3] Recent numbers for the 2020-2022 period from the Organization for Economic Cooperation and Development (OECD) and the Food and Agriculture Organization (FAO) showed a worldwide estimated production of 124 billion litres, dominated by North and South America.[2] The same organisations predicted an increase up to 150 billion litres produced in 2032 mainly in the Americas, Asia and Europe, or an annualized increase of 1.4 %, resulting from the increase in biofuel needs.[2,3] Indeed, the current contribution of biofuel in the ethanol consumption sits at 81.1 % and as projected for 2032, this contribution will remain stable and reach 82.9 %.[2]

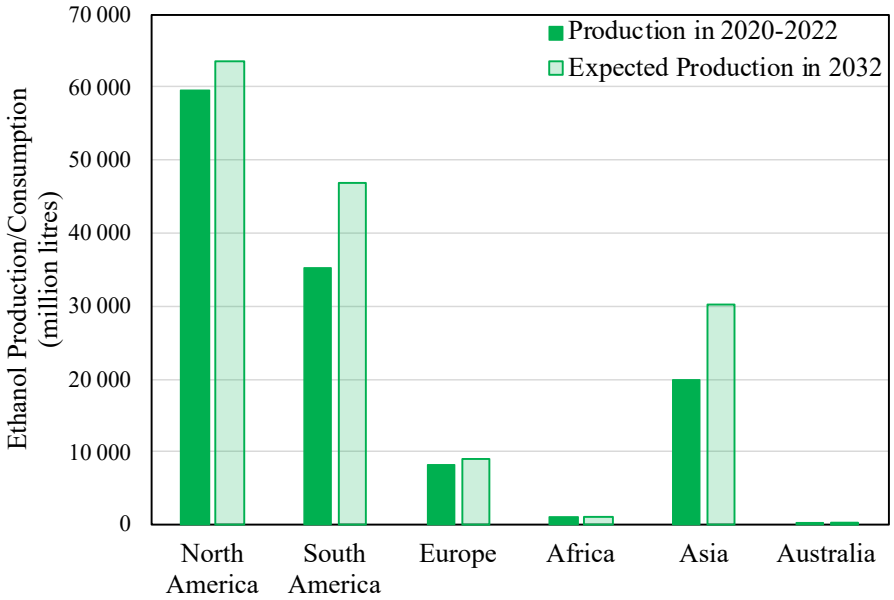

Figure I.3: Ethanol production in the different continents and prediction for 2032.[2]

However, industrial bioethanol production has issues: certain crops optimized for bioethanol production need energy and water to cultivate, while other crops compete for food.[69] Moreover, despite being well documented, further knowledge, improvements and insights are discovered through additional research on ethanol production.[63,69] Due to the high contribution of the feedstock price to the cost of the overall process (70-90%), many research were conducted to test different feedstocks.[70-73]

1.3.2 Ethanol as a platform molecule

Bioethanol is one of the most attractive bio-based chemical, listed among the 10 priority-biobased products from biorefinery carbohydrates by the US Department of Energy.[74] The high number of applications (Scheme I.6) makes this “platform chemical” a very interesting candidate towards petrochemical independence.[74,75] For example, ethylene – which can easily be obtained by ethanol dehydration[76,77] – is a typical drop-in chemical and can be used for example to produce bio-based polyethylene or ethyl acetate (a vastly used food enhancer).[77] Another interesting reaction is the conversion of ethanol to butanol via the Guerbet reaction, which is used in biofuels.[75,78] In this thesis, the focus will be on the catalytic upgrading of bioethanol to butadiene which has attracted a lot of attention in the recent years.[3,5-7,79-83]

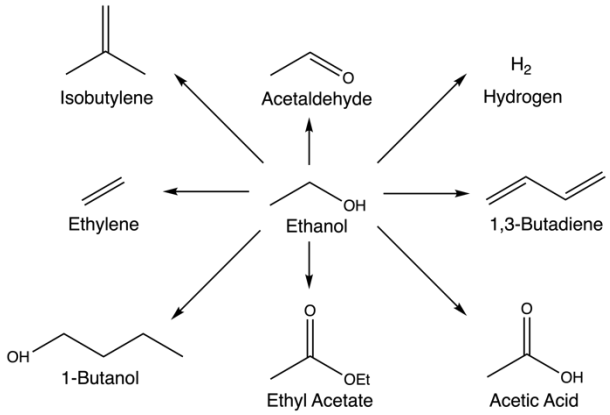

Scheme I.6: Major bulk chemicals derived from ethanol.[27]

1.4 Catalytic conversion of ethanol to 1,3-butadiene

1.4.1 Historical aspect (Ostromislensky + Lebedev)

As explained in Section 1.2.1, BD industrial production first started through the catalytic conversion of ethanol via the Ostromislensky process and the Lebedev process before the Second World War. Also called the two-step process and the one-step process respectively, they were applied throughout the USA and the Soviet Union respectively. The two-step process, based on two fixed bed reactors placed in succession, first produces acetaldehyde from ethanol and then produces BD from a mixture of ethanol and the newly produced acetaldehyde. On the other hand, the one-step process directly converts ethanol to BD (Scheme I.7).

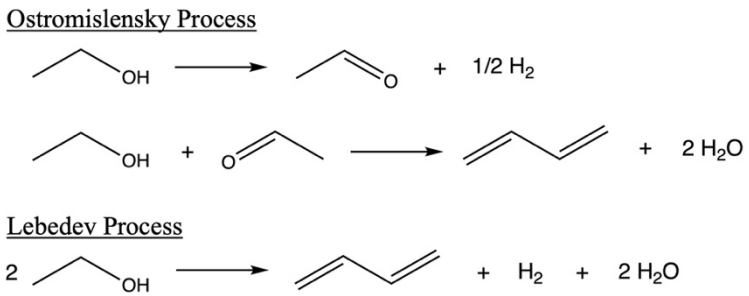

Scheme I.7: Reaction scheme of the Ostromislensky and Lebedev processes.[3]

An in-depth work from Cespi *et al.* studied different “sustainability indicators”, the Cumulative Energy Demand, the Carbon footprint, the Water depletion, the Single score (macro factors) and the Economic Index. These parameters were distinctively studied in different regions of the world (North America, Brazil and European Union) and similar conclusions were reached in all these areas: the Lebedev process reaches lower environmental and economic burdens compared to Ostromislensky, and both processes are deemed preferable to the steam cracking.[3] It is noteworthy to mention that in Asia, the sustainable alternatives are considered to be not competitive yet due to the high ethanol price in these regions.[2,3] Furthermore, this study considers typical temperatures of the Lebedev process around 400 °C. For the Ostromislensky process, the first step takes place between 260 and 330 °C and the second step between 320 and 350 °C.[3]

In this work, the focus was brought on the Lebedev process, i.e. the one-step conversion of ethanol to butadiene for its industrial advantage over the Ostromislensky process from an environmental and economic point of view.[3] Indeed, the development of processes that involve a limited number of steps is more attractive from an industrial perspective as it eliminates the numerous purification steps and the costs and time associated with them.

1.4.2 Reaction Mechanism

To correctly understand the requirements for the catalysts design, elucidating the reaction mechanism of the ethanol-to-butadiene reaction is essential. In the literature, the Ostromislensky and Lebedev processes are generally acknowledged to follow the Toussaint-Kagan pathway (Scheme I.8).[84-91] Historically, Gorin and Jones suspected the exact same sequence of reactions, starting with acetaldehyde and providing ethanol only for the Meerwein-Ponndorf-Verley (MPV) reduction step.[92] Such reaction sequence is known to proceed in several steps.

The first step in the Toussaint-Kagan mechanism is the non-oxidative dehydrogenation of ethanol to acetaldehyde, typically obtained over redox active sites such Cu, Ag, Zn or Fe nanoparticles.[84,93-99] Even noble metals like Au and NiAu alloys have been tested.[100] Intense research efforts are being made to develop effective alcohol dehydrogenation catalysts, because acetaldehyde is itself a valuable platform chemical.[101,102] Yet, for the ethanol-to-butadiene (ETB) reaction, there are other requirements for the catalyst to be able to complete the next steps of the reaction scheme, up to BD.

In the second step, acetaldehyde undergoes an aldol condensation to acetaldol. This step has often been described as the rate limiting step between 300 and 400 °C when considering Lewis acidic mixed oxide catalysts from periodic group 4 and 5.[84,85,87,103-110] For example, Lewis acid sites formed by Hf(IV) and Zr(IV) are known to be active in the aldol condensation,[98,108,111-113] Historically, Ta and Zr have been extensively described as the most suited transition metals for this step.[7,18,81,85,86,98,99,104,106-109,113-120] Atomically, this step is thought to be catalysed by so-called Lewis open sites, i.e. isolated atoms in a tetrahedral position connected to three Si–O– groups and one OH moiety.[84,85,106,121]

The third step is the acetaldol dehydration to crotonaldehyde. It is known to never be limiting since acetaldol is never observed in the analysed products.[84,85,109,122] The fourth step is the MPV reduction, involving ethanol

and crotonaldehyde to produce acetaldehyde and crotyl alcohol. Similar to the aldol condensation, Lewis acid sites specifically catalyse this step.[111,112,123]

Finally, the last dehydration of crotyl alcohol to BD is straight-forward and is not recognized as the rate limiting step.[93,105,111,124,125]

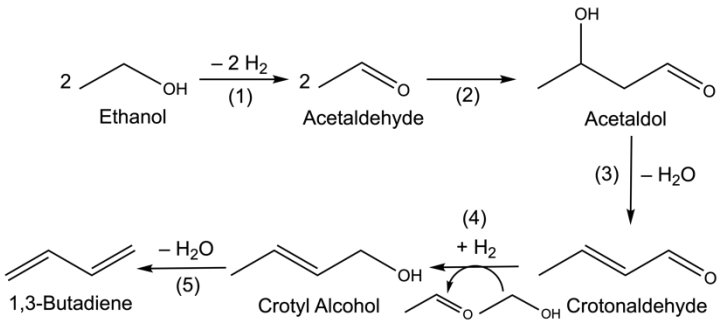

Scheme I.8: Toussaint-Kagan pathway for the ethanol-to-butadiene reaction, taken from Dochain *et al*.[126] This reaction cascade takes place in 5 steps: (1) Non-oxidative dehydrogenation of ethanol (EtOH) to acetaldehyde (AA); (2) condensation of two AA molecules into 3-hydroxybutanal (acetaldol); (3) acetaldol dehydration to crotonaldehyde; (4) production of crotyl alcohol and AA via a Meerwein-Ponndorf-Verley (MPV) reduction with ethanol; (5) dehydration of crotyl alcohol to butadiene.[7,127]

All in all, the Toussaint-Kagan mechanism provides us insights to design an effective catalyst for the ETB reaction, mainly the need for a bifunctional catalyst combining both redox properties and acidic properties.

In terms of by-products possibly produced in the one-step conversion of ethanol to butadiene, ethylene (EY) and diethylether (DEE) are the main ones. Due to the necessary presence of Lewis acid sites for the aldol condensation and the MPV reduction, ethanol can also be directly dehydrated on these sites to yield EY and DEE. It can be noted that the formation of EY is favoured at higher temperatures, due to the decomposition of DEE into EY.[7,128] More generally, dehydration by-products are expected at higher reaction temperatures.[7,128,129] Next to dehydration by-products, ethyl acetate (EtOAc) originates from the Tishchenko reaction between 2 molecules of acetaldehyde.[128] Propylene and pentadienes can also be produced through the MPV reduction or aldol condensation of acetone and formaldehyde, themselves obtained by retroaldol addition of 4-hydroxy-butan-2-one.[130,131] Finally, different variants of butenols can come from crotyl alcohol rearrangement or tautomerisation.[128,132]

The repartition between 1,3-butadiene and the different by-products depicted in the reaction mechanism are dependent on the reaction conditions. Increasing the weight hourly space velocity (WHSV) decreases the overall

ethanol conversion, BD selectivity and increases the acetaldehyde selectivity.[120,133] In opposition, when the WHSV is decreased, the BD selectivity is boosted, in conjunction with a drop in acetaldehyde selectivity.[7,133] To the best of our knowledge, only one example in the literature claimed no influence of the contact time on the BD selectivity.[134] The catalytic performance of Zr-based catalysts was shown to be directly correlated with the reaction temperature.[129] Although BD selectivity tends to remain constant from 673 K to 723 K, higher EtOH conversions are responsible for an increase in BD yields and thus productivity.

Apart from the Toussaint-Kagan mechanism, we must also take into the account the fact that another mechanism has been proposed by the research group of Cavani, based on research carried out on basic MgO catalysts (Scheme I.9).[128,135,136] Although with regard to acid catalysts, the universally accepted mechanism remains the Toussaint-Kagan pathway.[6]

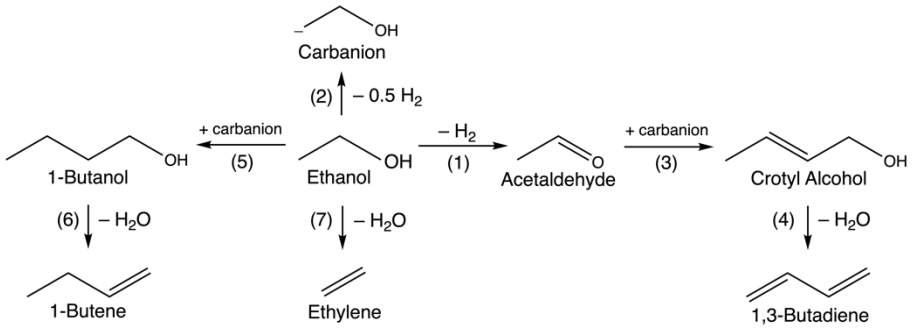

Scheme I.9: Cavani pathway for the ethanol-to-butadiene reaction.[128,135,136] Here, ethanol is believed to be either (1) dehydrogenated into acetaldehyde and hydrogen, or (2) deprotonated into carbanionic species supposedly stabilized by Mg cations. This carbanion can then (3) react with acetaldehyde to form crotyl alcohol, which is (4) dehydrated into butadiene. In some cases, (5) ethanol can also react with the carbanion to form 1-butanol, which can be (6) dehydrated to 1-butene. More simply, (7) ethanol can lose its hydroxyl group and can be dehydrated into ethylene.

1.4.3 Influence of reaction conditions on catalytic performance

- Influence of the reaction temperature

Different operating parameters can be tuned to optimize the catalyst performance.[108,113,133,137] First, the temperature has a direct impact on the overall ethanol conversion; it is positively correlated with the temperature.[108,112,137] But temperature also has a large impact on the products distribution.[113] The formation of ethylene and diethylether, dehydration by-products, is preferred at higher temperatures.[7,113,117,128,129,137] However, BD does not follow the same trend.[113] Below the optimal temperature (dependent on the catalyst), high acetaldehyde selectivity is usually observed, indicating a slow rate for the aldol condensation step, reducing the amount of BD.[113]

- Influence of the weight hourly space velocity

The influence of the space velocity logically has an opposite effect on ethanol conversion, relative to temperature: the higher the space velocity, the lower the contact time and thus the lower the ethanol conversion.[113] Dehydration by-products are not significantly correlated with space velocity. On the contrary, the acetaldehyde selectivity continuously increases with the space velocity,[113] due to the fact that the aldol condensation becomes too slow at high flow rates.[133] Coke formation (and thus the deactivation of the catalyst) can also be dependent on the contact time: the higher the contact time (low space velocity), the higher the coke formation.[134]

- Influence of the water content in the ethanol feed

Another important aspect to control in the ETB reaction, is the water content in the ethanol feed. Cepsi *et al*. discussed this point by stating the importance for a sustainable and viable industrial plant to be able to work efficiently with diluted ethanol as feed, reducing or even removing the need for ethanol purification after fermentation.[3] With this objective in mind, many research groups tackled this issue.[109,137] The overall ethanol conversion tends to decrease with the water content.[137] In Hf-Zn-based catalysts, water was suggested to adsorb on Hf^{4+} Lewis acid sites active in the aldol condensation, blocking this step.[137] However, this effect can be mitigated by increasing the reaction temperature.[137] By increasing the reaction temperature in Hf-Zn systems in the presence of aqueous ethanol, the BD yield increases with the water content. Authors justify this behaviour by the diminished likelihood of consecutive aldol condensations leading to heavy coke-like by-products since

water is partially adsorbed on Hf^{4+} active sites responsible for those. [137,138] Concurrently, blocking the undesired consecutive aldol condensation decreases coke formation and thus increases the catalysts stability.[137] Butenes yields follow the same trend as BD, since their formation also rely on the aldol condensation of two acetaldehyde molecules.[137,139] EY and DEE yields increase with the water content, due to the replacement of Lewis acid sites by Bronsted acid sites by the chemisorption of water molecules.[137] On Zn-ZrSi catalysts, H_2O was suggested to adsorb on Lewis acid sites active in the aldol condensation, resulting in lower EtOH conversion, lower BD selectivity and higher AA selectivity.[104,109,129] In the case of a Hf-Zn catalyst, water chemisorption on Zn^{2+} active sites suppresses their ability to produce acetaldehyde and therefore enhances the probability of generating EY and DEE.[137]

Interestingly, the addition of La in Zr-Zn-Si-Beta catalysts has proven to mitigate the deactivating effect of water by inhibiting the interaction of water vapor with surface oxygen which typically generates hydroxyl groups responsible for ethanol dehydration.[109] This had the effect of suppressing direct ethanol dehydration and promoting ethanol dehydrogenation, another reason for improved BD production (Table I.4).[109] Another similar phenomenon was observed on Zr-Cu-MTW where it was observed that ethanol dehydrogenation sites were more resistant to water adsorption than the aldol condensation sites.[98]

Table I.4: Promoting effect of metals on catalytic performance in aqueous ethanol.

Catalyst	% EtOH (in H_2O)	X_{EtOH} (%)	$S_{1,3\text{-BD}}$ (%)	$Y_{1,3\text{-BD}}$ (%)	$P_{1,3\text{-BD}}$ ($g_{1,3\text{-BD}}$ g_{cat}^{-1} h^{-1})
Zr-Zn-Si-Beta[109]	80	73	46	34	0.20
	50	55	36	20	0.12
La-Zr-Zn-Si-Beta[109]	80	83	61	51	0.30
	50	60	50	30	0.18

1.4.4 Deactivation mechanism

Extensive studies over Zn-Y/Beta catalyst have helped clarify the deactivation mechanism: the acetaldehyde produced in the first step of the reaction mechanism is the main precursor of all coke deposits that can form through a succession of aldol condensations and cyclization reactions (Figure I.4).[138] Other research confirmed this theory by observing an accumulation of

acetaldehyde in the reaction products causing fast deactivation by rapid coking, decreasing the ethanol conversion.[120,134,140]

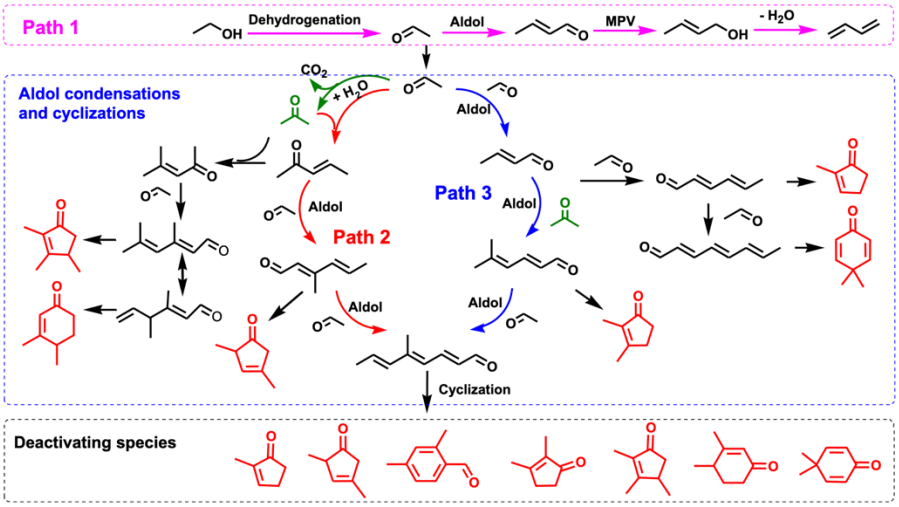

Figure I.4: Deactivation mechanism proposed by Yan et al., reproduced with authorization.[138]

Wang *et al.* further investigated the coke deposition phenomenon responsible for the decrease in both ethanol conversion and butadiene selectivity.[108] More precisely, acetaldehyde and crotyl alcohol are believed to undergo cross-aldol condensation followed by reduction and dehydration to form heavier by-products, covering the catalysts active sites.[105,108,138] On Y-Zn-Cu-SiBEA, coke is shown to partially cover Zn species, deactivating the catalyst.[134]

Study of spent catalysts showed in some cases that coke deposited preferentially in materials with low mass transfer efficiency and low accessibility (e.g. microporous catalysts), increasing the chance of formation of heavier coke-like by-products.[108]

It is worth noting, however, that in numerous cases, the catalytic performance could be recovered after an in-situ regeneration treatment, for example under oxygen (i.e. the burning of the deposited coke).[81,108,109,113,141]

However, another possible deactivation mechanism has also been described. In Zn-SiBEA catalysts, the redox active sites were shown to be altered during reaction, as zinc migrates from the SiBEA matrix to form less active surface oxide clusters.[134] This type of catalyst deactivation logically

leads to slower rates in the first step of the reaction (ethanol dehydrogenation to acetaldehyde). Moreover, in this case, catalysts can not be re-activated by a simple thermal treatment.

1.4.5 Heterogeneous catalysts for the ETB reaction

- Active elements

Since both redox sites and acid sites are required to produce 1,3-butadiene directly from ethanol, the choice of metals combination for the synthesis of a bifunctional catalyst is wide. Table I.5 summarizes a critical selection of recent and relevant scientific literature reports.

In terms of catalysts formulations, acidic transition metal oxide-based catalysts such as Ta, Zr, Nb, Hf or Y promoted with nanoparticles of Ag, Cu or Zn have been extensively described (Table I.5). Out of this series, the 3 most productive catalysts are Ta-Zn-TUD-1, Zr-Zn-KIT-6 and Y-Zn-SiBEA, with BD productivities above 2 $g_{1,3\text{-BD}}$ g_{cat} h^{-1}.[115,120,141] The only common trait out of all these catalysts is the presence of Zn, as active site for the acetaldehyde production. Otherwise, Lewis acidic metals and silica-based supports are all different. To be noted, these highly productive catalysts are tested above 400 °C and high space velocities (between 5.3 and 9.5 h^{-1}). Current literature tends to study the ETB reaction at reactions temperatures around 325-350 °C to minimize operating costs and WHSV around 0.5-1 h^{-1} to maximize BD selectivity (Table I.5). Across highly productive catalysts, common traits required to achieve exceptional performance are mentioned such as high dispersion and high proximity between the two types of active sites, a finely tuned acidity to mitigate by-products and a predominantly mesoporous support to limit deactivation and mass transfer limitations.[115,120,141]

Although Zn is the common point among the most productive catalysts (Table I.5), a study of Si-BEA by Kyriienko *et al.* in 2017 concluded that Cu associated with Ta was the most selective combination for BD production, compared to Ta-Zn and Ta-Ag.[114] Authors attributed this difference to the presence of strong Lewis acid sites originating from the incorporation of Zn atoms in the zeolite matrix, yielding ethylene to the detriment of the BD.

In this research, the focus was brought on Ta. Historically, Ta was identified as the most active element in the two-step conversion of ethanol to butadiene (Ostromislensky process),[18,106,131,142] and has also been the subject of theoretical investigations to study the chemistry and configurations of this

element in different environments.[85,143] Next to Ta, Ag and Cu were added to the composition of the bifunctional catalyst, as they showed superior performance in numerous research in acetaldehyde production from ethanol.[102,144-146] Combining these elements would be in alignment with our objective to maximize BD selectivity while maintaining a reasonably high productivity and stability.

Table I.5: Literature sample of transition metals combinations used in the one-step conversion of ethanol to 1,3-butadiene.

Catalyst	T° (°C)	WHSV (h^{-1})	X_{EtOH} (%)	$S_{1,3\text{-BD}}$ (%)	$Y_{1,3\text{-BD}}$ (%)	$P_{1,3\text{-BD}}$ ($g_{1,3\text{-BD}}\ g_{cat}^{-1}\ h^{-1}$)
Ta-Ag-SiBEA[114]	325	0.5	83	76	63	0.18
Ta-Cu-SiBEA[114]	325	0.5	88	83	73	0.21
Ta-Zn-SiBEA[114]	325	0.5	52	83	43	0.13
Ta-Zn-TUD-1[120]	400	5.3	94	73	69	2.13
Ta-Ag-SiO_2[7]	355	1.1	65	22	14	0.09
Ta-Cu-SiO_2[7]	355	1.1	75	41	31	0.20
Ta-Cu-SiO_2[126]	325	1.1	82	74	60	0.39
Zr-Ag-SiBEA[107]	320	3.0	15	59	8.9	0.16
Zr-Zn-KIT-6[115]	425	9.5	95	52	49	2.49
Zr-Zn-Silicalite-1[108]	350	0.38	90	61	55	0.12
Zr-Cu-MCF[116]	400	3.7	92	70	64	1.39
Zr-Zn-TUD-1[113]	400	0.38	85	62	53	0.31
Zr-Cu-MTW[98]	375	0.50	81	68	55	0.16
Zr-Zn-La-Si-Beta[109]	350	1.0	83	61	51	0.30
Hf-Cu-Zn-SiO_2[111]	400	0.64	99	72	72	0.26
Hf-Zn-SiO_2[111]	400	0.64	99	70	69	0.25
Hf-Cu-SiO_2[137]	360	1.1	88	44	39	0.23
Y-Zn-Beta[122]	350	1.0	78	63	49	0.29
Y-Zn-Beta[138]	350	1.0	95	62	59	0.35
Y-Cu-Zn-SiBEA[134]	375	1.0	98	66	65	0.40
Y-Zn-SiBEA[141]	400	7.9	82	63	52	2.33

- Importance of active sites configuration

DFT measurements on Zr-β zeolite distinguished so-called “closed sites” and “open sites”.[147] “Closed sites” were characterized by the linkage of an isolated zirconium atom with four oxygen bridges to Si atoms, essentially forming a closed $(Si–O)_4$–Zr cage, whereas the “open sites” possess one OH moiety replacing a Si linkage ($(Si–O)_3$–Zr–OH).[147,148] It was discovered that open sites in Zr-β demonstrated improved catalytic performance compared to the closed sites. Zhang *et al*. explain this difference by the presence of the Zr–OH bond, lowering the energy barrier for the aldol condensation step, the rate-limiting step.[147]

For Ta, XRD, FTIR, DRUV and EXAFS (extended X-ray adsorption fine structure) measurements corroborated by DFT calculations, have allowed proposing its potential configurations in BEA zeolites (Scheme I.10).[85,143] Out of these configurations, Ta(IV) (Scheme I.10, b) supposedly catalyses aldol condensation, MPV and further dehydration steps whereas Ta(V) (Scheme I.10, a and c) might be less effective.[120] Control on those configurations is not discussed but could depend on the zeolite framework, the Ta precursor or the synthesis conditions (temperature, aging time).

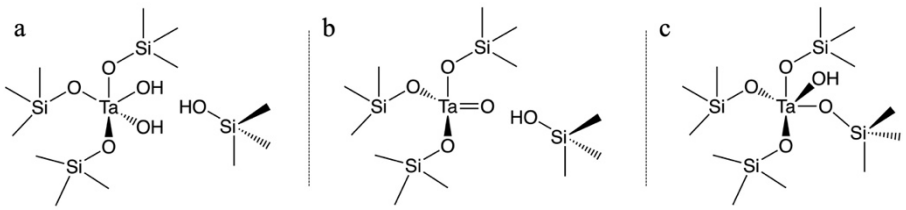

Scheme I.10: Ta possible configurations in BEA zeolites, adapted from Müller *et al*.[85]

Another study in 2010 used computational models to extrapolate 10 different Ta environments within a BEA zeolite.[143] They concluded that the most stable structure was a pentahedral Ta(V) featuring one Ta–OH bond and four Ta–O–Si bonds, providing both Lewis acid and basic sites (Scheme I.11).

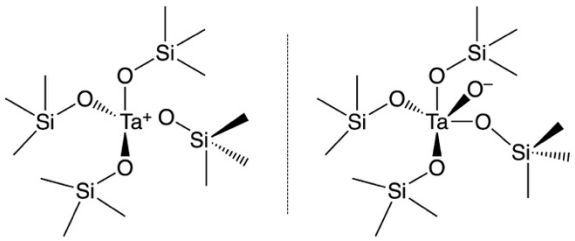

Scheme I.11: Most stable Ta configuration in BEA zeolites according to Tielens *et al.*[143]

- Effect of promoters

The addition of La in Zr-Zn-based formulations was shown to increase the overall ethanol conversion and the BD selectivity (Table I.6).[104,109] Authors explained this phenomenon by the decrease in acetaldehyde selectivity observed with the increase of La loading in the catalyst, suggesting that La species promoted the aldol condensation step.[109] A direct link was made with the improved basicity of the Zr-Zn-La catalyst (specifically weak basicity).[109] Furthermore, it is believed that La also help avoid the adsorption of water on Lewis acid sites, active in the MPV reduction, indirectly promoting this part of the reaction cascade.[104,109]

Table I.6: Effects of promoters on catalytic performance.

Catalyst	T° (°C)	WHSV (h^{-1})	X_{EtOH} (%)	$S_{1,3\text{-}BD}$ (%)	S_{AA} (%)	$P_{1,3\text{-}BD}$ ($g_{1,3\text{-}BD}$ g_{cat}^{-1} h^{-1})
Zr-Zn-Si-Beta[109]	350	1.0	73	46	28	0.20
La-Zr-Zn-Si-Beta[109]	350	1.0	83	61	15	0.30
Zr-Zn-SiO_2[112]	400	1.0	95	41	16	0.23
Na-Zr-Zn-SiO_2[112]	400	1.0	94	47	22	0.25
Cs-Zr-Zr-SiO_2[112]	400	1.0	98	56	16	0.32

- Importance of the support

Larina *et al.* studied La-Zr-Zn-Si oxide catalysts, prepared from a series of silica materials.[119] The research showed that, besides obvious differences in textural properties, quantity and strength of acid sites could be tuned by switching between different silica supports. These differences in acidic behaviours influenced significantly the BD selectivity of the resulting catalyst, although no quantification of acid sites was presented.[119]

In 2017, Zn-Y catalysts were studied on different supports and their catalytic activity compared (Table I.7).[141] The superiority of Beta zeolites in the BD productivity is undeniable, with more than a 3 fold increase in productivity compared to MCM-41 or commercial silica. Authors highlighted the close proximity between the two types of active sites under the form of Zn–Y-containing clusters in a three-dimensional zeolite cage.[141] The positive effect of proximity between active sites has also been demonstrated in a number of other studies, interpreted in terms of increased chance for the different intermediates to react with each other.[111,122]

Table I.7: Influence of support on catalytic performance on Y-Zn catalysts.[141] Catalysts contain 5 wt.% of Y and Zn. Reaction conditions: T=350 °C, WHSV=1.3 h^{-1}.

Catalyst	X_{EtOH} (%)	$S_{1,3\text{-}BD}$ (%)	$Y_{1,3\text{–}BD}$ (%)	$P_{1,3\text{-}BD}$ ($g_{1,3\text{-}BD}$ g_{cat}^{-1} h^{-1})
Y-Zn-SiO_2	56	28	16	0.12
Y-Zn-MCM-41	61	32	20	0.15
Y-Zn-Beta	95	69	66	0.50

- Importance of texture

A recent study on La-Zr-Zn-Si oxide catalysts tested numerous supports with very different textural properties and it was shown that in the case of the considered catalytic system, porosity, pore size distribution and specific surface area were not a determining factor in the direct catalytic conversion of aqueous ethanol into BD (Table I.8).[119]

Table I.8: Influence of silica support and textural properties on La-Zr-Zn-Si oxide catalytic performance. Reaction conditions: 375 °C, WHSV=0.40 h^{-1}, 80 wt.% ethanol in water. [119]

Catalyst	S_{BET} (m^2 g^{-1})	V_p (cm^3 g^{-1})	X_{EtOH} (%)	$S_{1,3\text{-}BD}$ (%)	$Y_{1,3\text{-}BD}$ (%)	$P_{1,3\text{-}BD}$ ($g_{1,3\text{-}BD}$ g_{cat}^{-1} h^{-1})
La-Zr-Zn-KSKG	260	0.82	58	68	39	0.093
La-Zr-Zn-A-175	160	0.80	64	66	42	0.098
La-Zr-Zn-A-380	205	1.08	46	61	28	0.066
La-Zr-Zn-SBA-15	340	0.81	49	63	31	0.073
La-Zr-Zn-MCM-41	615	0.46	61	57	35	0.082
La-Zr-Zn-MCM-48	380	0.69	69	45	31	0.072
La-Zr-Zn-MCF	355	1.15	55	48	26	0.062
ZnLa-Zr-SiBEA	570	0.59	67	35	23	0.055

However, another study stated the opposite, since higher BD yields were obtained with silica with higher specific surface area.[117] Concurrently, the BD selectivity can also be increased with the pore size of the catalyst.[28,116] Authors attributed the catalytic stability to the large and uniform pore size.[116,120] All in all, materials with open texture are better performing in the ethanol-to-butadiene and the synthesis technique should be able to control the textural properties of the resulting catalyst.

- Importance of synthesis techniques

The conditions in which catalysts are synthesized are often significant as they can greatly influence their physico-chemical properties. Most bifunctional catalysts are synthesized using preformed supports impregnated with the active elements.[98,112,120,128] Interestingly, the simultaneous impregnations of both active elements provided better performance and stability then separate impregnations followed by mechanical mixing.[111]

The control in the synthesis process is especially primordial for zeolites. As an example, Larina *et al*. were able to increase the number of surface acid sites in Zr-Cu-MTW only by increasing the amount of HF used in the synthesis process.[98]

One of the most active catalysts in the Lebedev process to date has been synthesized and studied by Pomalaza *et al*.[120,149] Comparing Ta-Zn catalysts on three different matrixes – TUD-1 silica, dealuminated BEA zeolites and fumed silica –, it was shown that TUD-1 obtained by sol-gel chemistry had the best BD productivity (Table I.9). It was discovered that the BD selectivity was directly correlated to the acid sites surface concentration, itself directly influenced by the synthesis technique used. Here, sol-gel chemistry was deemed superior compared to zeolites and pre-formed silica in terms of acidity and thus performance. Other research does also acknowledge the advantage of yielding mesopores in zeolites to increase activity.[98,108,118]

Table I.9: Influence of synthesis technique on catalysts texture, acidity on catalytic performance in the ETB reaction.[120] Reaction conditions: T=400 °C; WHSV=5.3 h^{-1}.

Catalyst	S_{BET} ($m^2\ g^{-1}$)	Acid Sites (mmol m^{-2})	X_{EtOH} (%)	$S_{1,3\text{-}BD}$ (%)	$Y_{1,3\text{-}BD}$ (%)	$P_{1,3\text{-}BD}$ ($g_{1,3\text{-}BD} \cdot g_{cat}^{-1}\ h^{-1}$)
Ta-Zn-TUD-1	640	563	94	73	69	2.13
Ta-Zn-deBEA	500	213	95	59	56	1.74
Ta-Zn-SiO_2	185	30	94	48	45	1.40

However, the synthesis of zeolites suffers from several drawbacks. First, the hydrothermal crystallization usually relies on the use of hydrogen fluoride (HF), a toxic and very corrosive compound that is not only harmful to the environment but also dangerous to manipulate. Moreover, in a typical synthesis procedure, the ageing time can last as long as 30 days, making the preparation of such catalysts time and resource consuming.[107,150] Furthermore, zeolites usually show diffusion limitations, which can negatively affect the catalytic performance.[107] The microporous zeolitic channels caused steric hindrance resulting in poor elements dispersion in the cages nests.[107] Another issue is the limited metal loading of the final material. Finally, the formation of large zeolite particles limits the molecular diffusion within the pore structure.[151]

1.4.6 Take-aways in relation to the present research

Based on the different results described in the former section, there is a clear need to develop new and effective synthesis pathways to obtain bifunctional catalysts for the ETB reaction. Considering the drawbacks associated with zeolites and the requirements highlighted for a good ETB catalyst (large pores, abundant acid sites, active sites proximity, etc.), we believe that it is of great interest to investigate more in depth the potential of the sol-gel chemistry to design such materials. Indeed, the sol-gel approach is a powerful tool for the preparation of a wide range of functional materials from nanoparticles to hybrid materials. Applicable in various solvents, the bottom-up reaction between the precursors can yield a solid with many different compositions and high homogeneity in certain conditions. Thus, with the objective to obtain highly active ETB catalyst, we put forward that sol-gel chemistry may offer unique tools to target: (i) the correct insertion of the metal in the silica matrix to bring the Lewis acid sites, (ii) the formation of small metal nanoparticles that serve as redox active species and (iii) the control on the spatial organisation in these catalyst, to bring the two active species in close proximity.

However, classical sol-gel routes also suffer some specific limitations (mostly related to the control of the composition, the homogeneity and the texture, as explained in further details in section 1.5.1). Thus, in this PhD thesis, the focus is put on the development of peculiar sol-gel processes (see sections 1.5.3 and1.5.4) that were selected for their putative ability to circumvent these limitations and produce tailored catalytic formulations which could turn highly active in the ETB reaction.

In terms of active metals, the state of the art above also allow making strategic choices. Historically, tantalum was the most effective element in the Ostromislensky process.[18,131,142] More recent research has also shown the superiority of this element in the ETB reaction,[7,81,85,106,114,120] although we also acknowledge the good results obtained with other transition metals, such as Zr, Hf and Y. Regarding the redox active species, Ag and Cu are the most common metals and Cu has shown on numerous studies its superiority compared to other metals with redox properties.[7,114,118,134,152,153]

The choice of elements and the ecological and economic context stated in this introduction also has to be put into perspective with the scarcity of the studied metals.[154] Figure I.5 gives the relative abundance of every element in the periodic table, highlighting the fact that almost all metals currently studied in the ethanol-to-butadiene reaction are classified under the category “Serious threat in the next 100 years”, meaning that their supply is highly questioned.[155] Therefore, an additional effort should be made to develop effective, stable and ideally reusable catalysts with low metal loadings and a synthesis procedure with a low economic and environmental burden. As this study focuses on Ta, Ag and Cu, these issues must be considered in the perspective of an industrial application. Here, the current most productive catalysts in the literature either contain Ta-Zn or Zr-Zn, all of them categorised as “serious threat in the next 100 years” or “Rising threat from increased use” (Figure I.5). Even though Zn could be suitable in an industrial application, other metals also active in the ETB reaction should thus be preferred, such as Cu. While Ta is chosen in the current work for the reasons explained above, we note that alternative acidic metal oxides (e.g. Nb, Zr) should be considered as well. In future works, it is noted that all the promoters studied in Table I.6 are considered as “Plentiful supply” and their addition to a catalysts formulation in order to diminish the transition metal loading should be extensively studied.

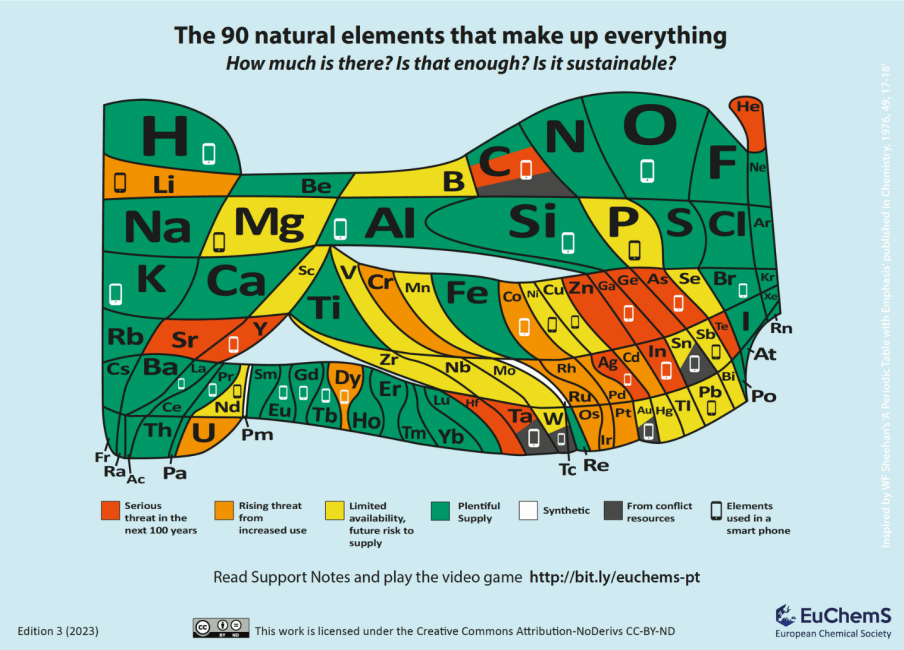

Figure I.5: Element Scarcity Periodic Table developed by the European Chemical Society, 2023 version.[155]

1.5 Obtaining a bifunctional catalyst through sol-gel chemistry

1.5.1 Sol-gel principles

Sol-gel chemistry offers various ways to customize the characteristics of porous materials, and in particular of solid catalysts.[156,157] Sol-gel approaches can be described as bottom-up preparation methods in which the solid is obtained via a succession of reactions between molecular precursors (Figure I.6).[156] In the most typical sol-gel routes, alkoxide or chloride or carboxylate precursors are put in solution and allowed to hydrolyse and then poly-condense in a controlled manner (Scheme I.12). Upon peptidisation, the solution turns into a sol and then reticulates to form a wet gel which usually undergoes subsequent steps of ageing, drying and calcination.

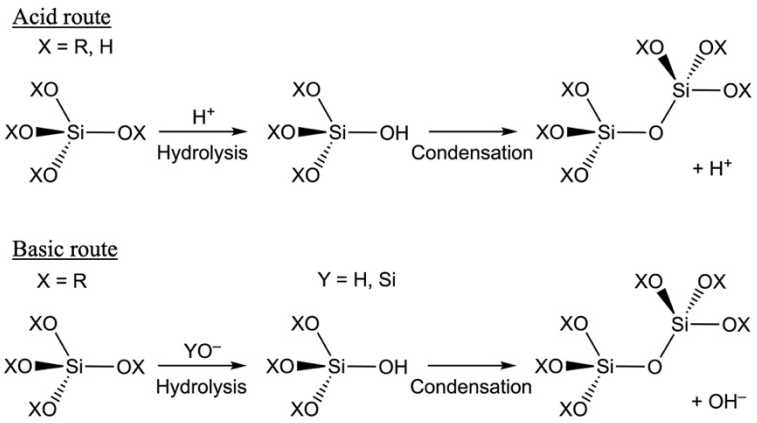

Scheme I.12: Chemical reactions representing the basis of sol-gel chemistry in acid and basic medium, adapted from Rex *et al.*[158]

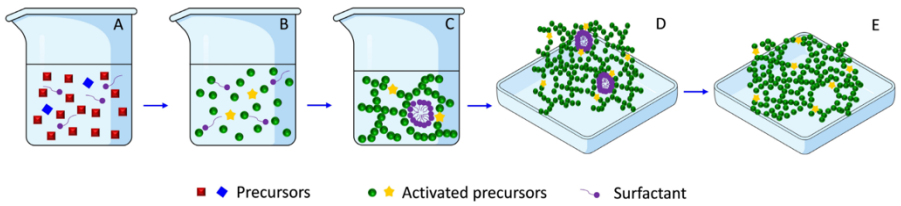

Figure I.6: Reaction steps in classical sol-gel chemistry, adapted from Debecker *et al.*[156] (A) molecular precursors solution; (B) activation of those precursors by hydrolysis or organolysis; (C) polycondensation of activated precursors to form a wet gel; (D) gel ageing and drying; (E) thermal treatment to remove residuals and consolidate the molecular network.

By manipulating reaction conditions, precursor properties, solvent, and by incorporating additives such as reactivity modifiers and sacrificial pore-generating agents, a wide range of ad-hoc formulations can be produced. These formulations can be fine-tuned in terms of composition, surface chemistry, porosity, etc.[156,159,160] However, two main challenges in classical sol-gel synthesis apply to the preparation of heterogeneous catalysts.

1.5.2 Sol-gel chemistry: limitations

The first limitation of sol-gel routes for the preparation of porous heterogeneous catalysts is related to the control on the composition and on the homogeneity of the solid. Indeed, the success of the method is restricted to the cases where all precursors are soluble in the same medium and react with similar hydrolysis and condensation rates. Otherwise, the resulting material will face homogeneity problems with clusters of different molecular compositions.

The second challenge is related to the control on the texture, which obviously needs to be controlled precisely for heterogeneous catalysts. When the solvent is evaporated from the gel, surface tensions can cause pore collapse and result in materials with poor textural properties. This is particularly the case when water (high surface tension) has to be removed, as it is the case in most sol-gel recipes which are based in hydrolytic conditions.

To tackle these limitations, various strategies are developed by materials chemists. Two of them, in particular, have been leveraged and further developed in the current PhD project. The aerosol-assisted sol-gel and the non-hydrolytic sol-gel will be detailed and their potential to solve the traditional sol-gel challenges explained.

1.5.3 Aerosol-assisted sol-gel

In the so-called “aerosol-assisted sol-gel” process (AASG), the sol-gel chemistry described above is coupled with an aerosol processing. In a typical procedure, a diluted solution of hydrolysed precursors (that is relatively stable in time) is atomized under compressed air in the form of air born droplets. These droplets are processed through a heated zone (tubular furnace or cyclone fed with drying) where they are dried.[161-164] During drying, the solvent first evaporates, triggering both the evaporation induced self-assembly phenomenon (EISA) of the templating agents (if any) and the inorganic polycondensation of the molecular precursors. The dried spherical particles

are recovered and calcined to remove any volatiles or surfactants and obtain the final material. The addition of templating agents in the precursors solution allows controlling the texture of the final material.[156] A schematic representation of the set-up used in the current study is presented in Figure I.7.

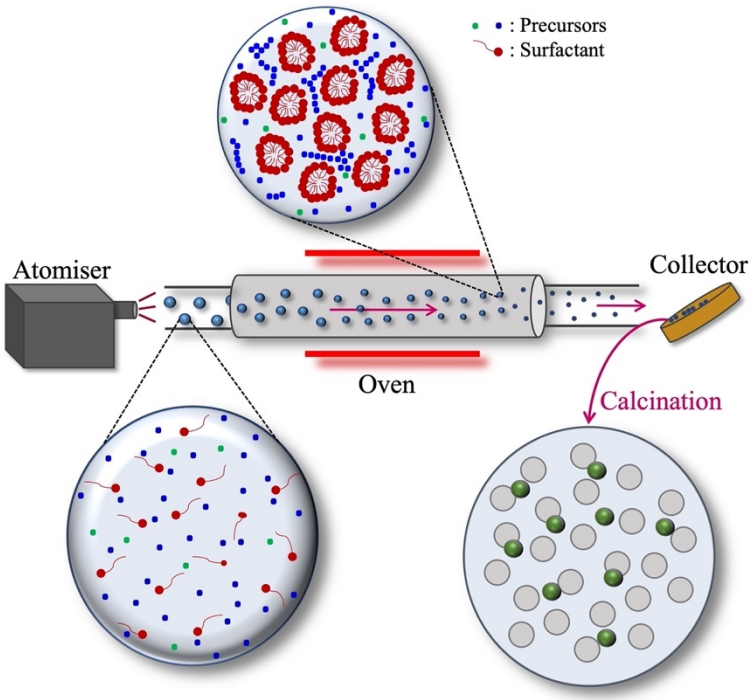

Figure I.7: Schematic view of the aerosol-assisted sol-gel process[156] Each droplet is composed of the similar amount of molecular precursors (blue and green dots) and potentially templating agents (tailed red dots).

This aerosol route was shown to give access to a variety of efficient (mixed) oxide catalysts with a high degree of control on homogeneity and texture.[164-169] The method can also be used to prepare supported metal nanoparticles.[160,163,170-173]

With regard to the limitations mentioned above, the AASG process allows for a high control on homogeneity. Indeed, the rapid formation of the solid particles inside the heated zone force species with different reaction rates to react or be confined in the inorganic matrix. This phenomenon is referred as “kinetic quenching”.[174]

1.5.4 Non-hydrolytic sol-gel

To circumvent the differences in hydrolysis and condensation rates between the precursors, a solution is to operate in non-aqueous environments, where oxo bridges can be formed using oxygen donors other than water.[7,175-184] In such "non-hydrolytic sol-gel" (NHSG) routes, the kinetics of solvolysis-condensation tend to be much slower and to vary only to a limited extent among different precursors. As a result, a so-called “kinetic levelling” is commonly observed, resulting in the formation of mixed oxide materials that exhibit exceptional homogeneity, even oxides with complex formulations[7,176,178] and organo-inorganic hybrids.[182,185] Additionally, by utilizing organic solvents and by avoiding the slightest presence of water, the risk of pore collapse during the drying process is mitigated, due to the low surface tension of these organic solvents. As a result, highly porous materials can be achieved.[7,76,175,177,186-188]

Figure I.8 summarizes the different steps in a non-hydrolytic sol-gel synthesis. Since all steps need to happen in an inert atmosphere in order to avoid water and oxygen, the precursors are dissolved and mixed in a glovebox. After the active sites and support precursors are dissolved and mixed together with an appropriate oxygen donor, in an autoclave, the latter is sealed and put in an oven at a set temperature for a specific duration. During that period, the inorganic polycondensation reactions take place and a gel is formed. The gel is then dried under a Schlenk line (Figure I.8) to remove trapped solvent and polycondensation reactions volatiles. Finally, the dried gel is calcined (here in a tubular furnace) to remove templating agents (if any) and residual volatiles.

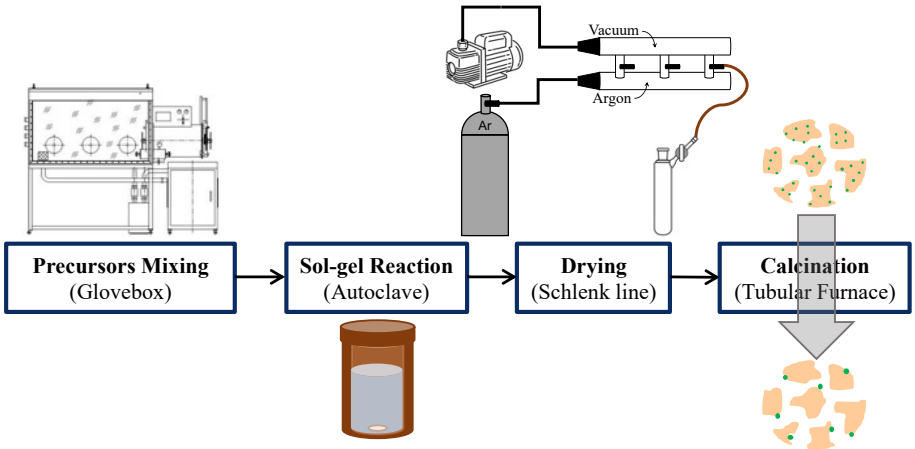

Figure I.8: Non-hydrolytic sol-gel procedure for the synthesis of catalysts.

NHSG routes were reported to lead to various types of metallosilicate catalysts showing high performance in many different fields of applications, including olefin metathesis,[189,190] olefin epoxidation,[159,191] mild oxidation of sulphur compounds,[192] aminolysis,[177] photocatalysed aniline degradation,[193] propane dehydrogenation,[194] glycerol dehydration,[195] titanium oxide coating,[196] etc.

CHAPTER 2: OBJECTIVES AND STRATEGY

2.1 Objectives

As shown in the general introduction, the research on the ethanol-to-butadiene reaction has gained an exponential attention in the last decades due to the increasing interest in bio-based processes, especially those that have the potential to mitigate our dependence towards petrochemical resources. In the mist of this economic and ecological challenge, the race to synthesize more **active bifunctional catalyst** with **tailored properties** in a **facile synthesis** procedure is still ongoing.

More specifically, the targeted material should be **mesoporous** to avoid mass transfer limitations. In terms of active species, it must combine **Lewis** acid sites (**isolated Ta** in the silica matrix) and **redox** sites (well dispersed **metal nanoparticles** of **Ag** or **Cu)**.

As most of synthesis procedures described in the literature rely on long and multi-step processes like impregnation or zeolites synthesis, we aim on developing **easy** and/or **straightforward** protocols to tackle these issues. Ideally, our protocols must provide a **one-step** synthesis of such catalysts with control on **texture** and active sites **speciation** and **dispersion**.

Apart from this general “applied” objective, we aim to leverage the peculiar sol-gel techniques briefly described above to gain new fundamental insights on the working patterns of these bifunctional catalysts. In this perspective, some scientific questions emerge:

(i) How can we control the nature of the two types of active sites through the synthesis process? More specifically, how do we obtain open Lewis sites inside the silica matrix and metal nanoparticles in one material in a one-step synthesis protocol?

(ii) What is the importance of the active sites proximity and dispersion in our bifunctional catalyst for the performance in the ethanol-to-butadiene? How can we mitigate undesired side-products formed by the direct dehydration of ethanol and boost the performance towards our main product of interest?

(iii) Finally, what dictates the deactivation of the catalyst and what solutions can we develop to remedy those mechanisms?

With the answers to these fundamental questions in hands, we aim to propose a unified view on the parameters that govern the catalytic behaviour of these bifunctional catalysts in the ETB reaction, and therefore to provide useful guidelines for future catalyst developments.

2.2 Strategy

Moving forward, **sol-gel** chemistry offers a foundation on which more advanced techniques can be leveraged. Two great examples of the versatility of the sol-gel approach are the **aerosol-assisted sol-gel** (AASG) and the **non-hydrolytic sol-gel** (NHSG). Each method provides unique advantages that will be utilized separately.

Although the AASG is already applied for catalysts active in other bio-based applications,[160,161,163,164,167,170,197] no such technique is currently used to the best of our knowledge for the preparation of catalysts potentially active in the ETB reaction. Here, we will **develop** and **optimize** a synthesis protocol to obtain in **one step** a bifunctional catalyst with properties adapted to the ETB reaction, as depicted in Scheme II.1.

The first chapter will tackle the synthesis of **AASG**-made mesoporous **Ta-Ag** catalysts. A **one-pot** spray-dried Ta-Ag catalyst will be compared with its **impregnated** counterpart, both on commercial silica and AASG-made silica. **Acidity** measurements and advanced **microscopy** and **spectroscopy** techniques will help **understand** the fundamental differences between the two synthesis protocols and highlight the **advantages** of the AASG process. With these understandings in mind, different loadings of Ta and Ag will be synthesized, characterized and tested to **improve** the catalytic performance of our system. After finding the **optimal** formulation, different catalytic **conditions** will be tested to understand catalysts **behaviour** further boost the **selectivity** towards butadiene.

The second chapter will be based on the study of **AASG**-made **Ta-Cu** catalysts. A wide screening of Ta and Cu loadings will be synthesized to study the influence of **proximity**, **dispersion,** and **interactions** between distinct active sites. **Ta insertion** will be further looked into with advanced **mass spectrometry** measurements and **probed-NMR** spectroscopy. These parameters also set alongside catalytic tests in order to maximize butadiene **selectivity**. Finally, we will go more in depth into the different **conditions** in which the catalytic run takes place and study the influence of the different parameters involved to gain more **understanding** on the reaction

mechanism, study the **rate-limiting** step dynamics and in the end, obtain an **optimal catalytic procedure**.

Convinced by the potential of **NHSG**, we already conducted a preliminary study in 2019 on Ag-Ta-SiO_2 catalysts and confirmed their **good performance** in the ETB reaction.[7] On this basis, the preparation method was further investigated in this PhD project, focusing on two strategies, the **ether** route and the **acetamide** elimination route for the synthesis of Ta-Cu-based catalysts. Using a series of characterisation techniques such as X-ray photoelectron spectroscopy, infrared spectroscopy on CO and pyridine-adsorbed samples, electron microscopy, etc will help us the difference in **Ta insertion** and the influence of it on the catalysts **properties** and catalytic **behaviour**. In the second part of this chapter, the loadings of Ta and Cu will be **optimized** to improve the best BD productivity.

The fourth and final chapter will assess the possibility of synthesizing an effective bifunctional **Ta-Cu** catalyst by **combining** both previously studied NHSG synthesis routes, in the hope of combining the benefits in one synthesis protocol. For this, the concept of "**delayed addition**" will be introduced and studied by applying different ratios of both **ether** and **acetamide** elimination route in the synthesis process. The influence of these ratios on the catalysts **performance** will be studied through infrared spectroscopy, X-ray photoelectron spectroscopy and acidity measurements.

It is noted that both synthesis routes (NHSG and AASG) have been investigated in parallel during this PhD thesis, and that the presentation of the results along the document do not represent the chronological order of the investigations. This means that the teachings gained in certain chapters could not necessarily be leveraged in the experiments described in other chapters.

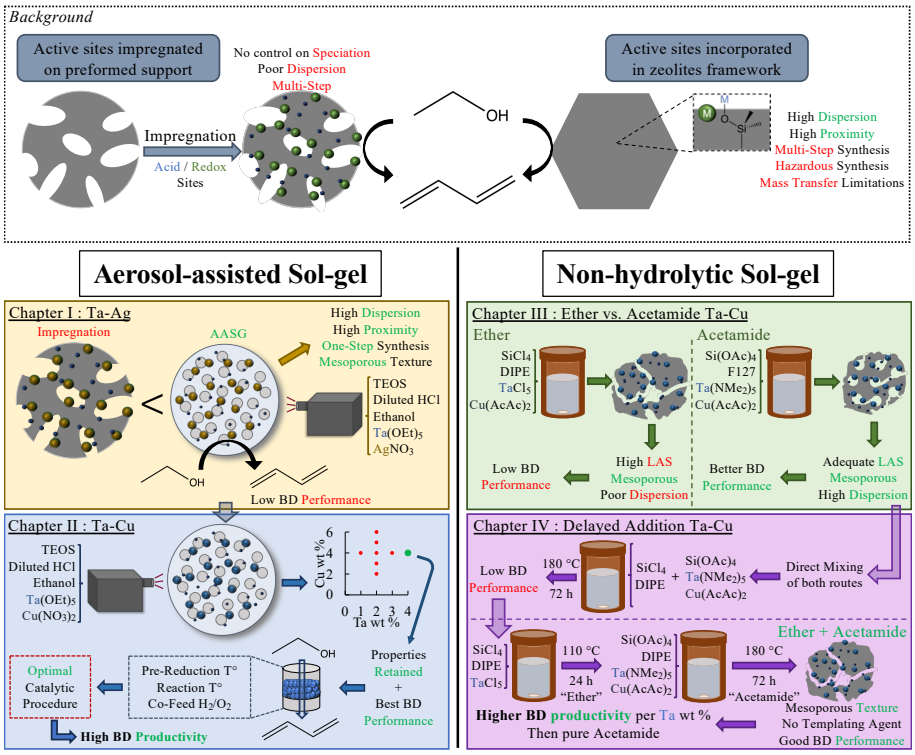

Scheme II.1: Global strategy of the thesis.

CHAPTER 3: EXPERIMENTAL

3.1 General synthesis protocols

3.1.1 Materials

Commercially available chemicals:

- Tetraethylorthosilicate >97.0 % (TCI Chemicals)
- HNO_3 65 % (Merck)
- HCl 37 % (Merck)
- Pluronic F127 (Sigma-Aldrich). In NHSG, Pluronic F127 was dried under vacuum (< 10^{-6} mbar) at 100 °C overnight and stored in a glovebox.
- Ethanol absolute (VWR, > 99.8 %)
- Pentane (ROTH, >99 %)
- Tantalum(V) ethoxide (ABCR 99.99 %)
- Silver nitrate (VWR, 99.9 %)
- Copper(II) nitrate hemi(pentahydrate) (Alfa Aesar, 98 %)
- Silicon tetrachloride (Acros Organics, 99.8 %),
- Copper(II) acetylacetonate (TCI, 97 %),
- Diisopropylether (Sigma, 99 %)
- Pyridine (Sigma, anhydrous, 99.8 %)

Silicon tetraacetate and pentakis(dimethylamido)tantalum(V) were prepared according to literature[198-200]

3.1.2 Dry impregnation

The appropriate amount of tantalum ethoxide was weighted inside a glove box and stored in a sealed vial before being taken out of the glovebox. Silver nitrate was weighted and both precursors were mixed in a volume of ethanol absolute in the sealed vial corresponding to the total pore volume determined by N_2-physisorption of the catalyst to impregnate (commercial silica or spray-dried silica). The mixture was then added to the catalyst, stirred until a thick paste was obtained. The paste was put to rest for 2 h at room temperature and dried overnight at 100 °C. The powder was then calcined at 500 °C (flowing dry air, 5 °C min^{-1}, 5 h). This sample is denoted 1Ag5Ta/SiO_2 where the dash bar "/" indicates that the active components have been incorporated by impregnation. The same protocol was applied on a commercial silica support (Silicon dioxide nanopowder, 10-20 nm particle size (BET), 99.5%, Aldrich), to prepare a reference catalyst denoted

"1Ag5Ta/SiO_2-A". Another sample was prepared by impregnating silver nitrate on the 5Ta-SiO_2 catalyst prepared by AASG (sample denoted 1Ag/5Ta-SiO_2).

3.1.3 AASG

Precursors solution A is prepared by mixing 6 g of tetraethylorthosilicate (TCI Chemicals, > 97.0 %) with 12 g of aqueous acid 0.01 M (diluted HNO_3 in the case of an Ag-containing catalyst precursor, diluted HCl otherwise) to hydrolyse the silicon precursor overnight. Solution B is prepared by mixing (overnight) 1.94 g of Pluronic F127, 22.5 g of ethanol absolute and 4 g of distilled water. Both solutions are then put together and the desired amount of metals precursors (tantalum(V) ethoxide diluted in pure ethanol, silver nitrate and/or copper(II) nitrate hemi(pentahydrate), depending on the targeted formulation) are added to the mixture and left to stir for 30 minutes before the spray-drying process. This precursor solution is atomized with a Six-jet atomizer 9306 from TSI using a compressed air flow of 30 psi, and dried by passing through a tubular furnace set at 450 °C (residence time around 1 second).[201] The resulting powder is recovered on 0.45 µm nitrocellulose filters (Sartorius) and calcined at 500 °C (flowing dry air, 5 °C min^{-1} and a 5 h dwell). This calcination temperature was selected following a short survey of the effect of calcination temperatures between 500 and 750 °C on the catalytic performance (Appendix, Section 9.1).

Ag-Ta-based catalysts are denoted "*x*Ag*y*Ta-SiO_2", where *x* is the nominal Ag loading (wt %), *y* is the nominal Ta loading (wt %), and the dash "-" indicates that both active elements have been incorporated directly in one-step (as opposed to reference samples prepared by impregnation, see below). "*y*Ta-SiO_2" catalysts are prepared according to the same one-step aerosol protocol but omitting the addition of Ag. A pristine mesoporous silica was also prepared according to the same protocol, but omitting the addition of both Ta and Ag (simply denoted "SiO_2").

Cu-Ta-based catalysts are denoted "*x*Cu*y*Ta-SiO_2", where *x* is the nominal Cu loading (wt %), *y* is the nominal Ta loading (wt %), and the dash "-" indicates that both active elements have been incorporated directly in one-step. Table III.1 describes exact precursors and solvent masses used in the spray-drying process.

Table III.1: Solvents and precursors masses (g) for the spray-dried catalysts (the same table expressed in moles is available in Appendix, Table IX.2).

Catalyst	TEOS	HCl 0.01M	F127	EtOH[a]	Distilled H_2O	$Ta(OEt)_5$	$AgNO_3$	$Cu(NO_3)_2 \cdot 2.5H_2O$
1Ag1Ta-SiO_2	6.04	10.01	1.94	22.61	4.05	0.0390	0.0288	-
2Ag1Ta-SiO_2	5.99	10.04	1.94	22.55	4.00	0.0393	0.0570	-
5Ag1Ta-SiO_2	6.01	10.04	1.95	22.50	4.09	0.0392	0.145	-
1Ag2Ta-SiO_2	6.05	10.00	1.94	22.51	4.10	0.0801	0.0282	-
2Ag2Ta-SiO_2	6.00	10.03	1.93	22.60	4.02	0.0803	0.0556	-
5Ag2Ta-SiO_2	6.00	10.00	1.94	22.57	4.03	0.0829	0.144	-
2Cu2Ta-SiO_2	6.01	10.02	1.93	22.51	4.10	0.0810	-	0.131
3Cu2Ta-SiO_2	6.01	10.34	1.94	22.53	4.00	0.0806	-	0.197
4Cu2Ta-SiO_2	6.00	10.06	1.95	22.56	4.01	0.0810	-	0.267
5Cu2Ta-SiO_2	6.00	10.02	1.95	22.90	4.00	0.0800	-	0.333
6Cu2Ta-SiO_2	6.00	10.02	1.94	22.44	4.06	0.0800	-	0.407
4Cu1Ta-SiO_2	6.01	10.07	1.97	22.49	4.01	0.0410	-	0.264
4Cu3Ta-SiO_2	6.01	10.04	1.95	22.56	4.01	0.125	-	0.265
4Cu4Ta-SiO_2	6.01	10.01	1.93	22.50	4.02	0.166	-	0.266

[a]Ethanol absolute

3.1.4 NHSG

NHSG processes were performed under Ar atmosphere or high vacuum by using a Schlenk line and a dry box with H_2O and O_2 levels below 1 ppm. CH_2Cl_2 (Carl Roth, ≥ 99.8 %) was dried with P_4O_{10}. All solvents were distilled and stored in a glovebox under molecular sieves.

- Catalysts synthesis through the ether route

Xerogel synthesis through the ether route (Scheme III.1, left). For the synthesis of Cu-Ta-SiO_2, silicon tetrachloride and diisopropylether were loaded in a 100 cm^3 Teflon autoclave with 25 cm^3 of dichloromethane. In separate vials, tantalum(V) pentachloride and copper acetylacetonate were each dissolved in 10cm^3 of dichloromethane before being transferred to the Teflon autoclave while stirring. The autoclave was sealed and kept in an oven at 110 °C for 72 hrs for the gelation. Afterwards, the autoclave was cooled down and put back into the glovebox, opened and the gel was transferred into a Schlenk flask. The gel was dried under vacuum (< 10^{-6} mbar) at 60 °C overnight to remove solvent and volatile condensation products. Finally, the resulting powder was calcined at 500 °C (flowing dry air, 5 °C min^{-1}, 5 h). Samples are denoted Et-XTaYCu where “Et” refers to the ether route, “X” is the nominal Ta wt.%, and “Y” is the nominal Cu wt.% in the metallosilicate. Table III.2 describes exact precursors masses used in the synthesis protocol.

Table III.2: Precursors masses (g) for ether-based catalysts. Solvent is CH_2Cl_2 and 45 mL were used in total (the same table expressed in moles is available in Appendix, Table IX.3).

Catalyst	$SiCl_4$	DIPE	$TaCl_5$	$Cu(AcAc)_2$
Et-2Ta2Cu	4.600	5.527	0.0651	0.137

- Catalysts synthesis through the acetamide elimination route

Xerogel synthesis through the acetamide elimination route (Scheme III.1, right). For the synthesis of Cu-Ta-SiO_2, silicon tetraacetate and Pluronic F127 were loaded in a 100 cm^3 Teflon autoclave in a glovebox and dissolved in 40 cm^3 of dichloromethane. In a separate vial, pentakis(dimethylamido)tantalum(V) was dissolved in 5 cm^3 dichloromethane. This solution was then added to the solution of $Si(OAc)_4$ and Pluronic F127 while stirring and copper acetylacetonate was finally added. The autoclave was sealed and kept in an oven at 180 °C for 72 hrs for the gelation. Afterwards, the autoclave was cooled down and put back into the glovebox, opened and the gel was transferred into a Schlenk flask. The gel was dried under vacuum (< 10^{-6} mbar) at 60 °C overnight to remove solvent and volatile condensation products (dimethylacetamide and acetic acid anhydride). Finally, the resulting powder was calcined at 500 °C (flowing dry air, 5 °C min^{-1}, 5 h). Samples are denoted Ac-XTaYCu where “Ac” refers to the acetamide elimination route, “X” is the nominal Ta wt.%, and “Y” is the nominal Cu wt.% in the metallosilicate. Table III.3 describes exact precursors masses used in the synthesis protocol.

Table III.3: Precursors masses (g) for acetamide-based catalysts. Solvent is CH_2Cl_2 and 45 mL were used in total per synthesis (the same table expressed in moles is available in Appendix, Table IX.4).

Catalyst	$Si(OAc)_4$	F127	$Ta(NMe_2)_5$	$Cu(AcAc)_2$
Ac-2Ta2Cu	7.099	3.630	0.0730	0.136
Ac-2Ta3Cu	7.106	3.639	0.0745	0.207
Ac-2Ta4Cu	7.101	3.638	0.0744	0.280
Ac-2Ta5Cu	7.102	3.632	0.0745	0.355
Ac-1Ta4Cu	7.093	3.631	0.0370	0.277
Ac-3Ta4Cu	7.095	3.641	0.111	0.279
Ac-4Ta4Cu	7.094	3.634	0.150	0.280

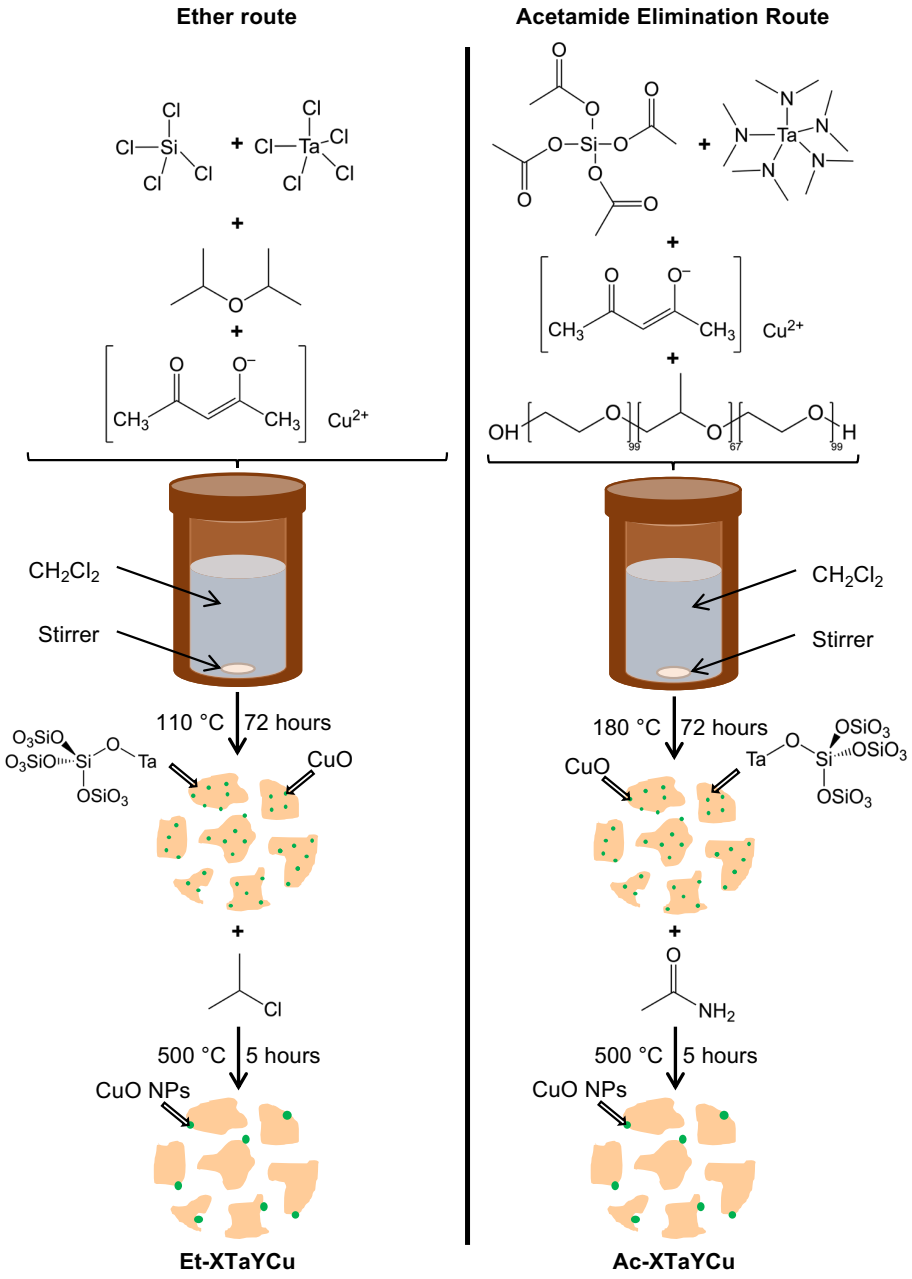

Scheme III.1: Synthesis protocol and chemical reactions involved in the ether route and the acetamide elimination route.[126]

- Catalysts synthesis through the one-pot mixing of ether and acetamide routes

For the xerogel synthesis via a combination of ether route and acetamide elimination route (for a justification of this strategy, see Section 7.3.1), the protocol consisted of mixing in one-step all precursors. First, $SiCl_4$ and silicon tetraacetate ($Si(OAc)_4$) were dissolved in 45 mL of CH_2Cl_2 and added to a Teflon autoclave. Diisopropylether (DIPE), pentakis(dimethylamido)tantalum(V) ($Ta(NMe_2)_5$) and copper acetylacetonate ($Cu(AcAc)_2$) were then added sequentially in the autoclave. The autoclave was sealed in a metal casing and left at 145 °C for 4 days. Afterwards, the autoclave was cooled down and put back into the glovebox, opened and the gel was transferred into a Schlenk flask. The gel was dried under vacuum (< 10^{-6} mbar) at 60 °C overnight to remove solvent and volatile condensation products. Finally, the resulting powder was calcined at 500 °C (flowing dry air, 5 °C min^{-1}, 5 h). Considering a basis of 64 Si atoms, we express separately in the sample name the number of Si atoms coming from the ether route and the amount of Si atoms coming from the acetamide elimination route. Thus, samples are denoted *A*Et*B*Ac-*X*Ta*Y*Cu where "Et" refers to the ether route, "Ac" refers to the acetamide elimination route, "*A*" refers to the molar amount of Si coming from $SiCl_4$ added in the synthesis protocol based on 64 Si atoms in total, "*B*" refers to the atomic amount of Si coming from $Si(OAc)_4$ added in the synthesis protocol based on 64 Si atoms in total, "X" is the nominal Ta wt.%, and "Y" is the nominal Cu wt.% in the catalyst. Table III.4 describes exact precursors masses used in the direct mixing protocol.

- Catalysts synthesis through the "delayed addition"

For the xerogel delayed synthesis, the protocol was divided into 2 steps: first, the addition and partial polycondensation of the ether route precursors and second, the addition of the acetamide elimination route precursors (for a justification of this strategy, see Section 7.3.2). Both steps were carried out in a glovebox and Teflon autoclaves were only transferred in the oven when fully sealed.

In the first step, $SiCl_4$, diisopropylether (DIPE) and a catalytic amount of $TaCl_5$ were added to a Teflon autoclave with CH_2Cl_2 as solvent, sealed in a metal casing and left at 110 °C for 24 h. Whatever the ether/acetamide ratios, the $SiCl_4/CH_2Cl_2$ ratio was kept constant to keep the polycondensation rate constant during the first 24 h. $TaCl_5$ served here as the catalyst for the start of the polycondensation.

After 24 h, the autoclaves were taken back into the glovebox to add the rest of the precursors. Silicon tetraacetate ($Si(OAc)_4$), tantalum dimethylamide ($Ta(NMe_2)_5$), copper acetylacetonate ($Cu(AcAc)_2$) and remaining DIPE (for the fraction of $SiCl_4$ that has not reacted during the first polycondensation) were dissolved in CH_2Cl_2 separately and transferred in the autoclave. In total, 45 mL of CH_2Cl_2 are used. The autoclave was sealed back in the metal casing and left at 180 °C for 72 h. Afterwards, the autoclave was cooled down and put back into the glovebox, opened and the gel was transferred into a Schlenk flask. The gel was dried under vacuum (< 10^{-6} mbar) at 60 °C overnight to remove solvent and volatile condensation products. Finally, the resulting powder was calcined at 500 °C (flowing dry air, 5 °C min^{-1}, 5 h). Samples are denoted *A*Et*B*Ac-*X*Ta*Y*Cu-D*Z*h where "Et" refers to the ether route, "Ac" refers to the acetamide elimination route, "*A*" refers to the molar amount of $SiCl_4$ added in the synthesis protocol based on 64 Si atoms in total, "*B*" refers to the molar amount of $Si(OAc)_4$ added in the synthesis protocol based on 64 Si atoms in total, "X" is the nominal Ta wt.%, and "Y" is the nominal Cu wt.% in the metallosilicate. "*Z*" represents the h between the first polycondensation and the addition of the rest of the precursors.

Table III.4 describes exact masses added to the autoclaves for the different catalysts. In the study, we systematically vary the ether/acetamide ratios: considering a basis of 64 Si atoms, we express separately in the sample name the number of Si atoms coming from the ether route and the amount of Si atoms coming from the acetamide elimination route. For example, for the samples denoted "56Et8Ac", 56 out of 64 Si atoms come from $SiCl_4$ (ether route) and 8 out of 64 Si atoms come from $Si(OAc)_4$ (acetamide elimination route).

In addition to the study of ether/acetamide ratios, different Ta loadings have been synthesized. Cu loading remained unchanged as previous studies have already proven the 4 wt.% to be the most selective towards butadiene. "DIPE" (2) refers to the potential DIPE needed in the second step to provide additional oxygen atoms, if needed, to keep the molar ratio $SiCl_4$/DIPE=2.

Table III.4: Precursors masses (g) for catalysts synthesized via the direct mixing and delayed protocol (the same table expressed in moles is available in Appendix, Table IX.5).

Catalyst	$SiCl_4$	DIPE (1)	$TaCl_5$	$Si(OAc)_4$	$Ta(NMe_2)_5$	$Cu(AcAc)_2$	DIPE (2)
4Ac60Et-4Ta4Cu	5.090	5.960	-	0.534	0.186	0.341	-
6Ac58Et-4Ta4Cu	4.930	5.440	-	0.797	0.191	0.340	-
8Ac56Et-4Ta4Cu	4.770	5.02	-	1.062	0.187	0.345	-
56Et8Ac-4Ta4Cu-D8h	4.760	5.030	0.020	1.071	0.164	0.339	-
56Et8Ac-1Ta4Cu-D24h	5.984	3.621	0.007	1.33	0.049	0.374	2.427
56Et8Ac-2Ta4Cu-D24h	5.981	3.617	0.007	1.329	0.103	0.373	2.421
56Et8Ac-4*Ta4Cu-D24h	5.981	3.603	0.004	1.328	0.026	0.373	2.429
48Et16Ac-1Ta4Cu-D24h	5.135	3.084	0.003	2.659	0.052	0.372	0.881
48Et16Ac-2Ta4Cu-D24h	5.131	3.088	0.006	2.663	0.099	0.374	0.885
48Et16Ac-4*Ta4Cu-D24h	5.13	3.091	0.005	2.667	0.05	0.377	0.884
40Et24Ac-1Ta4Cu-D24h	4.276	2.58	0.005	3.995	0.049	0.376	/
40Et24Ac-2Ta4Cu-D24h	4.277	2.574	0.007	4	0.1	0.374	/
40Et24Ac-4*Ta4Cu-D24h	4.278	2.578	0.01	4.01	0.077	0.375	/
32Et32Ac-1Ta4Cu-D24h	3.427	2.057	0.005	5.324	0.049	0.375	/
32Et32Ac-2Ta4Cu-D24h	3.426	2.059	0.008	5.319	0.099	0.376	/
32Et32Ac-4*Ta4Cu-D24h	3.432	2.054	0.013	5.318	0.103	0.377	/

3.2 Characterisation techniques

Textural properties (surface area, pore volume, pore size) were determined by nitrogen physisorption at 77.4 K on a Tristar 3000 instrument from Micromeritics, USA. Prior to measurement, samples were degassed at 150 °C for 8 hrs minimum. The specific surface area was determined by the BET method with at least five data points with relative pressure between 0.05 and 0.30.

X-ray photoelectron spectroscopy measurements were carried out on a SSI X probe spectrometer (model SSI 100, Surface Science Laboratories, Mountain View, CA) equipped with a monochromatized Al-Kα radiation (1486 eV). The catalyst powders previously pressed in small stainless troughs of 4 mm diameter, were placed on an insulating home-made ceramic carousel.

The pressure in the analysis chamber was set at around 10^{-8} Pa. The analysed area was approximately 1.4 mm^2 and the pass energy was set at 150 eV. The Si2p peak of silicon has been fixed to 103.5 eV to set the binding energy scale.[202] Data treatment was performed with the CasaXPS program (Casa Software Ltd, UK) and spectra were decomposed with the least squares fitting routine provided by the software with a Gaussian/Lorentzian (85/15) product function and after baseline subtraction.

Temperature programmed desorption of ammonia (NH_3-TPD) was performed on a Hiden CATLAB-PCS microreactor connected to a mass spectrometer equipped with a quadrupole separator. Samples (400–800 µm particle size) were first dehydrated at 300 °C (10 °C min^{-1}) for 1 hr under Ar (40 cm^3 min^{-1}). Ammonia adsorption took place at 150 °C for 40 minutes (20 cm^3 min^{-1} of Ar, 5 %vol NH_3) before an 80 minutes purge under Ar (40 cm^3 min^{-1}). The temperature was then increased to 500 °C (5 °C min^{-1}, except in Chapter 4 where a ramp of 10 °C min^{-1} was applied) to desorb ammonia. The experimental error on the number of acid sites is estimated at 5 %.

Solid-state ^{31}P and ^{29}Si magic angle spinning (MAS) nuclear magnetic resonance NMR spectra were acquired on Bruker AvanceIIIHD-700 NMR spectrometer with a 4 mm CP-MAS Bruker probe at frequencies 139.2 MHz for ^{29}Si and 283.7 MHz for ^{31}P. MAS rates were 5 kHz for ^{29}Si CPMAS and 10 and 12 kHz for ^{31}P MAS spectra. Chemical shifts were referenced externally to ^{29}Si δ[3-(trimethylsilyl)-1-propanesulfonic acid sodium salt (DSS)]: 1.53 ppm; ^{31}P δ [H_3PO_4] (85 %)]: 0.0 ppm.

Time-of-flight secondary ion mass spectrometry (ToF–SIMS) analyses were conducted with a TOF.SIMS5 instrument (IONTOF GmbH, Münster, Germany). Sample powders were pressed onto the adhesive part of Post-it papers. A pulsed Bi^{5+} metal ion source was used to produce a primary beam using an acceleration voltage of 30 kV. An AC target current of 0.07 pA with a bunched pulse width lower than 1 ns was used. Both positive and negative secondary ion species were analysed. Mass spectra were obtained by scanning the primary ion beam over a 250x250 $µm^2$ area. The total primary ion beam dose for each analysed area was always kept below 5.10^{10} ions per cm^2, ensuring static conditions. Lateral resolution of ~3 µm and mass resolution $m/\Delta m$ > 4000 at 29 *m/z* were maintained for positive and negative mass spectra acquisition. Charge compensation was conducted using an interlaced electron flood gun (kinetic energy = 20 eV). Data analyses were carried out with SurfaceLab (version 6.5).

FTIR spectra (4000–400 cm^{-1}) were recorded on a Bruker Equinox 55 spectrometer (transmission mode, through KBr pellets).

FTIR spectra after pyridine adsorption were similarly recorded. Catalysts were pelletized and degassed overnight at 350 °C. Pyridine adsorption was carried out at room temperature. FTIR spectra were taken at room temperature and after 2h degassing under vacuum at 150 °C.

DRUV spectra (150–500 nm) were recorded on a Shimadzu UV-3600Plus.

For carbon monoxide adsorption followed by FTIR analysis, about 20 mg of the sample was pressed to yield a self-supported wafer. The sample was then introduced into a glass cell specially designed for in situ FTIR spectroscopy and enabling preliminary thermal treatments. The activation procedure always started with a heating step (5 K min^{-1}) under vacuum from room temperature to 628 K with a 3 h plateau at 628 K. When the activation procedure was finished, the sample was cooled to 100 K and a reference spectrum was recorded (128 scans at a 4 cm^{-1} resolution). Carbon monoxide (99.99997% Air Liquide) calibrated aliquots were then gradually introduced into the cell, and IR spectra were subsequently recorded. The procedure was repeated until the evolution of adsorbed species indicated that CO saturation of the surface was reached.

A transmission electron microscope FEI Tecnai F20 (FEI, Eindhoven, The Netherlands) equipped with a field emission gun source, a 4k CCD camera (FEI Eagle) and operated at 200 kV was used for sample visualization. STEM-EDS measurements were performed on a FEI Titan Themis instrument with a combination of a spherical aberration image (Cs) corrector, a monochromator system, sensitive ChemiSTEM technology, and a high-end GATAN GIF Quantum energy filter for EELS and EFTEM with a new enhanced piezo stage, FEI and GATAN software, and a FEI Ceta 16-megapixel CMOS camera.

3.3 Catalytic testing

Calcined catalysts (pressed and sieved in the 0.20–0.40 mm particle size range) were added to a tubular reactor (stainless steel, 0.6 cm internal diameter). The latter was then filled to the top with silica beads. Before reaction, the catalyst was pre-treated *in situ* by feeding hydrogen (30 vol.% H_2 in N_2) for 1 hr at 350 °C (for silver or copper reduction). Catalytic testing was carried out by feeding a mixture of ethanol absolute and pentane as internal standard (95-5 molar percent) (fed with a NE-300 syringe pump) diluted in nitrogen (5 mol% of ethanol in N_2). If not stated otherwise, 96 mg of sieved catalyst was introduced in the reactor, 0.14 mL/hr of a liquid ethanol-pentane mixture was diluted in 18 mL/min of N_2 and fed in the reactor. If not stated otherwise, the tests were carried out at atmospheric pressure and at 325 °C

for 4 h. The gas effluent was analysed on a VARIAN 3800 Gas Chromatograph (1 injection per 15 minutes, 16 injections in total) equipped with a flame ionization detector (FID) and a Restek Rt-U-Bond column (30 m long, internal diameter of 0.32 mm, film thickness of 10 µm). In other words, the catalytic data (conversion and selectivity) are averaged on the overall time-on-stream for each give temperature. After having run 5 identical catalytic tests with the same catalyst, it was concluded that the error on these measurements is estimated at 5 %.

Conversion (X), selectivity (S), yield (Y) and carbon balance (CB) were calculated as follows:

$$X_{EtOH}(\%) = \frac{MF_{EtOH_i} - MF_{EtOH_f}}{MF_{EtOH_i}}$$

$$S_{Product}(\%) = N * \frac{MF_{Product}}{MF_{EtOH_i} - MF_{EtOH_f}}$$

$$Y_{Product}(\%) = X_{EtOH} * S_{Product}$$

$$CB\ (\%) = \frac{\sum \frac{n_{N_2}}{MF_{N_2}} * MF_{EtOH/Product}}{MF_{EtOH_i}}$$

Where, MF_{EtOH_i} is the molar fraction of ethanol fed in the reactor, MF_{EtOH_f} is the molar fraction of ethanol after the reactor, *N* is the stoichiometric ratio between the considered product and ethanol, n_{N_2} is the molar input of nitrogen in the reactor and MF_{N_2} is the molar fraction of nitrogen after the reactor. Products considered in the carbon balance were ethanol, acetaldehyde, ethylene, diethylether, 1-butene, 2-butene and butadiene.

Throughout the manuscript, the CB was always between 90 and 110 %, unless stated otherwise.

CHAPTER 4: Aerosol-assisted sol-gel synthesis of mesoporous Ag–Ta catalysts for the direct upgrading of ethanol to butadiene

The results presented in this Chapter are published in:

Aerosol-assisted sol-gel synthesis of mesoporous Ag-Ta-SiO_2 catalysts for the direct upgrading of ethanol to butadiene, Denis D. Dochain, Antoine Van Den Daelen, Ales Styskalik, Vit Vykoukal, Damien P. Debecker, **RSC Sustainability**, 1 (2023) 599-608.

Aerosol-assisted sol-gel synthesis of mesoporous Ag–Ta catalysts for the direct upgrading of ethanol to butadiene

4.1 Abstract

In this first chapter, we disclose a straightforward, one-step, and continuous preparation of Ta-doped SiO_2 loaded with Ag nanoparticles by coupling sol-gel chemistry with aerosol processing. Combining tantalum ethoxide, silver nitrate, hydrolysed tetraethyl orthosilicate and Pluronic F127 (as a templating agent) in the aerosol process leads to mesoporous bifunctional catalysts featuring a specific surface area between 310–370 $m^2\ g^{-1}$, a pore volume of ca. 0.5 $cm^3\ g^{-1}$ and an average pore diameter of 5 nm. As attested by a variety of characterization techniques, the method leads to the homogeneous incorporation of highly dispersed tantalum species in the silica matrix, thereby creating the required acidic sites. These new catalysts have higher dehydration activity, as compared to the corresponding reference catalysts prepared by classical impregnation of Ta on preformed silica. Concomitantly, relatively small silver nanoparticles are stabilized (~15 nm). The relative Ta and Ag loading can be tuned easily. In the ethanol to butadiene reaction, these aerosol-made catalysts achieve a butadiene yield of ca. 25 % by optimizing the relative loadings of Ta and Ag, outcompeting the corresponding formulations prepared by impregnation.

4.2 Introduction

As explained thoroughly in Chapter 1, a challenge in the preparation of ETB catalysts is the synthesis of bifunctional catalysts in an easy and straightforward protocol that can yield materials with desirable properties such as mesoporosity and high active sites dispersion. This prompted us to explore the potential of AASG to obtain mesoporous Ta-SiO_2 catalysts promoted with Ag nanoparticles and to assess their performance in the ETB reaction. The catalysts are compared to similar formulations obtained from commercial supports or aerosol-made silica, and via classical impregnation. We rationalize the catalytic performance by characterizing the texture, acidity, and active species dispersion.

4.3 Results

4.3.1 Comparing impregnation with one-pot aerosol

Here we compare on the one side a catalyst prepared in one-pot using the AASG process (1Ag5Ta-SiO_2) and on the other side two reference catalysts prepared by impregnation (either on a commercial silica support (SiO_2-A) or on an aerosol-made silica support (SiO_2)). We first targeted formulations with 5 wt. % Ta and 1 wt. % Ag.

ICP results in Table IV.1 are close to the nominal values aimed for Ta (65-76 for bulk Ta obtained vs. 75 aimed, corresponding to 5 wt. %). For Ag, we aimed at a Si/Ag ratio of 179 (corresponding to 1 wt.%) and we generally obtained high values, indicating a lower amount of Ag. XPS results confirms that the impregnation process brings majority of active sites to the surface of the catalysts, as shown by lower Si/Ta and Si/Ag surface ratios relative to bulk ratios (Table IV.1).

The commercial silica support (SiO_2-A) and 1Ag5Ta/SiO_2-A, textural properties are mainly macroporous, as shown by a type III isotherm in Figure IV.2. The pristine AASG-made silica is predominantly mesoporous (Figure IV.1) with type IV isotherms presenting a well-defined hysteresis loop, specific surface area reaching 360 $m^2\ g^{-1}$, large pore volume (0.61 $cm^3\ g^{-1}$) and a narrow mesopore size distribution, centred at 9 nm (Figure IV.1). When incorporating Ta directly in the AASG process, the texture was not significantly affected. In the same way, the bifunctional catalyst prepared in one-pot through AASG (1Ag5Ta-SiO_2) exhibited very similar isotherms and textural parameters.

The impregnation of Ag on the AASG-made 5Ta-SiO_2 (1Ag/5Ta-SiO_2) or the simultaneous impregnation of Ta and Ag on the AASG-made silica (1Ag5Ta/SiO_2) only altered the textural properties of the catalysts in a minor way; while the SSA and pore volume tended to decrease marginally, the mesoporous structure of the material was maintained (Figure IV.1, Table IV.1). Similarly, the texture of the catalyst prepared by impregnation on the commercial silica support (1Ag5Ta/SiO_2-A), was not strongly affected as compared to the support (slight decrease in specific surface area and pore volume, and minor increase in the average pore diameter (Figure IV.2 and Table IV.1).

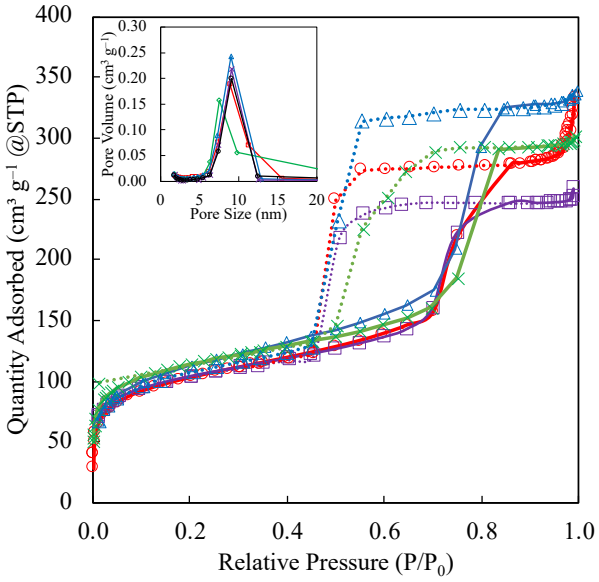

Figure IV.1: N_2-physisorption isotherms of SiO_2 (blue Δ), 5Ta-SiO_2 (purple ■), 1Ag5Ta/SiO_2 (red ○), 1Ag5Ta-SiO_2 (green ×). Adsorption isotherms are plotted as solid lines, desorption isotherms are plotted as dotted lines.

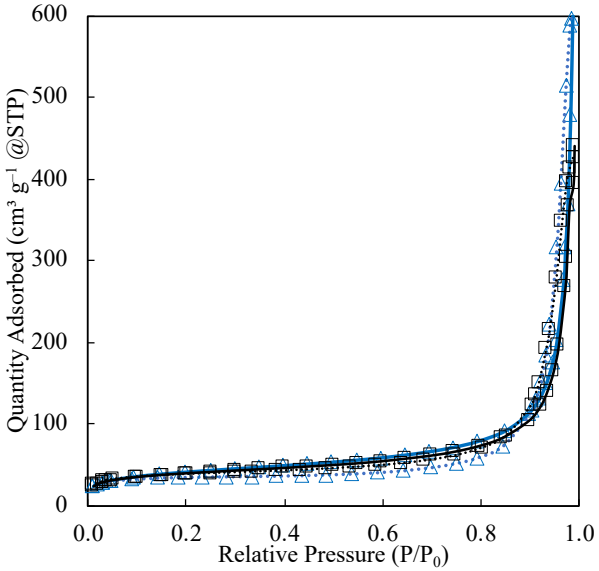

Figure IV.2: N_2-physisorption isotherms of SiO2-A (black), 1Ag5Ta/SiO2-A (blue). Adsorption isotherms are plotted as solid lines, desorption isotherms are plotted as dotted lines.

Table IV.1: Textural properties (N_2-physisorption), bulk composition (ICP), surface composition analysis (XPS), surface acidity (NH_3-TPD).

Sample	S_{BET} (m^2 g^{-1})	V_p (cm3 g^{-1})[a]	D_p (nm)[b]	Bulk Si/Ta[c]	Bulk Si/Ag[c]	Surface Si/Ta[d]	Surface Si/Ag[d]	Acid sites (mmol g^{-1})[e]
SiO_2-A	190	0.61	14.3	-	-	-	-	-
1Ag5Ta/ SiO_2-A	140	0.57	16.2	77	214	n.m.	n.m.	n.m.
SiO_2	370	0.50	5.4	-	-	-	-	-
5Ta-SiO_2	380	0.40	4.1	n.m.	-	n.m.	-	-
1Ag5Ta/SiO_2	340	0.51	6.0	65	215	8.7	14.2	2.4 10^{-2}
1Ag/5Ta-SiO_2	310	0.35	4.5	76	192	72.5	34.2	6.1 10^{-2}
1Ag5Ta-SiO_2	370	0.47	5.0	71	222	62.5	57.0	4.1 10^{-2}

[a] Pore volume at P/P_0=0.98; [b] Calculated as $4V_p/S_{BET}$; [c] Determined by ICP; [d] Determined by XPS; [e] Determined by NH_3-TPD

In the ethanol-to-butadiene reaction, the bifunctional catalyst prepared by impregnation of Ta and Ag on the commercial silica (1Ag5Ta/SiO_2-A) reaches ca. 45 % of ethanol conversion with 16 % in butadiene selectivity and 24 % in dehydration by-products (ethylene + diethylether) and 42 % of dehydrogenation product (acetaldehyde) (Table IV.2). The catalyst prepared by impregnation of Ta and Ag on AASG silica (1Ag5Ta/SiO_2) is less active (23 % conversion), also showing a high selectivity for acetaldehyde, together with a high selectivity for ethylene. The catalyst prepared by direct AASG process (1Ag5Ta-SiO_2), reaches 80 % ethanol conversion but with a low acetaldehyde selectivity and a very low BD selectivity (2 %). This goes hand in hand with a high selectivity towards ethylene, as a result of the direct dehydration of ethanol, typically catalysed by acid sites.[203-205] Characterisation of such acid sites is thus required to better understand the catalytic behaviour and optimize the AASG catalysts.

Table IV.2: Catalytic conversion of ethanol, yield and selectivity of butadiene and by-products; Reaction conditions T=355 °C, WHSV=1.10 h^{-1}.

Catalyst	Ethanol conversion (%)	Butadiene (%)		Acetaldehyde (%)		Ethylene (%)		Diethylether (%)		Others (%)	
		Yield	Sel	Yield	Sel	Yield	Sel	Yield	Sel	Yield	Sel
1Ag5Ta/SiO_2-A	43.5	6.9	15.9	20.1	46.2	3.6	8.4	7.0	16.0	5.9	13.6
1Ag5Ta/SiO_2	22.6	2.3	10.3	9.4	41.7	9.5	42.2	0.01	3.1	0.01	2.7
1Ag5Ta-SiO_2	80.6	1.8	2.2	13.9	17.2	46.3	57.4	3.3	4.1	15.3	19.0

4.3.2 Characterizing the peculiarities of aerosol made AgTa-SiO_2 catalysts

With the intent to understand the catalytic behaviour of the new formulations prepared by aerosol, we here undertake a thorough characterization of the acidic and redox properties of the catalyst (and compare them to impregnated catalysts). We extend our investigations to

various formulations containing 1, 2, 5, or 10 wt. % of Ta and 1, 2, or 5 wt. % of Ag.

TEM analyses reveal the morphology of the silica-based microspheres formed through the aerosol process (Figure IV.4). Spherical particles with a diameter ranging from 50 to 500 nm can be seen as well as the porosity created by the templating agent (~5 nm), compared to the more chaotic structure observed for the commercial silica (Figure IV.3a). As expected, the elemental mapping presented in Figure IV.4a confirms that the impregnation method concentrates Ta and Ag species on the surface of the microspheres. In the AASG-made catalysts, STEM-EDS analysis shows well dispersed Ta throughout the silica spheres (Figure IV.4b) as well as Ag nanoparticles of around 10-20 nm (Figure IV.4c). Even after increasing the silver loading to 5 wt% (2Ag5Ta-SiO_2), silver nanoparticles dispersion remains similar (Figure IV.5).

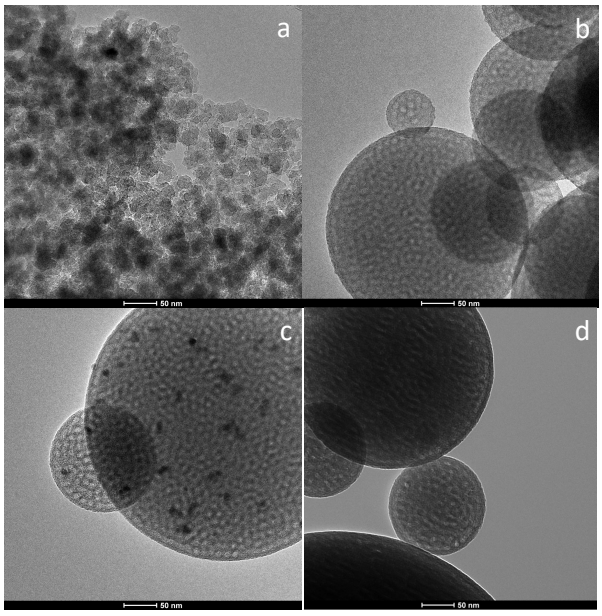

Figure IV.3: TEM images of 1Ag5Ta/SiO_2-A (a), 1Ag5Ta/SiO_2 (b), 1Ag/5TaSiO_2 (c), 1Ag5Ta-SiO_2 (d).

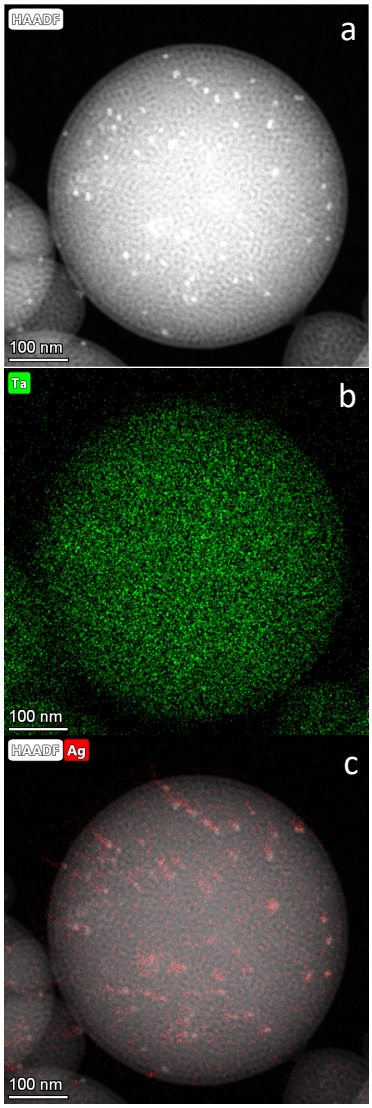

Figure IV.4: Electron microscopy analysis of 1Ag5Ta-SiO_2: (a) STEM ; (b) STEM-EDS of Ta ; (c) STEM-EDS of Ag.

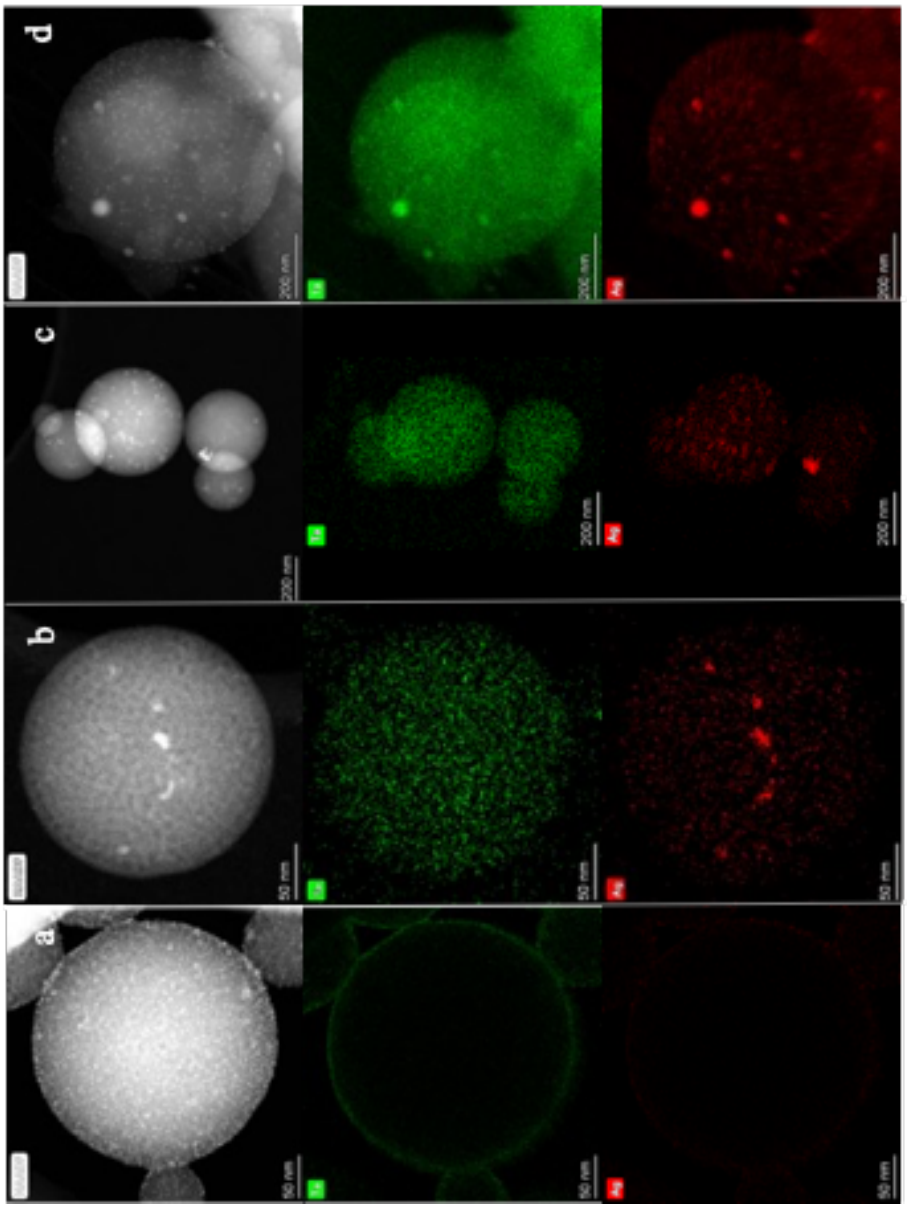

Figure IV.5: STEM-EDS analysis of 1Ag5Ta/SiO_2 (a), 1Ag/5TaSiO_2 (b), 1Ag5Ta-SiO_2 (c), 5Ag2Ta-SiO_2 (d).

Consistently, XRD shows Ag nanoparticles of around 14 nm (Figure IV.6, the Scherrer equation was used on 2 diffraction peaks to obtain 12 nm from 2θ=36 and 16 nm for 2θ=38). It should be noted that the uncalcined materials already contain some Ag nanoparticles of smaller size (~8 nm from the Scherrer equation, see Figure IV.7). Upon calcination, the silver ions

and/or the small silver nanoparticles that are dispersed in the silica matrix sinter to stabilize in the form of ~15 nm sized Ag crystallites. Importantly, the Ag crystallite size remains stable with increasing silver loadings (1, 2 and 5 wt %, see Figure IV.6). Furthermore, the presence of tantalum does not influence the size of Ag nanoparticle; for example, by doubling the tantalum loading from 1 to 2 wt.% coupled with 5 wt.% Ag, the crystallite size remains constant at around 14 nm, (Figure IV.6). Thus, a good dispersion of silver is maintained even at relatively high loadings. It is noted that the broad diffraction signal around 2θ=23 up until 38 is attributed to silica.

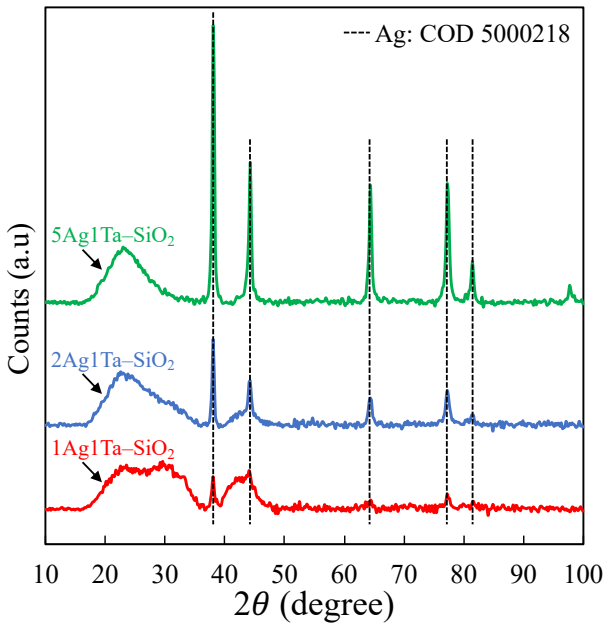

Figure IV.6: XRD diffractograms of catalysts containing different silver loadings.

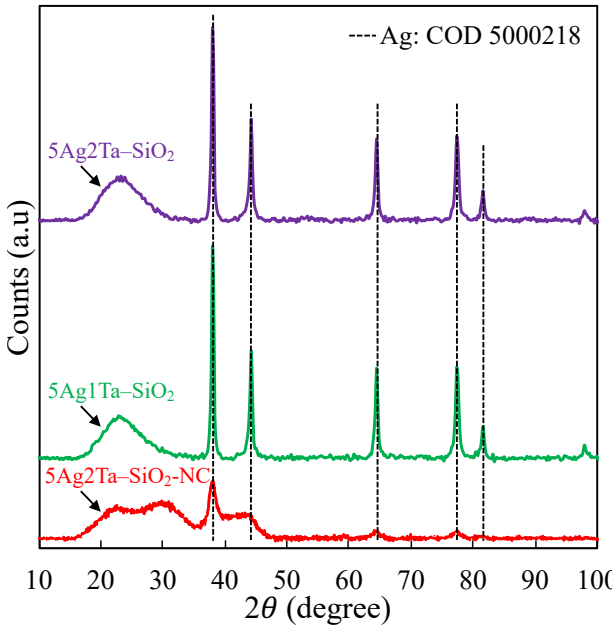

Figure IV.7: XRD data for 5Ag1Ta-SiO_2 (green); 5Ag2Ta-SiO_2 (purple); uncalcined 5Ag2Ta-SiO_2 (red).

FTIR spectra were very similar for all catalysts, with the typical main absorption bands originating from the silica matrix (Figure IV.8).[206-210] The band at 750-850 cm^{-1} was attributed to the symmetric vibration of Si–O–Si bonds whereas the most intense absorption band at 1050-1065 cm^{-1} was ascribed to the antisymmetric stretching vibration of Si–O–Si. The distinct shoulder at 1170-1220 cm^{-1} was due to SiO_4 and their external linkage. The two bands at 1580-1660 cm^{-1} and 3000-3700 cm^{-1} were respectively assigned to the bending of H–O–H bonds and the stretching of O–H bonds. Interestingly, catalysts with Ta incorporated through the aerosol process displayed an additional distinct band at 950 cm^{-1} (Figure IV.9). This band corresponds to the Si–O–Ta stretching mode.[211,212] It suggests that tantalum was effectively incorporated into the silica matrix through the AASG process. Furthermore, the intensity of the band can be correlated with the tantalum loading (Figure IV.10). As expected, this band is absent in the pristine silica. Strikingly, this band is not found in the impregnated catalysts (where TaO_x is deposited on the silica surface rather than incorporated in the silica matrix). Thus, FTIR spectroscopy points to a very different environment for Ta, depending on the preparation mode.

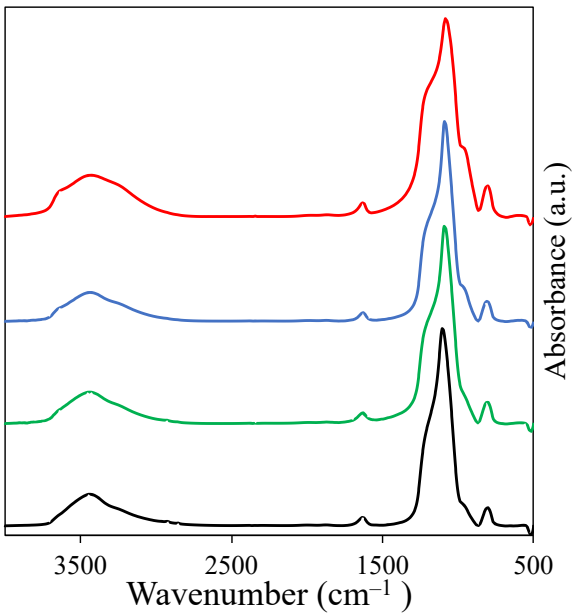

Figure IV.8: IR spectra of (from bottom to top) 1Ag5Ta/SiO_2-A (black); 1Ag5Ta/SiO_2 (green); 1Ag/5TaSiO_2 (blue); 1Ag5Ta-SiO_2 (red).

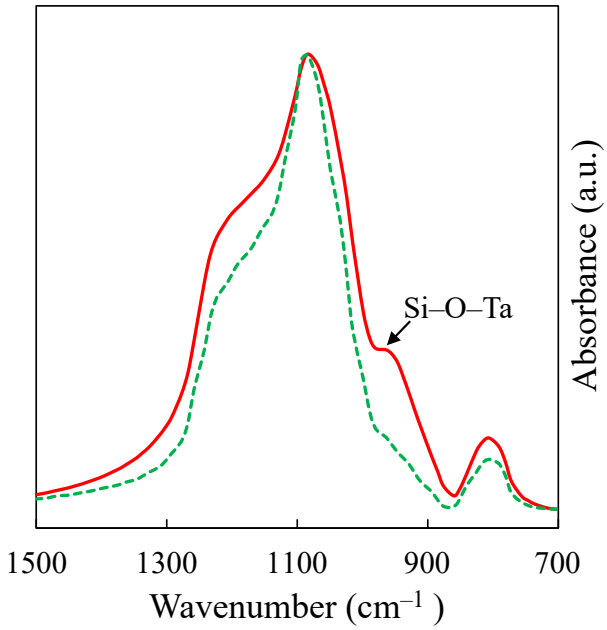

Figure IV.9: FTIR Spectra obtained on 1Ag5Ta-SiO_2 (solid red line), 1Ag5Ta/SiO_2 (broken green line).

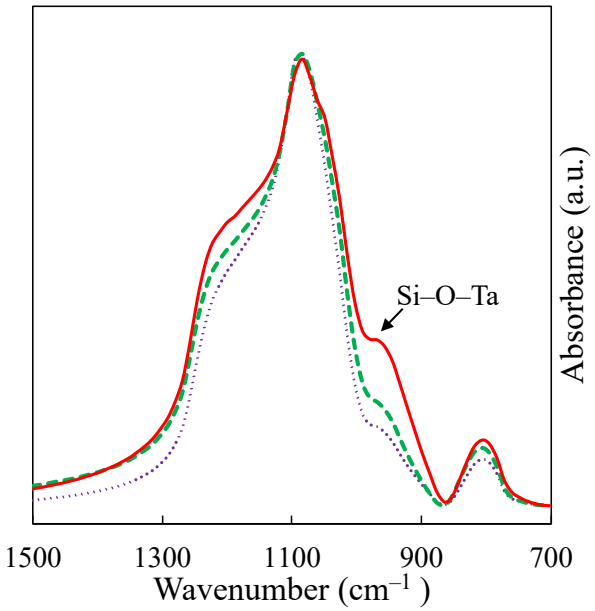

Figure IV.10: FTIR Spectra obtained on 2Ag/2Ta-SiO_2 (dotted purple line), 2Ag/5Ta-SiO_2 (broken green line), 2Ag/10Ta-SiO_2 (solid red line).

Here, NH_3-TPD measurements (Table IV.1) complement FTIR by bringing to light higher acidity for samples with Ta incorporated through the aerosol process (e.g. +71 % for 1Ag5Ta-SiO_2, compared to 1Ag5Ta/SiO_2, see Figure IV.11 and Table IV.1). Going further and looking at the identity of those acid sites, pyridine adsorption followed by FTIR measurements were also performed (Figure IV.12). After pyridine desorption at 150 °C, Tantala-silica synthesized via the aerosol process reached a Lewis acidity of 19.9 µmol g^{-1} compared to 16.3 µmol g^{-1} for impregnated Ta. The higher Lewis acidity for 2Ta-SiO_2 can be explained for the difference in Ta conformation inside the silica matrix. Si–O–Ta bonds shown in IR should be more acidic than polymeric TaOx species because of the higher Ta dispersion. This higher dispersion translates into a higher accessibility and thus justifies the difference in Lewis acidity between both samples. No significant Bronsted acidity was observed for both catalysts. We note that a more precise description of the acidic sites formed by the Ta-O-Si species in aerosol catalysts could usefully be obtained via dedicated CO-FTIR experiments.[123,213]

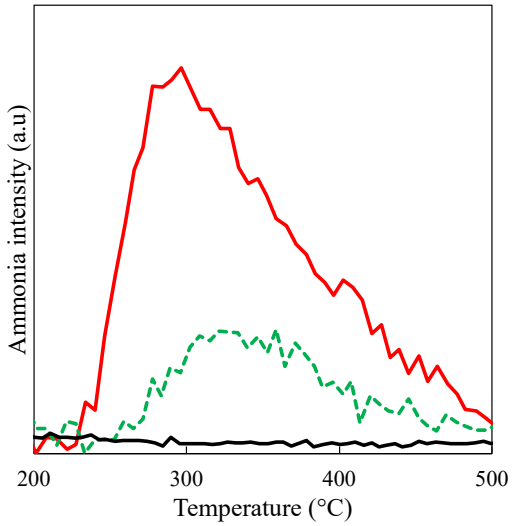

Figure IV.11: NH_3-TPD profile of 1Ag/5Ta-SiO_2 (solid red line) and 1Ag5Ta/SiO_2 (dotted green line). Solid black line is pure spray-dried silica.

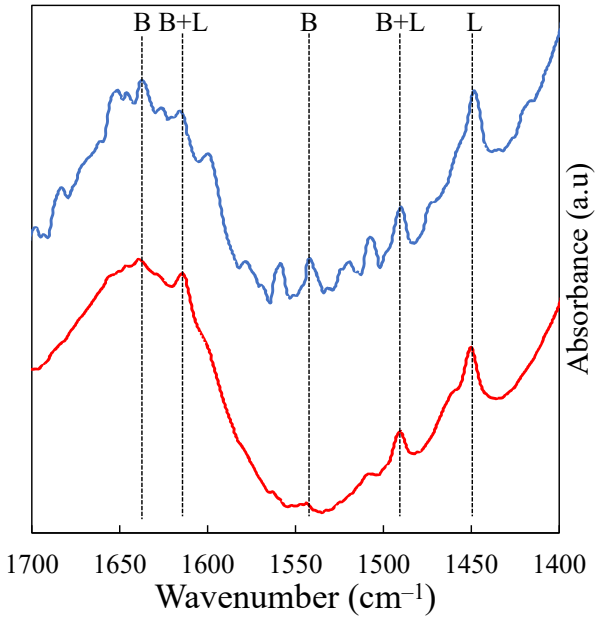

Figure IV.12: FTIR spectra after pyridine adsorption and evacuation at 150 °C of 2Ta-SiO_2 (bottom red curve) and 2Ta/SiO_2 (top blue curve). B= band corresponding to Bronsted acid sites ; L= band corresponding to Lewis acid sites.

Altogether, these characterization results substantiate the benefits of the AASG method. Both FTIR and NH_3-TPD point to the fact that homogeneously dispersed Ta within the silica matrices through AASG displays higher acidity compared to polymeric TaO_x surface species, predominant in the impregnation process. However, the high acidity of AASG catalysts also leads to a high selectivity towards dehydration products (ethylene and diethylether) (Table IV.2). Very similar results were previously obtained via the non-hydrolytic sol-gel (NHSG) process.[7,214] NHSG catalysts displayed higher acidity leading to higher production of ethylene. An important take away message is that AASG represents a reliable method to obtain highly dispersed Ta species in silica matrices. Concomitantly, the dispersion of Ag nanoparticles and the texture are maintained for the various compositions that have been explored.

4.3.3 Optimizing the catalyst composition to boost butadiene yield

In an attempt to understand the influence of acid and redox sites on the butadiene yield and selectivity, and to ultimately mitigate the formation of unwanted by-products observed with 1Ag5Ta-SiO_2, loadings of Ta and Ag have been modified (Table IV.4). Interestingly, the method allows tuning the composition without modifying the textural properties (Figure IV.13 and Table IV.3) or the active sites dispersion (Figure IV.5). Indeed, a similar mesoporous texture is obtained for all catalysts, even at high loading, with constant pore sizes (Figure IV.13). Table IV.3 shows that the doubling of Ta loading from 1 to 2 wt % strongly decreases the mesoporous volume, potentially explained by an interaction between the silica and the Ta precursors and F127, perturbing the concomitant processes of micelles formation and inorganic polycondensation reactions. The increase in Ag loading does not significantly modify the mesoporous volume and the average mesopore diameter (Table IV.3), implying that the decrease in SSA could be due to a disruption in the polycondensation, leading to different rugosity on the silica's surface.

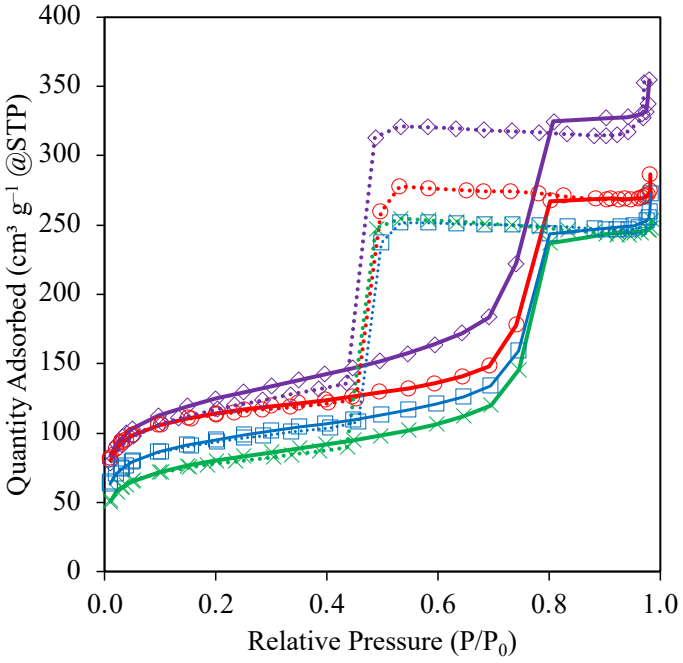

Figure IV.13: N_2-physisorption isotherms of 1Ag1Ta-SiO_2 (purple ◊), 1Ag2Ta-SiO_2 (red ○), 2Ag2Ta-SiO_2 (blue ■), 5Ag2Ta-SiO_2 (green ×).

Table IV.3: Textural properties (N_2-physisorption) of various Ag-Ta catalysts.

Sample	S_{BET} ($m^2\ g^{-1}$)	V_{meso} ($cm^3\ g^{-1}$)[a]	D_{meso} (nm)[b]
1Ag1Ta-SiO_2	460	0.46	8.5
1Ag2Ta-SiO_2	430	0.31	9.0
2Ag2Ta-SiO_2	350	0.33	9.3
5Ag2Ta-SiO_2	300	0.33	8.9

[a] calculated as ((total pore volume) – (micropore volume)), [b] calculated as $4V_{meso}/A_{meso}$

By decreasing the tantalum loading (1Ag1Ta-SiO_2), the overall ethanol conversion was lowered, together with the ethylene and diethylether selectivity. This confirms that Ta acid sites are responsible for the formation of these dehydration by-products. In conjunction to this, the dehydrogenation activity of the catalyst was increased, as shown by the significant increase in acetaldehyde selectivity, from 17 to 52 %. Nevertheless, BD selectivity remained very low (< 1 %). By increasing the Ag loading to 2 and 5 wt.%, BD selectivity increased only to ca. 6 %. Still, the acetaldehyde yield reached 43 %, a sign that the catalyst lacks the ability to effectively convert acetaldehyde to crotonaldehyde over the appropriate acid sites. To overcome this issue, the Ta loading was also increased (to 2 wt.%). Combined with 1 wt.% of Ag, acetaldehyde yield sat at 13.5 % whereas dehydration by-

products (ethylene, diethylether) reached a combined yield of ca. 15 %, a sign that the catalyst demonstrates balanced dehydration and dehydrogenation activities. Yet, BD selectivity remained under 1 %. With the increase of the Ag loading to 2 and 5 wt.%, BD yields rose respectively to 9.4 and 15.1 %. In parallel, selectivity towards dehydration by-products was gradually decreased. When considering the overall effect of the Ta loading, its increase systematically led to an increase in BD selectivity combined with a decrease in acetaldehyde selectivity. This is consistent with previous claims of the importance of the presence Ta–O–Si species to catalyse the aldol condensation step and confirms the importance of this step in the overall mechanism of the reaction. But in all tested catalysts, no traces of crotonaldehyde or crotyl alcohol were observed, further indicating that the MPV reduction and the final dehydration of crotyl alcohol to 1,3-butadiene are not limiting in the case of acid catalysts. However, the accumulation of unconverted acetaldehyde can indicate a slower reaction rate for the aldol condensation.

Thus, we show that adapting the absolute and relative loadings of the redox and acidic functions in these bifunctional catalysts can be done easily via AASG and can be used to drive the process towards the desired product. Within the series of catalysts presented in Table IV.4, the formulation with 2 wt.% Ta and 5 wt.% Ag appears to present the most suitable balance between acid and redox sites, leading to a relatively high BD yield.

Table IV.4: Catalytic conversion of ethanol, yield and selectivity of butadiene and by-products; Reaction conditions T=355 °C, WHSV=1.10 h^{-1}, TOS=3 h.

Catalyst	Ethanol conversion (%)	Butadiene (%)		Acetaldehyde (%)		Ethylene (%)		Diethylether (%)		Others (%)	
		Yield	Sel	Yield	Sel	Yield	Sel	Yield	Sel	Yield	Sel
1Ag5Ta/SiO_2-A	43.5	6.9	15.9	20.1	46.2	3.6	8.4	7.0	16.0	5.9	13.6
1Ag5Ta-SiO_2	80.6	1.8	2.2	13.9	17.2	46.3	57.4	3.3	4.1	15.3	19.0
1Ag1Ta-SiO_2	46.7	0.3	0.7	34.9	74.7	1.9	4.0	0.8	1.7	8.8	18.8
2Ag1Ta-SiO_2	68.3	1.5	2.2	52.6	76.9	4.3	6.4	0.5	0.8	9.3	13.6
5Ag1Ta-SiO_2	84.6	5.3	6.2	52.4	61.9	5.3	6.2	0.4	0.4	21.4	25.3
1Ag2Ta-SiO_2	45.8	1.1	2.3	16.3	35.6	13.0	28.4	3.5	7.7	11.9	26.0
2Ag2Ta-SiO_2	69.7	9.4	13.6	30.6	43.9	13.9	19.9	3.9	5.5	11.9	17.1
5Ag2Ta-SiO_2	86.6	15.1	17.4	35.9	41.4	11.4	13.2	2.1	2.4	22.2	25.6

Others: propylene, butenes,

4.3.4 Pushing the butadiene production

With the best catalyst in hands (5Ag2Ta-SiO_2), we attempt to boost the process by playing with operational parameters. In particular, temperature plays a role in both the overall ethanol conversion and the reaction products distribution (Table IV.5). The lower temperature of 325 °C gives the lowest ethanol conversion and tends to favor acetaldehyde, with a selectivity above 50 %. When switching to higher temperatures, ethanol conversion increases to values above 80 %, along with a higher selectivity towards dehydration by-products, 15 % and 25 % for 355 °C and 385 °C respectively. Thus, it means that the redox power of the catalyst is favored at lower temperatures (high acetaldehyde selectivity), whereas the dehydrating features are dominant at higher temperatures (high ethylene + diethylether selectivities). The optimum is found at 355 °C with the highest butadiene selectivity (ca. 18 %) among the tested temperatures. At this temperature, a correct balance is achieved between the redox and acidic properties to efficiently obtain butadiene while maintaining dehydration by-products at a low level.

Secondly, the weight hourly space velocity (WHSV) is known to play a major role in the catalyst performance, since a network of inter-dependent reactions is involved.[7] Here, a linear relationship between the WHSV and the butadiene selectivity was highlighted (Figure IV.14a). Concomitantly, the acetaldehyde selectivity increased when the WHSV increases. When the WHSV is low, the contact time is increased, giving more possibility to the newly produced acetaldehyde to undergo the self-condensation to the acetaldol, which will be further dehydrated to crotonaldehyde and finally butadiene. As the aldol condensation is often recognized in the literature as the rate-limiting step in the ETB mechanism,[84,103] increasing the odds of achieving it yields more butadiene. On the contrary, when the WHSV is increased, the amount of unreacted acetaldehyde logically rises.

Figure IV.14b shows the influence of the WHSV on the products distribution. At WHSV below 0.5 h^{-1}, the most abundant product is butadiene, with a maximum yield of 24 %. At WHSV of 1.12 h^{-1} and 2.24 h^{-1}, ethylene and acetaldehyde are the most abundant products. Since ethylene is the result of a fast dehydration of ethanol on acid sites and acetaldehyde is the product of direct dehydrogenation of ethanol on redox sites, these two compounds are favored at lower contact time in comparison to BD.

In terms of productivity, 5Ag2Ta-SiO_2 reaches 0.085 g_{BD} g_{cat}^{-1} h^{-1} at WHSV=1.12 h^{-1}. This is lower than the record performance reached with other

catalytic systems, such as Zn-Zr based zeolites.[93,115,120] However, higher ethanol conversion and similar butadiene yields are obtained with the best AASG-made catalyst, when comparing with other Ag/silica-based systems reported in the literature.[105,215] It must be recalled that the AASG is a straightforward one step, low waste preparation method that compares favorably to classical multistep catalyst preparation processes.

Table IV.5: Catalytic conversion of ethanol, yield and selectivity of butadiene and by-products in function of the temperature; Reactions conditions: WHSV=1.10 h^{-1}.

Catalyst	Ethanol conversion (%)	Butadiene (%)		Acetaldehyde (%)		Ethylene (%)		Diethylether (%)		Others (%)	
		Yield	Sel	Yield	Sel	Yield	Sel	Yield	Sel	Yield	Sel
5Ag2Ta-SiO_2 325 °C	68.6	8.5	12.3	36.6	53.4	6.8	9.9	3.6	5.3	13.1	19.1
5Ag2Ta-SiO_2 355 °C	86.6	15.1	17.4	35.9	41.4	11.4	13.2	2.1	2.4	22.2	25.6
5Ag2Ta-SiO_2 385 °C	84.1	9.0	10.7	28.6	34.0	3.6	8.4	7.0	16.0	5.9	13.6

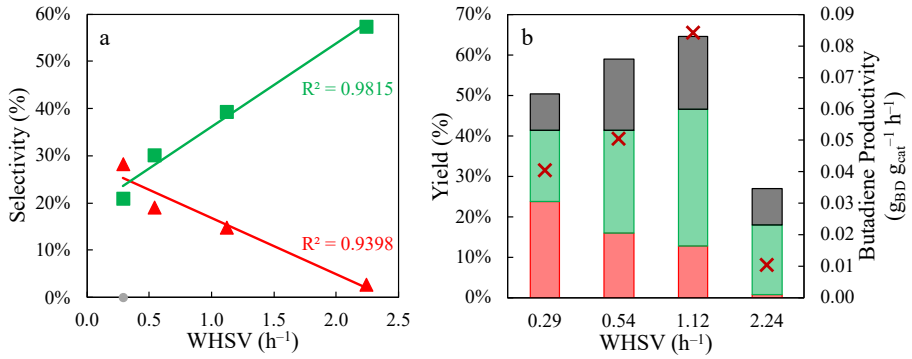

Figure IV.14: (a) Influence of the WHSV on the butadiene (▲) and acetaldehyde selectivity (■) for 5Ag2Ta-SiO_2 at 355 °C; (b) (from bottom to top) Butadiene yield (red), acetaldehyde yield (green), ethylene yield (black) and butadiene productivity (×) as a function of the WHSV for 5Ag2Ta-SiO_2 at 355 °C.

4.4 Conclusion

The aerosol-assisted sol-gel method allows obtaining, in one step, highly homogeneous bifunctional AgTa-SiO_2 catalysts with advantageous mesoporous texture (large pore volumes and relatively high specific surface area). Characterization data displays a high degree of insertion of dispersed Ta species in the silica matrices, resulting in an acidic catalyst producing markedly more dehydration by-products compared to impregnated tantalum

oxide. With the addition of well dispersed Ag nanoparticles, we are able to obtain butadiene from ethanol. Upon optimization of the Ta and Ag loadings it is possible to temper the dehydration activity, while increasing the dehydrogenation activity and maintaining sufficient acidity to complete the cascade reactions towards butadiene. We show that playing with the reaction conditions (in particular reaction temperature and contact time) allows further boosting the butadiene yield, up to 23 %.

To make the link with the research questions mentioned in the objectives, the aerosol-assisted sol-gel allowed us to control the nature of the Ta active sites, yielding inserted Ta in the silica matrix in a one-step synthesis protocol (question (i)). Furthermore, we managed to mitigate the production of by-products by controlling the relative abundance of the two types of active sites and by so, adjusting the redox and acidic properties of our material (question (ii)).

CHAPTER 5: Aerosol-assisted sol-gel synthesis of Cu–Ta catalysts: optimization of formulation and catalytic performance

Aerosol-assisted sol-gel synthesis of Cu–Ta catalysts: optimization of formulation and catalytic performance

5.1 Abstract

In this second chapter, we improve upon previous results by replacing Ag with Cu in the AASG process. Cu-Ta-SiO_2 catalysts keep an open mesoporous texture with specific surface areas in the 520–660 $m^2\ g^{-1}$ range, pore volumes between 0.48 and 0.67 $cm^3\ g^{-1}$, and average pore diameters around 4 nm. In addition to that, isolated Ta acid sites and dispersed small Cu nanoparticles are obtained and evidenced by characterisation techniques such as FTIR, NH_3-TPD, XPS, XRD, TEPO-NMR, ToF-SIMS and STEM-EDS. After optimization of Ta and Cu loadings, diffusion limitations are assessed and deemed absent, and a study of different reaction parameters is carried out. It is shown that a reaction temperature of 350 °C is best suited to maximize BD selectivity. In addition to that, a pre-reduction temperature of 200 °C improves catalytic performance but not the stability of the catalyst. Finally, co-feeding 0.13 % of oxygen in the reaction stream boost significantly BD yields and stability and allow for an impressive 0.38 $g_{BD}\ g_{cat}^{-1}\ h^{-1}$ BD productivity, attributed to the constant removal or formation hindering of coke by diluted oxygen on the active sites surface. A BD yield of more than 30 % was kept over 24 hours in the same conditions.

5.2 Introduction

On the one hand, AASG has already proven effective for the synthesis of mixed oxide catalysts[166,167,216] and supported metal nanoparticles,[170-172] and bifunctional catalysts featuring both dispersed oxide species and small metal nanoparticles.[126] On the second hand, Cu was already shown to display higher dehydrogenation activity as compared to Ag.[7,114] This is important because we showed in the previous Chapter that the overall performance in the ETB reaction is strongly governed by the dehydrogenation activity. Thus, we study here the possibility of synthesizing mesoporous Cu-Ta-SiO_2 catalysts via the AASG process, to be exploited in the ETB reaction. In the specific case of the Cu-Ta pair, recent literature also showed its superiority against Ag-Ta.[93,114]

5.3 Results and discussion

5.3.1 Characterizing Cu–Ta AASG catalysts

In these following paragraphs, we present and discuss the influence of the Ta and Cu loadings on the bifunctional catalysts' key properties.

Figure V.1 shows type IV isotherms thus primarily mesoporous textures for all catalysts. Specific surface areas (SSA) range from 520 to 660 $m^2\ g^{-1}$, and the catalysts feature large mesopores volumes between 0.37 and 0.52 $cm^3\ g^{-1}$ and an average mesopore diameter around 7 nm (Table V.1). When the Ta loading is kept constant at 2 wt.% and the Cu loading is gradually increased from 2 to 6 wt.%, the mesoporous volume of the resulting catalyst is decreased from 0.52 to 0.38 $cm^3\ g^{-1}$ (Table V.1). Similarly, a slight decrease in the mean mesopore diameter is observed, from 7.4 to 4.8 nm (Table V.1). The hysteresis in the N_2 physisorption isotherms and the corresponding BJH pore size distribution clearly indicate the presence of mesopores with a relatively narrow size distribution centred on ~8 nm (which is consistent with the templating effect of F127 micelles).

The same protocol was followed, keeping the Cu loading constant at 4 wt.% but increasing the Ta content from 1 to 4 wt.%. Marginal reductions in SSA, pore volume and average pore diameter are noticed as the catalyst contains more Ta (Figure V.1b and Table V.1).

Si/Cu ratios obtained by XPS logically decrease as the Cu loading rises (Table V.1), from 98 for 2Cu2Ta-SiO_2 to 38 for 6Cu2Ta-SiO_2. Compared to theoretical values, experimental Si/Cu is systematically higher, indicating a tendency of the spray-drying process to concentrate Cu species in the bulk of the SiO_2 particles. At constant Ta loading, whatever the Cu loading, the surface Si/Ta ratio remains very stable, higher than the nominal.

Naturally, in the series of catalysts with constant Cu loading and increasing Ta loading (4CuXTa-SiO_2), the surface Si/Ta ratio decreases from 100 for 4Cu2Ta-SiO_2 to 64 for 4Cu4Ta-SiO_2. The fact that the experimental Si/Ta ratio sits lower than the nominal values, indicates that the surface of the mixed oxide is slightly richer in Ta than the bulk. Interestingly, when the loading of one active element is modified while the other remains constant, the spatial distribution of the latter appears to be unchanged.

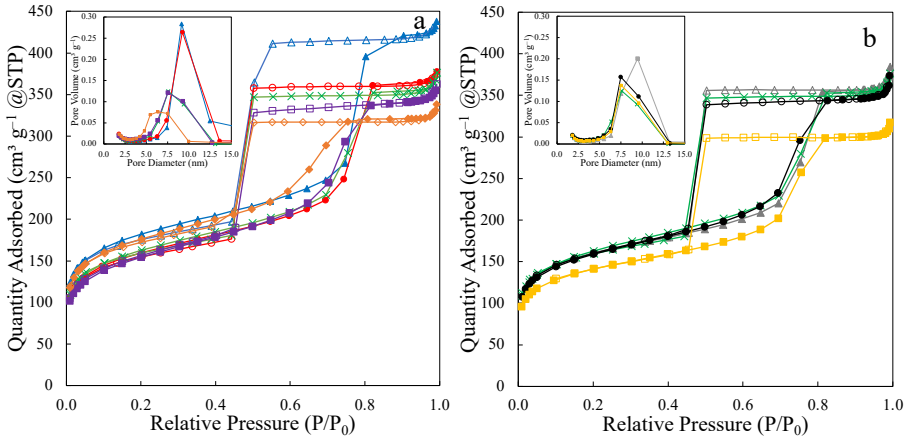

Figure V.1: (a): N_2-physisorption isotherms and BJH pore size distribution profiles measured on the adsorption (inset) of 2Cu2Ta-SiO_2 (blue Δ), 3Cu2Ta-SiO_2 (red ○), 4Cu2Ta-SiO_2 (green ×), 5Cu2Ta-SiO_2 (purple ■), 6Cu2Ta-SiO_2 (orange ◊) ; (b) : N_2-physisorption isotherms of 4Cu1Ta-SiO_2 (grey Δ), 4Cu2Ta-SiO_2 (green ×), 4Cu3Ta-SiO_2 (black ○), 4Cu4Ta-SiO_2 (yellow ■)
Adsorption isotherms are plotted as solid lines, desorption isotherms are plotted as dotted lines.

Table V.1: Textural properties (N_2-physisorption), surface composition analysis (XPS).

Sample	S_{BET} ($m^2\ g^{-1}$)	V_{meso} ($cm^3\ g^{-1}$)[a]	D_{meso} (nm)[b]	Surface Si/Ta[d]	Surface Si/Cu[d]
2Cu2Ta-SiO_2	660	0.52	7.4	90 (151)	98 (53)
3Cu2Ta-SiO_2	580	0.45	6.9	80 (151)	80 (35)
4Cu2Ta-SiO_2	590	0.40	6.7	85 (151)	51 (26)
5Cu2Ta-SiO_2	560	0.45	6.2	78 (151)	45 (21)
6Cu2Ta-SiO_2	570	0.38	4.8	80 (151)	38 (18)
4Cu1Ta-SiO_2	570	0.44	7.8	100 (301)	56 (26)
4Cu3Ta-SiO_2	580	0.42	6.9	69 (100)	46 (26)
4Cu4Ta-SiO_2	520	0.37	6.9	64 (75)	68 (26)

[a] calculated as ((total pore volume) – (micropore volume)), [b] calculated as $4V_{meso}/A_{meso}$ [c] Determined by ICP; [d] Determined by XPS, theoretical values between brackets

NH_3-TPD measurements show no significant influence of the Cu loading on the total acidity of the catalyst (Table 2), staying in the range 2.4-2.8 10^{-1} mmol g^{-1} of acid sites for catalysts with 2 wt.% Ta. Expectedly, the total acidity is related to the Ta loading, and it increases from 1.6 10^{-1} mmol g^{-1} for 4Cu1Ta-SiO_2 to 5.0 10^{-1} mmol g^{-1} for 4Cu4Ta-SiO_2. Such results indicate that Cu is not significantly interfering with the Ta active sites to alter the acidic properties and Ta is the only active element responsible for the acidity of the catalyst. Table V.6 assesses the strength of those active sites and all studied

catalysts show a similar thermogram, with a maximum of NH_3 desorption around 250 °C, showing a similar strength of Ta active sites.

Table V.2: Acidity measurements on spray-dried samples.

Sample	Total acidity (mmol g^{-1})[a]
2Cu2Ta-SiO_2	2.4 10^{-1}
4Cu1Ta-SiO_2	1.6 10^{-1}
4Cu2Ta-SiO_2	2.8 10^{-1}
4Cu4Ta-SiO_2	5.0 10^{-1}

[a] Determined by NH_3-TPD

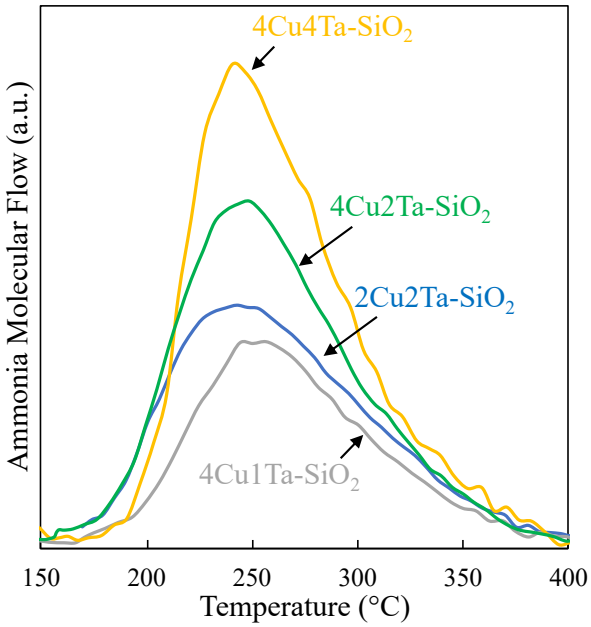

Figure V.2: NH_3-TPD of (from bottom to top curve) 4Cu1Ta-SiO_2 (grey), 2Cu2Ta-SiO_2 (blue), 4Cu2Ta-SiO_2 (green) and 4Cu4Ta-SiO_2 (yellow).

Additional measurements by ^{31}P MAS NMR on chemisorbed triethylphosphine oxide (TEPO) were conducted. Since this molecule is basic, it will adsorb preferentially on acid sites. The analysis reveals a main peak at 66 ppm and a smaller one at 101 ppm (18 and 114 are attributed to spinning side bands) (Figure V.3).[217] Here, the higher the chemical shift, the higher the interaction between TEPO and Ta (acid site) is.[217] Based on previous studies, the peak at 66 ppm is attributed to the interaction between TEPO and surface silanols group.[218] Based on this, the peaks at 54 and 81 ppm are supposedly weaker and stronger silanol groups respectively, potentially due to different

environments in the close vicinities of the silanol groups. By increasing the Cu loading for 4 to 6 wt %, the relative concentration of the peak around 54 ppm increases from around 9 to 16 %. This could indicate a small contribution of Cu to the acidity of the catalyst, especially weak acid sites. Furthermore, when increasing the Ta loading from 2 to 4 wt %, the relative concentration of the 101 ppm peak increases from 8.1 to 9.7 %. The origins of the signal at 101 ppm could be silica-inserted Ta species.

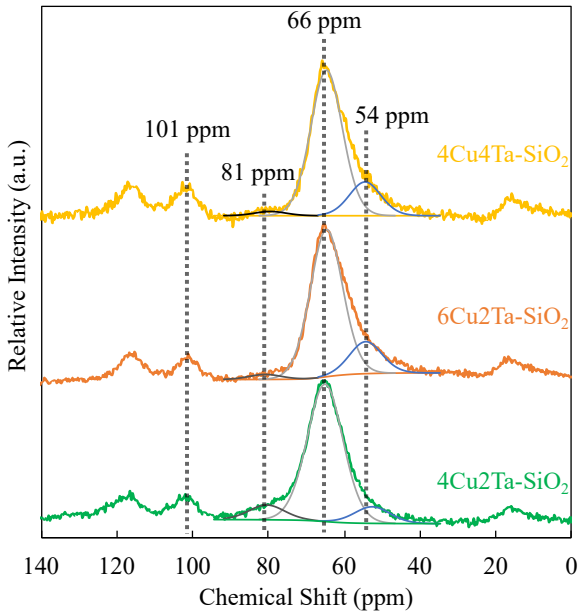

Figure V.3: ^{31}P MAS NMR spectra collected after triethyl phosphine oxide chemisorption; peaks at 18 ppm and 114 ppm represent spinning side bands.

Table V.3: ^{31}P MAS NMR spectra deconvolution data of the 66 and 101 ppm peaks.

Catalyst	Chemical Shift (ppm)	Relative Concentration (%)
4Cu2Ta-SiO$_2$	101.8	8.10
	80.4	8.04
	65.0	74.8
	52.6	9.03
6Cu2Ta-SiO$_2$	101.4	7.68
	80.8	2.51
	64.7	73.8
	54.3	16.1
4Cu4Ta-SiO$_2$	102.0	9.67
	79.5	2.09
	64.6	71.6
	54.5	16.6

IR analysis on pellets made with KBr showed very similar spectra for all catalysts, with the main absorption bands originating from the SiO_2 matrix (Figure V.4).[206-210] The small band at 750-850 cm^{-1} was attributed to the symmetric vibration of Si–O–Si bonds whereas the most intense absorption band at 1050-1065 cm^{-1} was ascribed to the antisymmetric stretching vibration of Si–O–Si. The distinct shoulder at 1170-1220 cm^{-1} was due to SiO_4 and their external linkage. The two bands at 1580-1660 cm^{-1} and 3000-3700 cm^{-1} were respectively assigned to the bending of H–O–H bonds and the stretching of O–H bonds.[206-210] Interestingly, catalysts with Ta incorporated through the aerosol process displayed a distinct additional distinct band at 950 cm^{-1}. This band corresponds to the Si–O–Ta stretching mode.[211,212] It suggests that the aerosol-assisted sol-gel process has allowed the effective incorporation fo Ta oxide into the silica matrix. The intensity of the FTIR band can be correlated to the Ta loading in the catalyst (Figure V.4b). Furthermore, Figure V.4a shows no significant influence of the Cu loading on the intensity of the band at 950 cm^{-1}, indicating that Cu does not influence the insertion of Ta in the silica matrix.

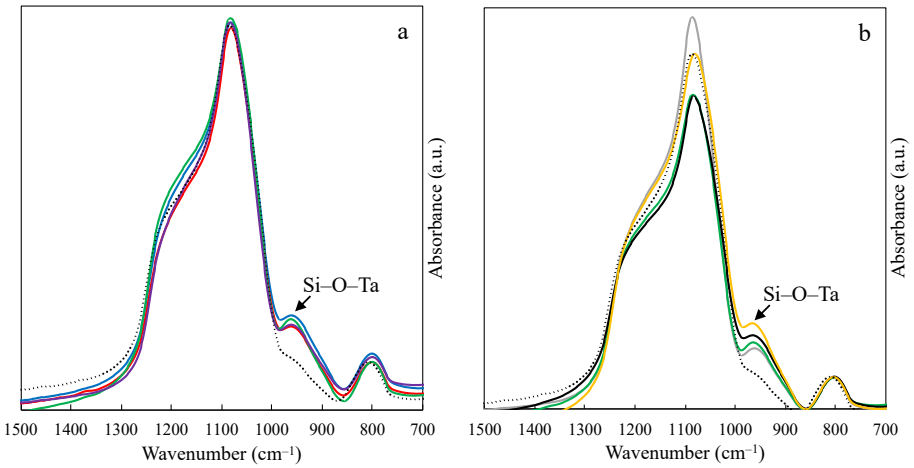

Figure V.4: FTIR spectra on KBr pellets of (a) Cu screening and (b) Ta screening. (a) Dotted black curve is pure silica made by AASG.

ToF-SIMS was used to further study the insertion of Ta in the silica matrix in relation to the total amount of Ta introduced in our synthesis process (Figure V.5). The signals attributed to mixed clusters of Ta and Si (i.e. $TaOSi^+$, TaO_2Si^+, TaO_4Si^- and TaO_5Si^-, m/z = 225, 241, 273, 289 respectively) are taken as proxies for the insertion of Ta in the silica matrix. For each polarity, the sum of the intensity of mixed clusters was normalized by the total intensity of Ta-containing clusters in the same spectrum (Table V.9 in Appendix).

Figure V.5 presents the normalized the sum of the intensity of these mixed clusters for positive (a) and negative (b) spectra. Overall, these ratios show no difference between 4Ta-SiO_2, 4Cu4Ta-SiO_2 or 4Cu2Ta-SiO_2 further suggesting that nor the presence of Cu, nor the Ta loading influence the quality of the insertion of Ta in the silica matrix.

Figure V.5a represents the ratio of the sum of these “TaOSi” positively charged clusters over the total Ta cations. Figure V.5b exhibits a similar ratio but takes into account negatively charged ions and clusters. Overall, these ratios show no difference between 4Ta-SiO_2, 4Cu4Ta-SiO_2 or 4Cu2Ta-SiO_2 further confirming that nor the presence of Cu, nor the Ta loading influence the Ta integration in the silica matrix.

Figure V.6 complements other characterization techniques shown in this study by hinting at the spatial distribution indication of Ta when varying the loading in the bifunctional catalyst. Even though we double the nominal amount of Ta from 2 to 4 wt.%, no preferential accumulation of Ta into clusters was observed. Instead, Ta distribution remained homogeneous among the catalyst particles (Figure V.6b). These STEM-EDS results put to the forefront the fact that Ta remains well dispersed even at higher loadings and that its dispersion does not depend on the size of the spray-dried particles, an additional clue indicating the high homogeneity of active sites dispersion provided by the spray-drying process.

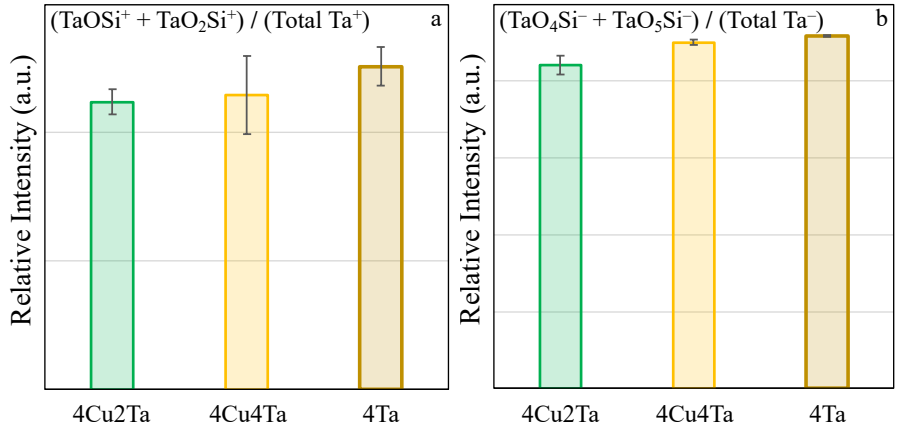

Figure V.5: ToF-SIMS Ratios of (a) positive ions ratio of Ta bonded to silica over the total amount of Ta ; (b) negative ions ratio of Ta bonded to silica over the total amount of Ta.

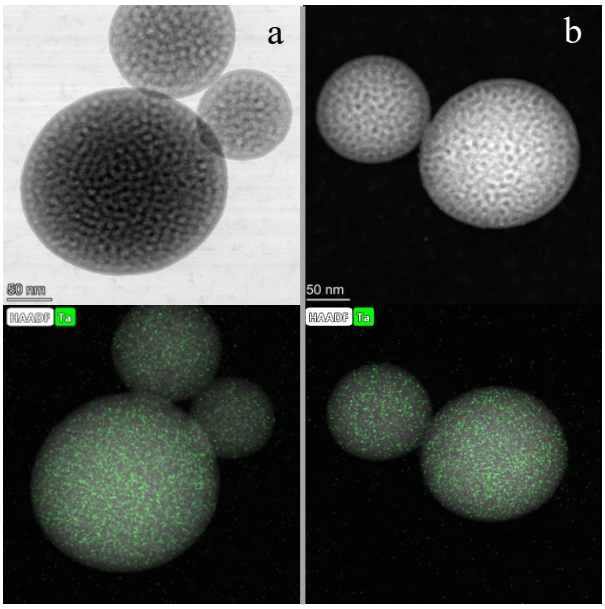

Figure V.6: STEM images of (a) 4Cu2Ta-SiO_2 ; (b) 4Cu4Ta-SiO_2. Bottom images represent the elemental mapping of Ta done by STEM-EDS.

Besides Ta, Cu dispersion can also be assessed by STEM-EDS (Figure V.7). In this case, the increase in Cu nominal loading from 2 to 6 wt.% induces the sintering of the larger nanoparticles. Indeed, even though 2Cu2Ta-SiO_2 displays well dispersed Cu species at 2 wt.%, 4Cu2Ta-SiO_2 starts to show signs of sintering of Cu particles at 4 wt.% and finally 6Cu2Ta-SiO_2 even proves advanced sintering of Cu nanoparticles, reaching sizes of ca. 50 nm.

Figure V.8a displays the diffraction patterns obtained on the bifunctional catalysts with different Cu loadings. The diffractions peaks at 2θ=36° and 38° correspond to CuO crystallites and become significant above a Cu loading of 3 wt.%. Interestingly, from 3 to 6 Cu wt.%, the CuO crystallite size remains in a close range between 10 and 14 nm (determined via the Scherrer equation on the 2θ=36° and 38° peaks), providing good indication of small well dispersed Cu nanoparticles in spray-dried catalysts, even at high nominal loadings. However, these values contradict STEM measurements for 6Cu2Ta-SiO_2. We can hypothesize that when CuO crystallites sinter, they agglomerate without changing their diffraction signature, leaving the XRD pattern unchanged. Thus, we form larger CuO nanoparticles composed of different small crystallites with separate XRD signals. The uneven shape of the nanoparticles (Figure V.7c) can also be the consequence of this uneven agglomeration. Figure V.8b suggests that the Ta loading has no effect on CuO crystallite size, remaining in the 10-12 nm range.

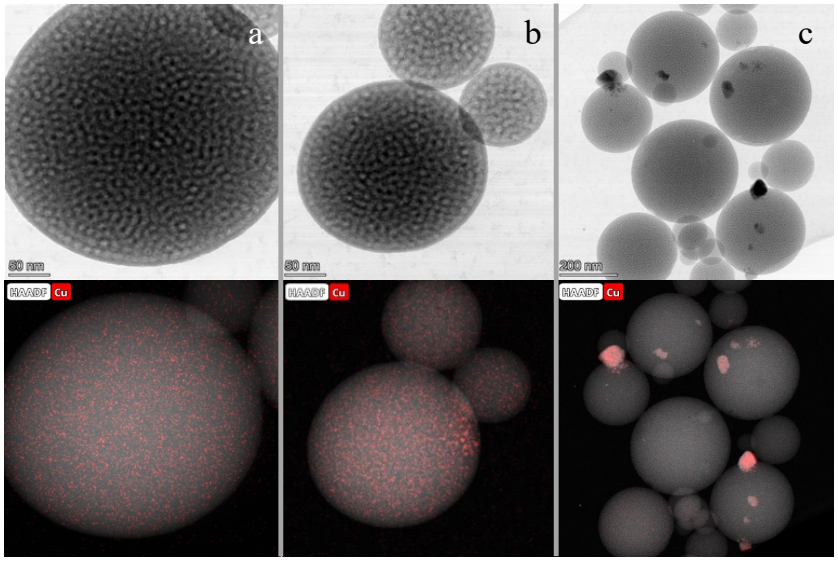

Figure V.7: STEM images of (a) 2Cu2Ta-SiO_2, (b) 4Cu2Ta-SiO_2, (c) 6Cu2Ta-SiO_2. Bottom images represent the elemental mapping of Cu done by STEM-EDS.

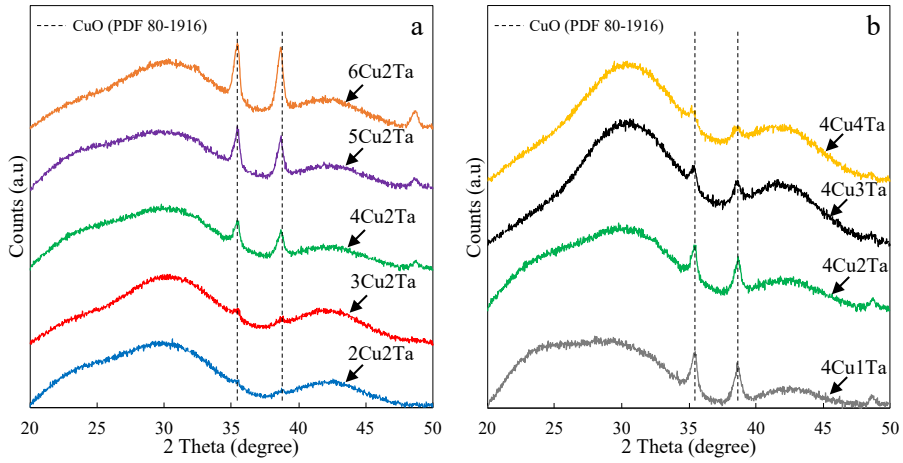

Figure V.8: (a): XRD data for (from bottom to top) 2Cu2Ta-SiO_2 (blue), 3Cu2Ta-SiO_2 (red), 4Cu2Ta-SiO_2 (green), 5Cu2Ta-SiO_2 (purple), 6Cu2Ta-SiO_2 (orange) ; (b) : XRD data for (from bottom to top) 4Cu1Ta-SiO_2 (grey), 4Cu2Ta-SiO_2 (green), 4Cu3Ta-SiO_2 (black), 4Cu4Ta SiO_2 (yellow).

5.3.2 Performance of Cu–Ta AASG catalysts in ETB

Catalytic data studying the influence of the copper loading on the catalytic performance of the bifunctional catalyst, targeting the production of butadiene is depicted in Table V.4. While keeping the Ta loading constant at 2 wt %, the Cu loading is gradually increased from 2 to 6 wt %. Ethanol conversion stays at around 90 %, at the exception of 2Cu2Ta-SiO_2 only reaching 65 %. Interestingly, acetaldehyde (AA) selectivity and ethylene selectivity are inversely proportional to the Cu loading. The decrease in EY selectivity is expected because of the lower accessibility of dehydration sites due to a higher Cu loading. However, we do reach an optimum of 41 % of BD yield at 4 wt % of Cu, already much better than Ag-Ta catalysts described in previous chapter and indicating a suitable balance between the two types of active sites. This balance can also be interpreted by an optimum reached between availability of Cu redox sites and their proximity with the Ta acid sites. Indeed, at Cu loadings above 4 wt %, the decrease in BD yield leads to consider a less active catalyst towards the dehydrogenation of ethanol to acetaldehyde, as shown by the decrease observed in AA selectivity (Table V.4). This is in line with STEM-EDS results on Figure V.6 where 6Cu2Ta-SiO_2 displayed much larger Cu nanoparticles, not ideal for catalytic performance.

The increase of Ta loading from 1 to 4 wt % systemically increased the BD selectivity, from 19 % for 1 wt % of Ta to more than 53 % for 4 wt % of Ta. Interestingly, the AA selectivity decreased at the same time. Thus, it can be concluded that a higher Ta loading enhanced the aldol condensation of AA, leading to higher BD selectivity. A 4 % of EY selectivity is obtained with 4Cu4Ta-SiO_2, a further sign that Ta sites are responsible for the direct dehydration of ethanol to ethylene. However, the EY selectivity remained low and does not hinder BD production. This way, the best formulation achieved a BD productivity of 0.28 $g_{BD}\ g_{cat}^{-1}\ h^{-1}$.

Table V.4: Catalytic performance of Cu-Ta catalysts; Reaction conditions T=325 °C, WHSV=1.10 h^{-1}, TOS=3 h.

Catalyst	Ethanol conversion (%)	Butadiene (%)		Acetaldehyde (%)		Ethylene (%)		Others (%)	
		Yield	Sel	Yield	Sel	Yield	Sel	Yield	Sel
2Cu2Ta-SiO_2	65.3	30.0	45.9	43.5	66.4	1.5	2.4	5.3	8.1
3Cu2Ta-SiO_2	87.6	40.6	46.3	52.8	60.3	0.9	1.1	0.2	0.2
4Cu2Ta-SiO_2	88.9	41.0	46.1	54.8	61.9	0.9	1.0	0	0
5Cu2Ta-SiO_2	87.3	39.7	45.5	51.5	59.0	1.0	1.1	0	0
6Cu2Ta-SiO_2	89.2	35.9	40.2	47.9	54.0	0.8	0.8	1.2	1.4
4Cu1Ta-SiO_2	87.1	16.9	19.4	68.9	79.3	0.2	0.2	1.0	1.1
4Cu2Ta-SiO_2	88.9	41.0	46.1	54.8	61.9	0.9	1.0	0	0
4Cu3Ta-SiO_2	90.6	45.1	49.8	60.4	66.7	0.1	0.2	0	0
4Cu4Ta-SiO_2	81.7	44.1	53.3	39.0	47.7	3.5	4.3	0	0

5.3.3 Assessing potential diffusion limitations

To assess if external diffusion limitations are present, several catalytic tests were performed at various ethanol flow rates by keeping the contact time and all other reaction conditions constant (i.e. changing the catalyst mass and the volumetric flow rate in a proportional way). A relatively high WHSV (short contact time) was chosen to ensure the ethanol conversion remained <100% (Figure V.9). In the presence of external diffusion limitations, lower catalytic masses (thus lower linear flows) would result in lower ethanol conversion due to the presence of a diffusion limit layer between catalysts particles that hinders the ethanol access to the active sites. In turns out all four catalytic tests display similar performance in terms of ethanol conversion, indicating that there is no external diffusion limitation. Here, sufficient turbulence is present at the surface of the catalysts particles to avoid the creation of this limit layer.

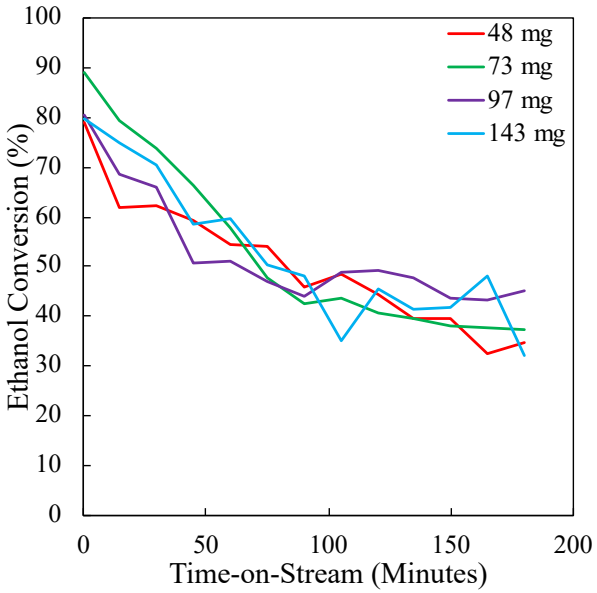

Figure V.9: Evolution of ethanol conversion in the ETB reaction over 4Cu4Ta-SiO_2 in relation to the mass of catalyst used. Reaction conditions: T=325 °C, WHSV=2.2 h^{-1}.

We also acknowledge the possible presence of internal diffusion limitations. Unfortunately, it is not easy to experimentally check this since the AASG process leads to a wide distribution of microspheres of various sizes, and it is difficult to vary this parameter in a systematic way (though it could be done, in principles, by varying the precursors solution concentration or by using specific tools to select particles in narrower size ranges). Similarly, testing various surfactants could have allowed to test catalysts with various pore size, but this was deemed unnecessary in the framework of this work. Indeed, theoretical calculations have allowed to exclude potential internal diffusion limitations. The Weisz-Prater number[130,219] allows verifying if the reaction rate is limited by internal diffusion limitations or not. Table V.5 summarizes all experimental parameters used in the methodology described by García-Sánchez to obtain the Weisz-Prater number.[219] First, the surface concentration C_s and the ethanol molar flow $F_{EtOH\text{-}0}$ are determined as followed:

$$C_{s-EtOH} = \frac{P_{EtOH}}{RT_{rxn}} \qquad F_{EtOH-0} = \frac{P_{EtOH} Q_{amb}}{RT_{amb}}$$

Next, the apparent the reaction rate $\mathcal{R}$, the mean free path of BD λ_m and the Knudsen number Kn_d are calculated:

$$\mathcal{R} = \frac{F_{EtOH-0} X_{EtOH}}{V_{bed}} \qquad Kn_d = \frac{\lambda_m}{d} \qquad \lambda_m = \frac{k_B T_{rxn}}{\sqrt{2}\pi d_{BD}^2 P_{atm}}$$

Apart from the Knudsen number, the Knudsen diffusivity D_{BD}, the void fraction of the catalyst particle ε_p (a larger size of catalyst particle of 500 nm was considered to investigate the least favorable scenario), the tortuosity factor τ and the effective diffusivity of BD (the largest molecule in our system) D_{eff} can also be determined from the properties of our materials and molecules involved:

$$\varepsilon_p = \frac{V_p}{V_p + \frac{1}{\rho_s}} \quad \tau \sqrt{\frac{3 - \varepsilon_p}{2}} \quad D_{BD} = \frac{d_p}{3} \sqrt{\frac{8RT_{rxn}}{\pi MW_{BD}}} \quad D_{eff} = \frac{\varepsilon_p}{\tau} D_{EtOH}$$

Finally, the Weisz-Prater number is expressed through the following equation, comparing the reaction rate and the diffusion rate:

$$N_{W-P} = \frac{\mathcal{R} R_p^2}{C_{s-EtOH} D_{eff}}$$

Using this methodology allowed us to obtain a Weisz-Prater (W-P) number of 5.30 10^{-6}. As this number is much lower than 1, we can conclude that the reaction rate is not limited by internal diffusion limitations. Furthermore, by considering smaller particles of 50 nm instead of 500 nm, as we have observed in STEM-EDS (Figure V.6), the W-P number further decreases to 5.30 10^{-8}, confirming the absence of internal diffusion limitations in smaller catalyst particles. Interestingly, the decrease of pore diameters to 1 nm still adds up to a low W-P number of 3.65 10^{-5}. To conclude, the AASG process gave rise to catalyst particles with no external or internal diffusion limitations, even when considering large microspheres and small mesopores.

Table V.5: Experimental parameters used in the calculus of the Weisz-Prater number.

Parameter	Abbreviation	Value
Ambient temperature	T_{amb}	298.15 K
Ethanol partial pressure	P_{EtOH}	5132 Pa
Reaction temperature	T_{rxn}	598.15 K
Volumetric total flow	Q_{amb}	$6.3\ 10^{-7}$ m^3 s^{-1}
Pore diameter	d	$6.9\ 10^{-9}$ m
1,3-butadiene diameter	d_{BD}	$4.0\ 10^{-10}$ m
Boltzmann constant	k_B	$1.38\ 10^{-23}$ m^2 kg s^{-1} K^{-1}
Ethanol conversion	X_{EtOH}	52.8 %
Catalytic bed volume	V_{bed}	$1.1\ 10^{-7}$ m^3
Pore volume	V_p	$4.8\ 10^{-4}$ m^3 kg^{-1}
Catalytic bed density	ρ_s	858 kg m^{-3}
1,3-butadiene molecular weight	MW_{BD}	0.05409 kg mol^{-1}
Catalyst particle radius	R_p	$5.0\ 10^{-7}$ m

5.3.4 Studying operational parameters on catalytic performance

After improving the catalysts composition in order to maximize BD production, we can leverage on the different parameters used in the catalytic reaction. Here, we study the influence of the reaction temperature and the pre-reduction temperature. Also, reasoning that our catalysts encounter fast deactivation during the reaction owed to a blockage of the acid sites, we explore the effect of co-feeding hydrogen or oxygen in the system.

- Influence of reaction temperature

Figure V.10 shows the overall ethanol conversion and the products distribution at different reaction temperature during separate catalytic runs, with the best catalyst selected from the screening above (4Cu4Ta-SiO_2). A clear optimum in ethanol conversion and BD selectivity is reached at 350 °C, justifying the highest BD productivity of 0.25 g_{BD} g_{cat}^{-1} h^{-1} (Table V.6). For acetaldehyde, the selectivity decreases as the reaction temperature increases. In parallel, the selectivity in ethylene steadily increases with temperature. This trend is consistent with the literature and clearly proves the importance of a correct balance between redox and acid sites. At lower temperature, the formation of acetaldehyde will be favoured but due to a lack of condensation and dehydration power, the formation of BD remains limited. At temperature above 350 °C, the dehydration power of the catalyst overwhelms the redox power, thus favouring the direct dehydration of ethanol to ethylene. Ethylene formation decreases the selectivity in acetaldehyde and thus hinders the BD production. With the selected catalysts, at 350 °C, a correct compromise between those sites is achieved: the redox capabilities allow for an efficient acetaldehyde production and the acid sites enable the condensation of acetaldehyde and the subsequent dehydrations while maintaining the rate of the direct dehydration to ethylene low.

Table V.6: Catalytic performance and BD productivity in function of the reaction temperature for 4Cu4Ta-SiO_2. TOS=4 h.

Reaction Temperature	X_{EtOH} (%)	S_{BD} (%)	S_{AA} (%)	S_{EY} (%)	Y_{BD} (%)	P_{BD} (g_{BD} g_{cat}^{-1} h^{-1})
300 °C	68.6	34.0	55.4	5.4	23.3	0.15
325 °C	62.1	38.8	47.9	10.2	24.1	0.16
350 °C	76.0	50.0	29.6	16.3	38.0	0.25
375 °C	77.5	41.8	25.4	29.7	32.4	0.21
400 °C	85.1	39.1	17.6	40.6	33.3	0.22

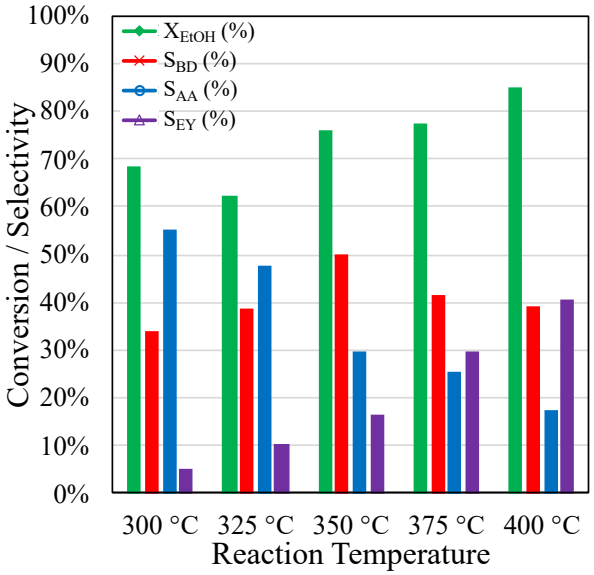

Figure V.10: Influence of the reaction temperature on the catalytic performance of 4Cu4Ta-SiO_2. Reaction conditions: Pre-reduction T°=350 °C, WHSV=1.1 h^{-1}, time-on-stream=4 hours.

Another important factor in any catalytic system is the stability, and this is obviously also influenced by reaction temperature. Data presented in Figure V.10 (and in other Tables and Figures of this work) are obtained as the average of 4 hours. Such representation suffers from important limitations because it hides the fact that these catalytic systems are in fact not stable in time. Thus, Figure V.11 shows the catalytic performance (ethanol conversion and selectivity for the major products) during time on stream at different reaction temperatures for separate catalytic runs (each one using fresh catalyst). For all reaction temperatures, the overall ethanol conversion tends to decrease with time, although the trend became more marked at high temperature. The BD selectivity is relatively stable at 300 °C but fell fast above this temperature, almost perfectly parallel with the ethanol conversion. Interestingly, the acetaldehyde and ethylene selectivities increased with time on stream. This points to a deactivation of the active sites responsible for the aldol condensation, causing the progressive accumulation of acetaldehyde. As this accumulation is gradual, we can hypothesize that some form of coke deposited on the active acid sites during reaction. This hypothesis is further corroborated by XPS analysis on the spent catalyst that was tested at 325 °C. The Si/C ratio was at 6.1 for the fresh catalyst and dropped to 3.0 for the spent sample, indicating a higher concentration of C on the catalysts surface. We can also expect this ratio to further decrease with the reaction temperature as

coke formation is more likely at higher temperatures, explaining the faster decrease in BD selectivity observed for the catalytic runs at 375 °C and 400 °C.

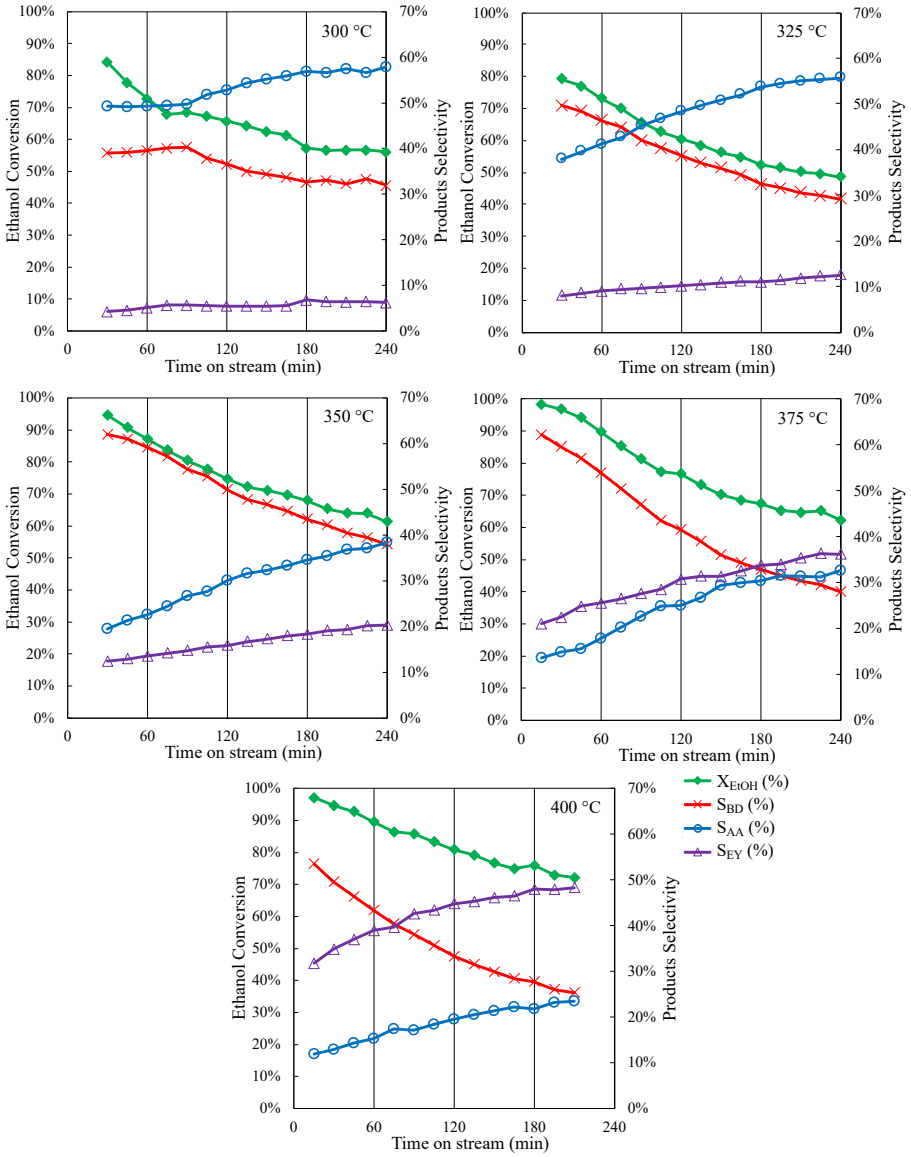

Figure V.11: Evolution of ethanol conversion and main products selectivities over time at different reaction temperatures for 4Cu4Ta-SiO_2.

- Influence of pre-reduction temperature

For the first step of the ETB reaction, e.a. the non-oxidative dehydrogenation of acetaldehyde, nanoparticles in the metallic state are needed.[220,221] For this, it is common practice to apply a pre-reduction of the catalyst (here, under a flow of 30 vol % of H_2 in N_2) to ensure the presence of metallic copper. However, to the best of our knowledge, the literature does not describe the influence of this pre-reduction temperature on the catalytic performance. Here, different pre-reduction temperatures were tested while keeping the reaction temperature constant at 325 °C (Figure V.12). In general, as the pre-reduction temperature increases, the BD selectivity decreases and the AA selectivity increases. Even though the highest ethanol conversion is reached at a pre-reduction temperature of 250 °C, the best BD selectivity is achieved at a pre-reduction temperature of 200 °C. Consequently, the best BD yield (41 %) and BD productivity (0.26 g_{BD} g_{cat}^{-1} h^{-1}) is obtained at the lowest pre-reduction temperature tested (Table V.7).

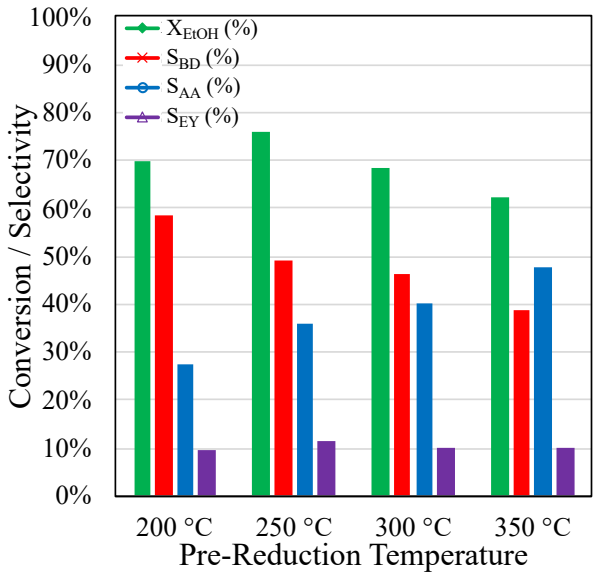

Figure V.12: Influence of pre-reduction temperature on the catalytic performance of 4Cu4Ta-SiO_2. Reaction conditions: Reaction temperature T°=325 °C, WHSV=1.1 h^{-1}.

Table V.7: Catalytic performance and BD productivity in function of the pre-reduction temperature for 4Cu4Ta-SiO_2. Reaction conditions: Reaction temperature T°=325 °C, WHSV=1.1 h^{-1}, TOS=4 h.

Pre-reduction Temperature	X_{EtOH} (%)	S_{BD} (%)	S_{AA} (%)	S_{EY} (%)	Y_{BD} (%)	P_{BD} (g_{BD} g_{cat}^{-1} h^{-1})
200 °C	69.7	58.6	27.5	9.6	40.8	0.26
250 °C	75.9	49.1	36.0	11.3	37.3	0.24
300 °C	68.3	46.3	40.2	10.1	31.6	0.20
350 °C	62.1	38.8	47.9	10.2	24.1	0.16

In terms of stability, a similar trend is observed for all pre-reduction temperatures (Figure V.13). The ethanol conversion starts at around 90 % and drops to ca. 50 % after 4 hours on stream for all tested pre-reduction temperatures. BD selectivity follows the same behaviour. However, the higher the pre-reduction temperature, the lower the average BD selectivity. Inversely, the AA selectivity increases with the pre-reduction temperature. Both observations point to an effect of the Cu oxidation state on the aldol condensation step or an influence of the pre-reduction on the Ta sites.

Only few studies have described the effect of the pre-reduction on the state of copper; no difference was observed between a catalyst pre-reduced at 325 °C and a catalyst directly exposed to ethanol.[127] In both cases, copper reached its reduced state in less than 1 hour and kept it during the following 3 hours of TOS.[127] Figure V.14a shows that a higher C/Ta ratio seems to be correlated to a higher BD productivity. As coke is supposedly depositing on active sites during the catalytic run, we should expect an opposite trend. But we can hypothesize that a higher condensation power of a catalyst can also lead to heavier carbonaceous species, as depicted in Figure I.4. For Cu, Figure V.14b and c show that the C/Cu ratio does not influence the BD productivity but the relative abundance of the different oxidation states of Cu can. Indeed, as the pre-reduction temperature of the catalyst decreases, the Cu(0)/Cu ratio increases and the Cu(I)/Cu decreases, leading to an improved BD productivity. This leads to consider that different copper oxidation states play different roles in the reaction mechanism of the reaction, potentially Cu(I) being active in the aldol condensation. Finally, TGA analysis in Figure V.14d displays a larger mass loss before 200 °C for the catalyst pre-reduced at 200 °C compared to the same catalyst pre-reduced at 350 °C (-8.2% and -5.7 % respectively, Figure IX.1 and 2), attributed to the loss of H_2O. TGA analysis also confirms that the sample pre-reduced at 200 °C contains more carbonaceous species than the catalyst pre-reduced at 350 °C as the mass loss around 300 °C is more pronounced (-9.1 % versus -5.5 %). However, the mass spectrometry analysis of the release of CO_2 (Figure IX.1 and 2) indicates that heavier coking species were present on the surface on the catalyst pre-

reduced at 200 °C, since the two CO_2 peaks are shifted to lower temperatures compared to the sample pre-reduced at 350 °C.

Although TGA data corroborates XPS analysis on spent catalysts, no clear trend is observed to justify the catalytic superiority of the catalyst pre-reduced at 200 °C. In the current state of our understanding, we can hypothesize that the different species of Cu may affect more than expected the aldol condensation rate and thus the BD productivity.

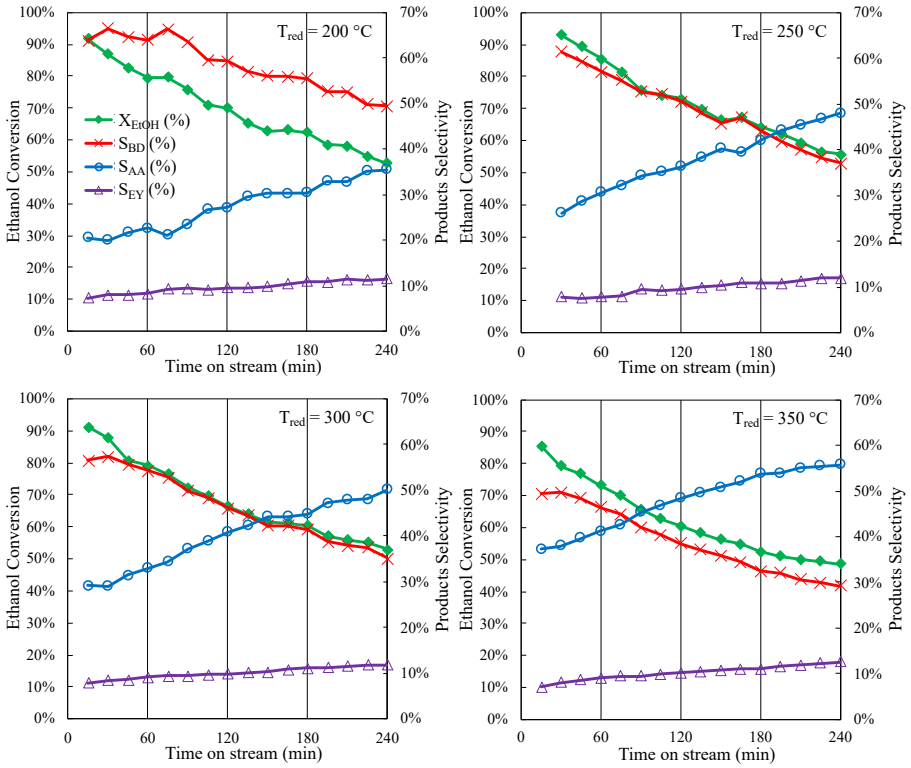

Figure V.13: Evolution of ethanol conversion and main products selectivities over time at different pre-reduction temperatures for 4Cu4Ta-SiO_2. Reaction conditions: T=325 °C, WHSV=1.1 h^{-1}.

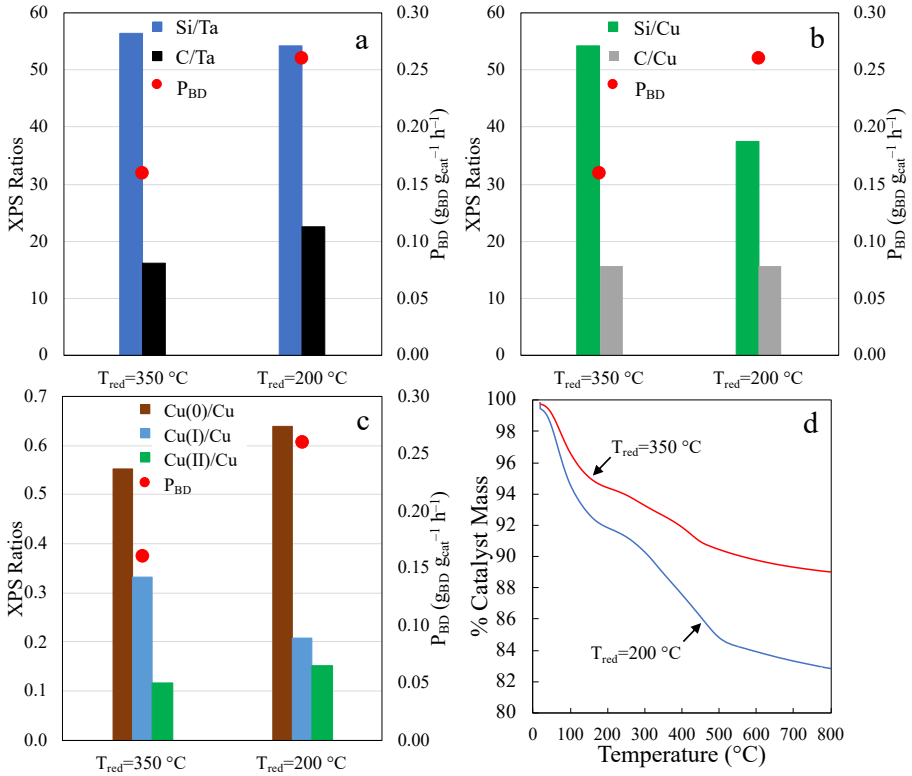

Figure V.14: Relationship between XPS molecular ratios and BD productivity (a, b, c); TGA analysis (d) on spent catalysts treated with different pre-reduction temperatures.

- Influence of co-feeding

With the idea to address the rapid deactivation of the catalyst for the first 4 hours of the catalytic run, different procedures of co-feeding gases were tested without a pre-reduction procedure. The co-feeding of a small partial pressure of hydrogen (<5 vol %) in the reaction stream was thought to potentially help maintain copper in a fully reduced state, helping the continuous production of acetaldehyde. However, Table V.8 and Figure V.15 show that the co-feeding of hydrogen with 2 or 5 molar percent does not improve the catalytic performance compared to a pre-reduction of the catalyst at 200 °C. These results indicate that the deactivation source in the ETB reaction is not related to a putative oxidation of the copper nanoparticles, especially since the catalytic test made without pre-reduction still yielded high amount of BD. Furthermore, Figure V.17a and b indicate no significant difference between molar ratios such as C/Ta or C/Cu. Even the ratio Cu(I)/Cu

seems identical between the two studied catalysts (Figure V.17c). Finally, the TGA profiles on Figure V.17d reflect similar mass losses at similar temperatures, further pointing to similar coking species being present on the catalysts surface, despite the different hydrogen concentrations co-fed to the catalysts during the catalytic run, indicating that the co-feeding of hydrogen does not improve the catalytic run, and even diminishes it.

To further investigate the source of deactivation, a small partial pressure of oxygen was also used as a co-feeding gas. A co-feeding of 0.5 mol.% of oxygen in the reaction stream yields near to no BD and the overall carbon balance is below 50 %, indicating that a significant fraction of ethanol and products were converted to CO_2. To avoid this issue, a lower molar percentage of O_2 was used. At 0.13 mol.%, a visible increase in both ethanol conversion and BD selectivity is observed over the first 4 hours of the catalytic run (Table V.8 and Figure V.15). A remarkable BD productivity of 0.38 $g_{BD}\ g_{cat}^{-1}\ h^{-1}$ was achieved. Here, we surmise that the co-feeding of a low percentage of oxygen helped prevent coke formation on aldol condensation sites or directly burn it after its formation, resulting in a high catalytic performance.

Table V.8: Catalytic performance and BD productivity in function of pre-reduction and co-feeding for 4Cu4Ta-SiO_2. Reaction conditions: Reaction temperature T°=325 °C, WHSV=1.1 h^{-1}, No pre-reduction, TOS=4 h.

Co-feeding Condition	X_{EtOH} (%)	S_{BD} (%)	S_{AA} (%)	S_{EY} (%)	Y_{BD} (%)	P_{BD} ($g_{BD}\ g_{cat}^{-1}\ h^{-1}$)
No Pre-reduction	65.0	43.0	40.6	12.1	28.0	0.18
Pre-reduction 200 °C	69.7	58.6	27.5	9.6	40.8	0.26
Co-feed H_2 2 %	63.5	47.3	37.6	10.9	30.0	0.19
Co-feed H_2 5 %	70.5	44.2	35.1	9.9	31.2	0.20
Co-feed O_2 0.13 %	91.3	64.0	28.7	4.5	58.4	0.38
Co-feed O_2 0.5 %	96.6	1.8	24.3	2.7	1.7	0.01

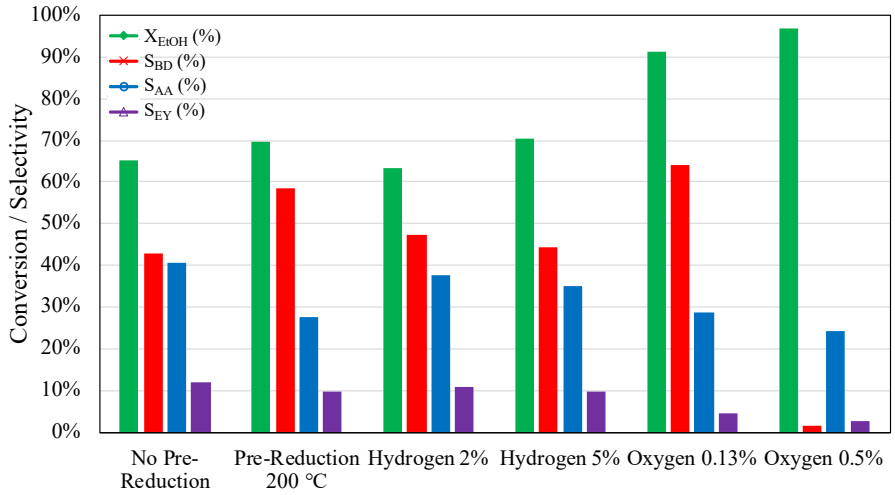

Figure V.15: Influence of pre-reduction and co-feeding on the catalytic performance of 4Cu4Ta-SiO_2. Reaction conditions: Reaction temperature T°=325 °C, WHSV=1.1 h^{-1}, No pre-reduction (unless stated otherwise).

Stability on stream is shown in Figure V.16 for the conditions discussed above (no pre-reduction, pre-reduction at 200 °C, with and without co-feed). This sheds light on the major stability advantage brought by co-feeding a low amount of oxygen. Even after 4 hours of time-on-stream, the BD yield sits at 48 %. Whereas all other catalysts showed rapid decrease in ethanol conversion, the co-feeding of oxygen maintains it around 90 %. Such activity can be explained by the constant coke removal from the catalysts surface by oxygen, keeping both type of catalytic sites active throughout the first 4 hours of the test.

A stability test over 24 hours was conducted in similar conditions (Figure V.18). Remarkably, the overall ethanol conversion stayed above 85 % for the whole test. Concomitantly, BD selectivity remained as high as 40% after 24h hours on stream. Over the course of this 24h test, the BD slowly decreased, while the AA selectivity increased, following a similar pattern to all other studied reaction conditions (yet much slower). Further adjustment of the percentage of oxygen in the feed might further optimize the stability in BD selectivity.

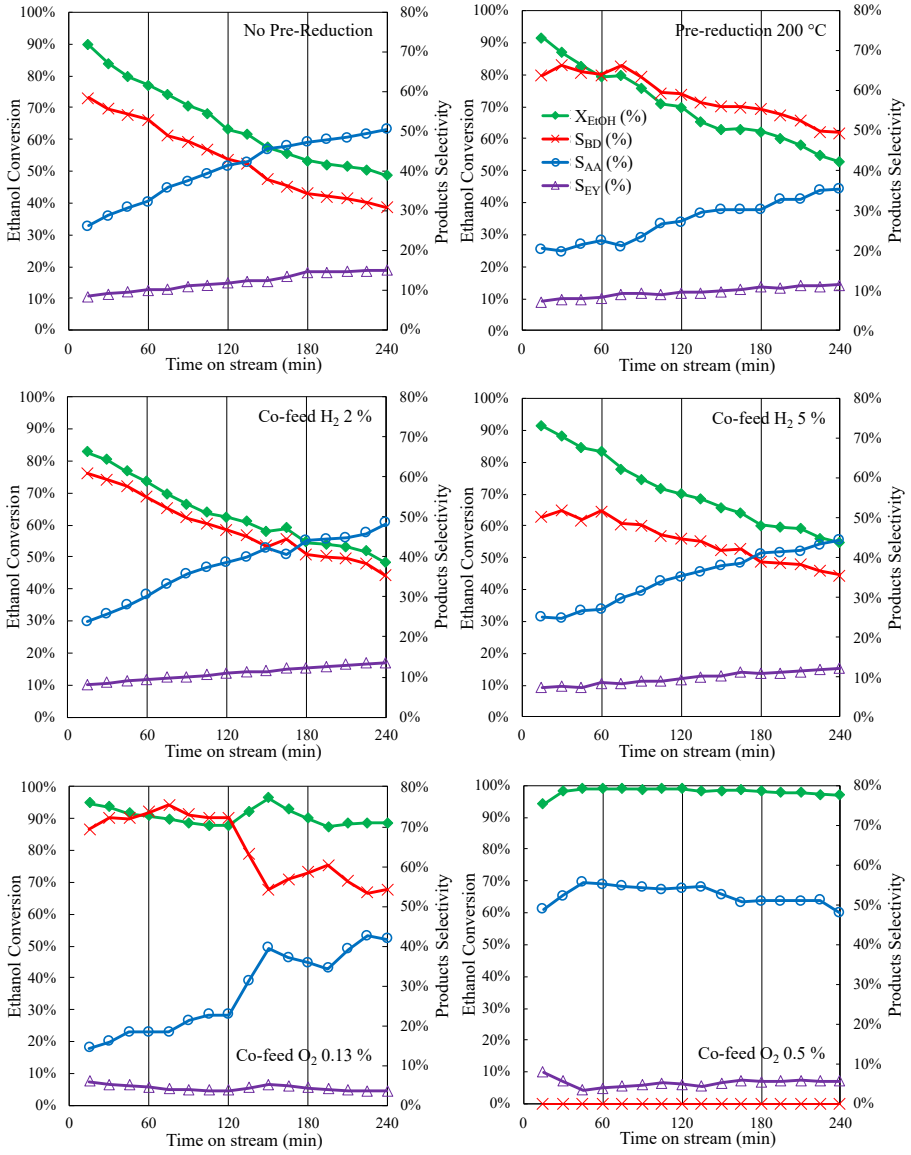

Figure V.16: Evolution of ethanol conversion and main products selectivities over time in different co-feeding conditions for 4Cu4Ta-SiO_2.

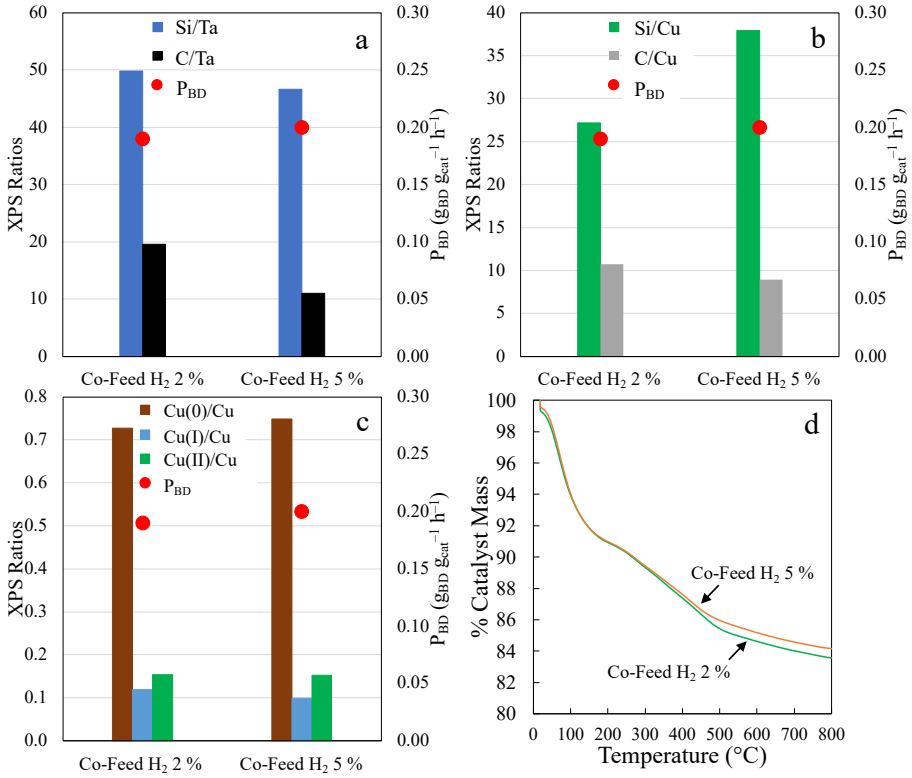

Figure V.17: Relationship between XPS molecular ratios and BD productivity (a, b, c); TGA analysis (d) on spent catalysts co-fed with different hydrogen percentages.

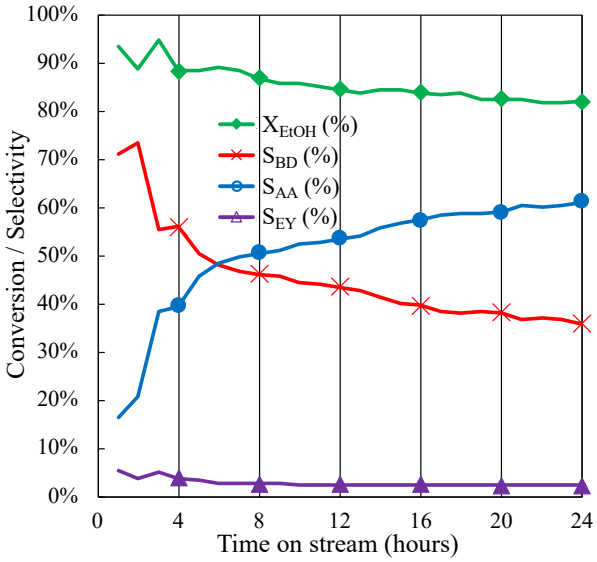

Figure V.18: Stability test of 4Cu4Ta-SiO_2 for 24 hours. Reaction conditions: T°=325 °C, Co-feed oxygen 0.13 %.

5.4 Conclusion

The aerosol-assisted sol-gel process was successfully applied to the synthesis of bifunctional Ta-Cu-based catalysts. We showed that our materials possessed open mesoporous texture with high specific surface areas and high pore volumes, ensuring facile mass transfer. Through different characterisation techniques, Ta was shown to be inserted in the silica matrix, in a dispersed form, and Cu was shown to form relatively small CuO nanoparticles (<20 nm). These two elements provided suitable acid and redox sites respectively for the direct conversion of ethanol to butadiene. Studying the influence of Ta and Cu loadings on catalyst properties and performance allowed us to design an optimized formulation with Ta and Cu loadings of 4 wt.% each. This catalyst was used to investigate different operating parameters. It was found that ethanol conversion and butadiene selectivity were highly dependent on the reaction temperature, on the pre-reduction temperature and on the presence of a co-fed gas. Applying the pre-treatment at 200 °C, setting the reaction temperature at 350 °C, and co-feeding a small partial pressure of oxygen, the best Ta-Cu catalyst reached a remarkable butadiene productivity of 0.38 $g_{BD}\ g_{cat}^{-1}\ h^{-1}$ with impressive stability.

Answering back to the questions stated in the objectives, we once again showed the importance of proximity and dispersion of the redox and acidic sites in our bifunctional catalyst, leading to a significant decrease in by-products (question (ii)). Studying operational parameters hinted at coking as the source of deactivation. It was further confirmed as the co-feeding of oxygen stabilized the catalysts performance, reaching new highs in BD selectivity and yield over 24 hours (question (iii)).

5.5 Appendix

Table V.9: List of ions used in ToF-SIMS.

Ion	m/z
Ta^+	180.9460
$TaOH^+$	197.9641
TaH_2O^+	198.9662
$TaOSi^+$	224.9265
$TaSiO_2^+$	240.9381
Ta^{2+}	361.8785
Ta_2OH^+	378.9091
Ta^{3+}	542.8896
Ta^-	180.9533
$TaOSi^-$	224.9195
TaO_3H^-	229.9410
TaO_4H^-	245.9378
$TaSiO_4^-$	272.9035
$TaSiO_5^-$	288.9015

CHAPTER 6: Non-hydrolytic sol-gel routes to bifunctional Cu–Ta catalysts

The results presented in this Chapter are published in:

Non-hydrolytic sol-gel routes to bifunctional Cu-Ta-SiO_2 catalysts for the upgrading of ethanol to butadiene, Denis D. Dochain, Ales Styskalik, Vit Vykoukal, Alexandre Vimont, Arnaud Travert, Damien P. Debecker, **Chemistry of Materials**, 35 (2023) 7113–7124

6.1 Abstract

Here, we leverage non-hydrolytic sol-gel (NHSG) chemistry to prepare tailored Cu-Ta-SiO_2 catalysts featuring open texture, dispersed acidic Ta sites and small Cu nanoparticles. In the ether route, silicon tetrachloride and tantalum pentachloride undergo polycondensation reactions with diisopropyl ether as the oxygen donor. In the acetamide elimination route, silicon tetraacetate reacts with pentakis(dimethylamido)tantalum(V). In both routes, copper(II) acetylacetonate is added and trapped in a tantalosilicate matrix. Upon calcination, CuO nanoparticles form and the resulting bifunctional materials develop a mesoporous texture with specific surface areas in the 650-950 $m^2\ g^{-1}$ range, pore volumes between 0.75 and 0.90 $cm^3\ g^{-1}$, and average pore diameters above 3 nm. With the help of NH_3-TPD, FTIR, CO- and pyridine-adsorbed FTIR, XRD, XPS and STEM-EDS, we demonstrate that the catalysts made via the acetamide elimination route show higher performance in the ethanol to butadiene reaction, with low selectivity in dehydration by-products, owing to moderate Lewis acidity, smaller Cu nanoparticles, and higher active sites proximity. After optimization of the Ta and Cu loadings, a butadiene productivity as high as 0.38 $g_{BD}\ g_{cat}^{-1}\ h^{-1}$ is obtained, surpassing state-of-the-art catalysts with similar formulations and tested in similar reaction conditions.

6.2 Introduction

Using the teachings of the previous chapter, we know that Cu-Ta-based formulations have a good prospect for the ETB reaction. We also know that we need a highly homogeneous catalyst with advantageous texture and good control on active sites speciation. In this context, NHSG is identified as an appealing preparation route. Indeed, “kinetic levelling” is commonly observed in NHSG, resulting in the formation of mixed oxide materials that exhibit exceptional homogeneity. Furthermore, the use of organic solvents with low surface tensions mitigates the risks of pore collapse during drying, yielding materials with great textures.

The present study compares the use of two distinct non-hydrolytic sol-gel synthesis routes – the ether route (Eq. 1) and the acetamide elimination route (Eq. 2). The final goal is to understand catalysts behaviour in order to obtain in a one-step fashion bifunctional Cu-Ta-SiO_2 catalysts showing high activity in the ETB reaction. The ether route, also called the alkyl halide elimination route, is a well-known recipe that combines metal chlorides and in

situ formed metal alkoxides to create M–O–M bonds (in this work, Si–O–Ta and Si–O–Si bonds).[176,180,222] On the other hand, the acetamide elimination route is an emerging method that involves the reaction between acetoxysilanes and metal amides to yield M–O–M bonds and release dialkylacetamide as volatile organic products.[177,179,188,223] Here, it is used to prepare a Ta-SiO_2 material via the reaction of silicon tetraacetate and pentakis(dimethylamido)tantalum(V).

$$\equiv M–Cl + R–O–M\equiv \rightarrow \equiv M–O–M\equiv + RCl \quad \text{(Eq. 1)}$$

$$\equiv M\text{-}NR_2 + \equiv M\text{-}OC(O)R' \rightarrow \equiv M\text{-}O\text{-}M\equiv + R'C(O)NR_2 \quad \text{(Eq. 2)}$$

By promoting the formulations with the addition of copper(II) acetylacetonate, we obtained bifunctional Cu-Ta-SiO_2 catalysts. The acetamide elimination route is shown to provide more active catalysts, owing to a better Cu dispersion and to a moderate Lewis acidity. We show that the formulation can be further optimized in terms of balance between Cu and Ta loadings, leading to boost catalytic performance and surpass similar state-of-the-art catalysts in similar catalytic conditions.[107,139]

6.3 Results

6.3.1 Ether route vs Acetamide route

We start by comparing the properties and performance of two bifunctional catalysts synthesized either by the ether route (Et-2Ta2Cu) or the acetamide elimination route (Ac-2Ta2Cu).

N_2-physisorption measurements (Figure VI.1a) show type IV isotherms with the presence of a hysteresis loop for both catalysts. Following IUPAC classification of hysteresis loops, Ac-2Ta2Cu follows a H2 loop, corresponding to ordered mesoporous materials. For Et-2Ta2Cu, we observe a H3 loop, characterizing aggregates of plate-like particles giving rise to slit-shaped pores.[224] It is noted that Ac-2Ta2Cu requires the use of a templating agent, here Pluronic F127. The addition of Pluronic F127 yields cylindrical mesopores, as already described in previous studies, while the non-templated acetamide route (not shown) is known to yield materials with predominantly microporous texture.[7,225,226] The ether route, on the other hand is known to lead to highly porous siliceous materials, even without templating agents. In fact, a widely open mesoporous is created simply by the trapping of the solvent during the slow inorganic polycondensation process.[190,227] Here, Et-2Ta2Cu is natively highly porous, with a broad pore size distribution in the mesopore

range. Both samples reach high specific surface areas (SSA): 640 $m^2 g^{-1}$ for Et-2Ta2Cu and 960 $m^2 g^{-1}$ for Ac-2Ta2Cu. Pore volume is higher for the catalyst obtained via the ether pathway with 0.91 $cm^3 g^{-1}$ compared to 0.76 $cm^3 g^{-1}$ for its acetamide counterpart (Table VI.1). Considering average mesopore diameters, Et-2Ta2Cu has the upper hand again with 6.2 nm whereas Ac-2Ta2Cu sits at 5.9 nm. However, when considering BJH adsorption curves (Figure VI.1a), both routes have the highest adsorption volume around 15 nm, further confirming the mesoporous character of Et- and Ac-2Ta2Cu. This is a typical range for materials prepared with Pluronic F127 as the templating agent.[7,225] The increase in pore volume in the lowest pore diameter range for Ac-2Ta2Cu corresponds to a fraction of micropores and are consistent with previous reports, as the acetamide elimination route natively yields a microporous texture.[177,179] Furthermore, Table VI.1 corroborates this observation with a superior micropore volume of 0.23 $cm^3 g^{-1}$ for Ac-2Ta2Cu compared to 0.05 $cm^3 g^{-1}$ for Et-2Ta2Cu. Indeed, Overall, both non-hydrolytic synthesis routes yield catalysts with a predominantly mesoporous texture and high SSA.

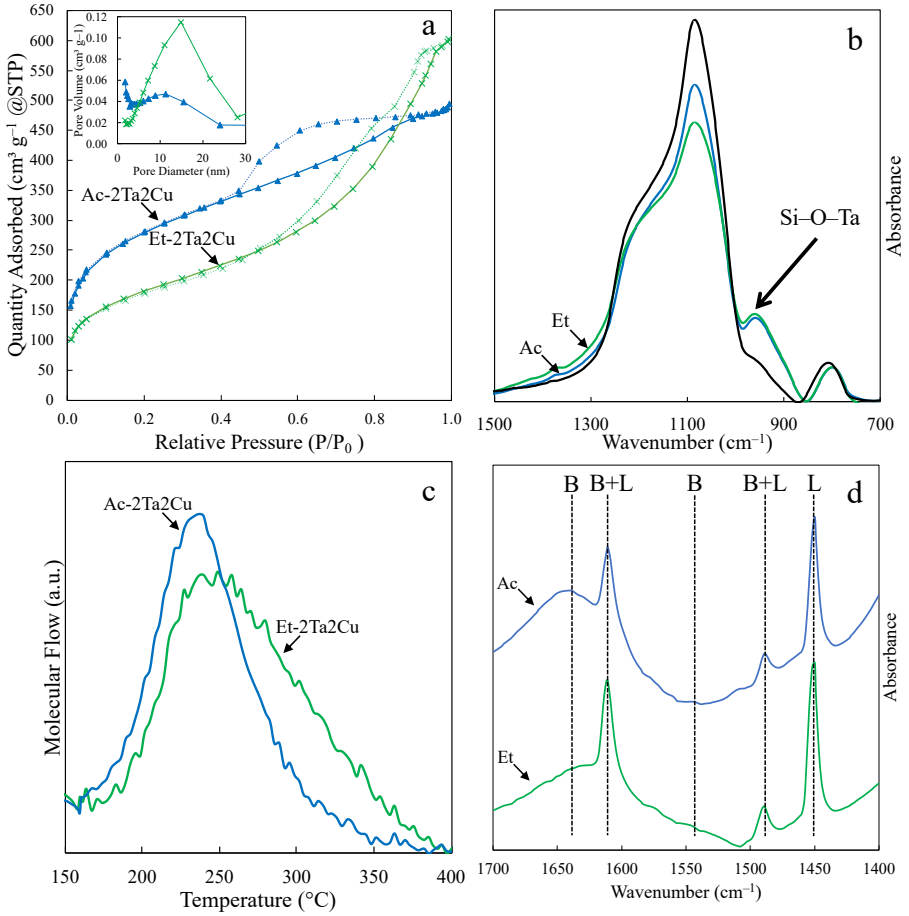

Figure VI.1: Comparison of Et-2Ta2Cu and Ac-2Ta2Cu on the basis of (a) N_2-physisorption isotherms and BJH pore size distribution profiles (inset) of Et-2Ta2Cu (green ×), Ac-2Ta2Cu (blue Δ) (adsorption isotherms are plotted as solid lines, desorption isotherms are plotted as dotted lines) ; (b) FTIR Spectra of SiO_2 (black), Et-2Ta2Cu (top green) and Ac-2Ta2Cu (bottom blue). ; (c) NH_3-TPD of Et-2Ta2Cu (green) and Ac-2Ta2Cu (blue) ; (d) FTIR spectra after pyridine adsorption and evacuation at 150 °C of Et-2Ta2Cu (bottom green curve) and Ac-2Ta2Cu (top blue curve) (B= band corresponding to Bronsted acid sites ; L= band corresponding to Lewis acid sites).

Table VI.1: Textural properties (N_2-physisorption) and chemical composition comparing catalysts synthesized by ether route and acetamide elimination route.

Sample	S_{BET} ($m^2\ g^{-1}$)	V_p ($cm^3\ g^{-1}$)[a]	V_{meso} ($cm^3\ g^{-1}$)[b]	V_μ ($cm^3\ g^{-1}$)[c]	D_{meso} (nm)[d]	Ta wt %[e]	Cu wt %[e]
Et-2Ta2Cu	640	0.91	0.86	0.05	6.2	1.97	1.83
Ac-2Ta2Cu	960	0.76	0.53	0.23	5.9	1.65	2.60

[a] Pore volume at P/P_0=0.98; [b] calculated as ((total pore volume) – (micropore volume)) [c] Calculated via t-plot; [d] calculated as $4V_{meso}/A_{meso}$; [e] Measured by ICP

ICP results confirm that both synthesis routes lead to Ta and Cu contents close to the nominal amounts (Table VI.1). Surface composition was measured by XPS. Si/Ta molar ratios were found comparable for Et-2Ta2Cu and Ac-2Ta2Cu, and close to the experimental values determined by ICP (Table VI.2). Therefore, Ta appears to be dispersed homogeneously throughout both catalysts similarly in the bulk and at the surface. On the contrary, Si/Cu ratios for both catalysts are markedly higher than the bulk values obtained by ICP, consistent with the formation of aggregated forms of copper (i.e. Cu nanoparticles, that are not necessarily on the particles surface). STEM-EDS (Figure VI.5c and d) indeed confirms the formation of aggregated copper in both catalysts, although more marked for Ac-2Ta2Cu. XRD also confirms the presence of those aggregates of copper nanoparticles (Figure VI.6). The lower Si/Cu ratio for Et-2Ta2Cu is a sign that Cu is more abundant on the surface of the catalyst made via the ether route. The relatively higher Si/Cu ratio for Ac-2Ta2Cu may be related to the interaction between the Cu precursor (copper acetylacetonate) and the Pluronic F127 that would concentrate Cu in the bulk of Ac-2Ta2Cu. Importantly, Figure VI.2 shows that the Ta $4f_{7/2}$ peak is slightly but significantly shifted from the position expected for Ta_2O_5 (26.9 eV), by + 0.2 eV for Et-2Ta2Cu and + 0.5 eV for Ac-2Ta2Cu.[228,229] This shift to higher binding energies indicates that Ta is not strictly in a Ta_2O_5 environment (Ta oxide crystals or amorphous polymeric or oligomeric surface species), and instead forms TaO_x species inserted into the silica matrix. Indeed, Si is more electronegative than Ta, resulting in lower electron density and thus higher electrons binding energies for Ta atoms forming multiple Ta–O–Si bonds instead of Ta–O–Ta bond. Interestingly, the shift is slightly more marked (by ~0.2 eV) in Ac-2Ta2Cu, which might indicate that Ta has a higher degree of dispersion and insertion in the silica matrix, as compared to Et-2Ta2Cu.

Table VI.2: Atomic ratios and acidic properties comparing ether and acetamide elimination route.

Sample	Bulk Si/Ta[a]	Bulk Si/Cu[a]	Si/Ta[b]	Si/Cu[b]	Total acidity (mmol g^{-1})[c]	Lewis acidity (µmol g^{-1})[d]
Et-2Ta2Cu	116	38	174	84	0.153	63.8
Ac-2Ta2Cu	139	23	191	115	0.122	42.0

[a] Measured by ICP ; [b] Measured by XPS, theoretical Si/Ta=151, theoretical Si/Cu=53; [c] Measured by NH_3-TPD ; [d] measured by FTIR spectroscopy coupled with pyridine adsorption, after degassing at 150 °C

FTIR analyses on the two catalysts (Figure VI.1b) gave very similar spectra, with the main absorption bands typically originating from the amorphous silica matrix.[206-210] The band at 750-850 cm^{-1} is attributed to the symmetric vibration of Si–O–Si bonds whereas the most intense absorption

band at 1050-1065 cm^{-1} is ascribed to the antisymmetric stretching vibration of Si–O–Si. Importantly, the distinct band at 950 cm^{-1} can be attributed to the Si–O–Ta stretching mode (even though a contribution of Si–OH vibration is possible too), since this band is not present in the pristine SiO_2 spectrum.[211,212,230] It suggests that tantalum was effectively incorporated into the silica in both catalysts.

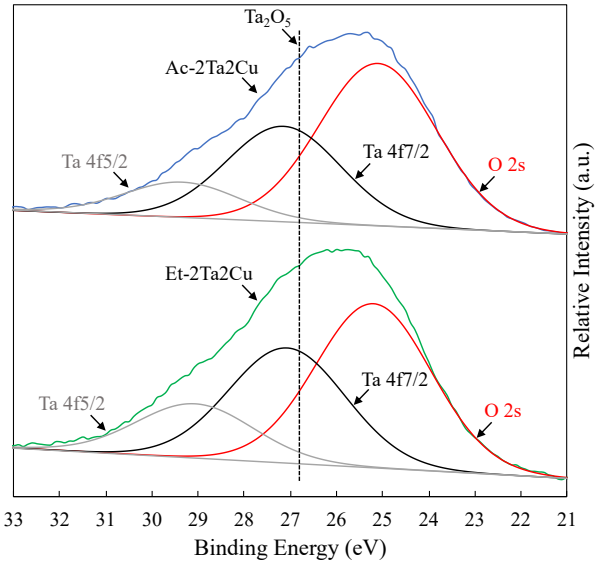

Figure VI.2: High resolution XPS spectra of the Ta 4f doublet observed on Ac-2Ta2Cu and Et-2Ta2Cu. The dotted line corresponds to the expected position of Ta 4f7/2 in bulk Ta_2O_5.

DRUV spectra depicted in Figure VI.3 provide further information on the chemical environment around the Ta atoms. A clear shoulder around 30,000 cm^{-1} is present for Et-2Ta2Cu but not for Ac-2Ta2Cu. Since the main intensity band around 40,000 cm^{-1} is attributed to Ta inserted in the silica matrix and the shoulder at 30,000 cm^{-1} is due to Ta in a higher coordination state,[230,231] we can state that some form of condensed Ta oxide is present in Et-2Ta2Cu, but not in Ac-2Ta2Cu. This result corroborates the XPS results showing a higher degree of dispersion/insertion in the catalyst made via the acetamide elimination route.

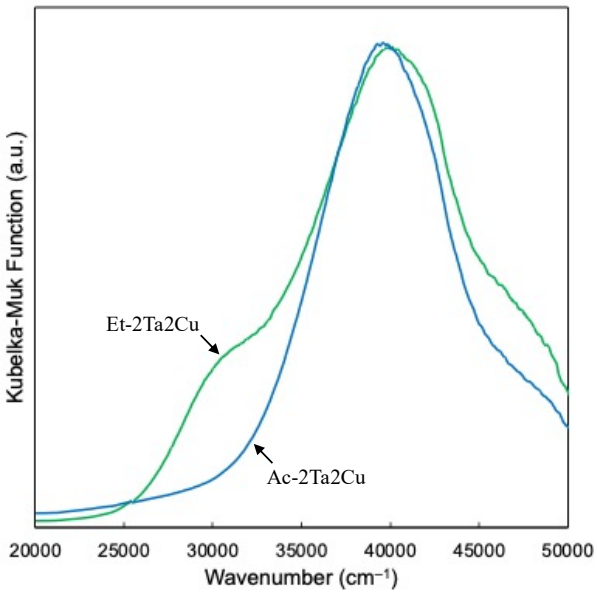

Figure VI.3: DRUV Spectra of Et-2Ta2Cu (top green curve) and Ac-2Ta2Cu (bottom blue curve).

FTIR measurements after CO adsorption can be used to corroborate NH_3-TPD and DRUV results (Figure VI.4). The band at 2156 cm^{-1} is attributed to CO adsorbed on silanol groups and that at 2138 cm^{-1} to physisorbed CO and both signals are of similar sizes for Ac- and Et-made catalysts. On Et-2Ta2Cu, CO adsorption leads to n(CO) vibration bands at 2200, 2191 and 2169 cm^{-1}, while the corresponding bands were virtually absent or found with a much lower intensity on Ac-2Ta2Cu. These bands were previously attributed to the coordination of CO on unsaturated transition metal oxide sites[148] (i.e. not Ta_2O_5 or mere TaO_x polymeric species), with different possible configurations inside the silica matrix, resulting in the formation of different types of acid sites.[232] Thus, the high-temperature shoulder in the NH_3-TPD peak (Figure VI.1c) and the 30000 cm^{-1} signal in DRUV spectra (Figure VI.3) of Et-2Ta2Cu can be related to the presence of those unsaturated Ta surface sites. Furthermore, the band at 2112 cm^{-1} is assigned to the adsorption of CO on Cu^{2+}.[233] Interestingly, its intensity is much higher for Ac, indicating again a higher amount of Cu^{2+} centers accessible to CO on this catalyst. This can be interpreted as a higher dispersion of Cu on Ac-2Ta2Cu, further confirming STEM-EDS results (Figure VI.5d).

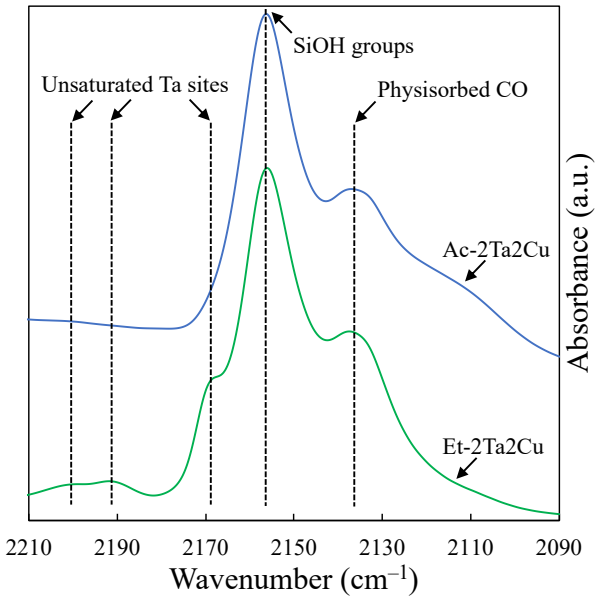

Figure VI.4: FTIR Spectra after CO adsorption at 77 K of Ac-2Ta2Cu (top blue curve) and Et-2Ta2Cu (bottom green curve).

STEM-EDS analysis shown in Figure VI.5 indicates an amorphous disorganised silica arrangement in both synthesis pathways. Et-2Ta2Cu features an uneven distribution of Cu, with the formation of large Cu aggregates appearing in the form of lighter spots of tens of nanometers, confirmed by the elemental mapping (Figure VI.5c). While Ta is present throughout the sample, some Ta accumulation is detected close to the Cu aggregates (Figure VI.5a). These Ta-rich zones are tentatively related to the condensed Ta oxide species suspected from DRUV results. On the contrary, Ac-2Ta2Cu images (Figure VI.5b and d) point towards a high dispersion of both Ta and Cu sites, with Ta (green) and Cu (red) scattered evenly throughout the sample. This is consistent with the apparent better degree of Ta insertion found for Ac-2Ta2Cu and the higher Cu dispersion shown by CO-FTIR. Interestingly, elemental mapping also suggests a higher proximity between the two active elements in this catalyst: where Ta is present, Cu is present in the immediate vicinity (Figure VI.5). On the contrary, in Et-2Ta2Cu one can detect zones where Ta is present, but Cu is not.

The total acidity, as measured by NH_3-TPD, is higher for Et-2Ta2Cu compared to Ac-2Ta2Cu (Table VI.2), which is consistent with the larger amounts of unsaturated Ta sites detected by CO. Additionally, since the ether route has yielded a material with lower SSA, the difference in the surface concentration of acid sites is even more pronounced, with 0.239 $\mu mol.m^{-2}$ for

Et versus 0.127 µmol m^{-2} for Ac. Ammonia desorption profiles (Figure VI.1c) also allow comparing the strength of these acid sites. For both catalysts, the main desorption peak sits at ~240 °C. However, Et-2Ta2Cu features a tail of NH_3 desorption at higher temperature (Figure VI.1c), indicating the presence of stronger acid sites in this catalyst, as compared to Ac-2Ta2Cu. FTIR coupled with pyridine and CO adsorption provides further description of the type of acid sites (Figure VI.1d and Figure VI.4). No FTIR band characteristic of pyridine adsorbed on Bronsted sites was identified. On the other hand, Lewis acidity is clearly detected and Et-2Ta2Cu was found to be significantly more Lewis acidic than Ac-2Ta2Cu (64 µmol g^{-1} vs. 42 µmol g^{-1} of Lewis acid sites respectively). Finally, CO-FTIR suggests that the stronger Lewis acidity evidenced by NH_3-TPD is mostly due to the two types of Ta coordinatively unsaturated sites characterized by the ν(CO) bands at 2191 and 2200 cm^{-1} (Figure VI.4) as such high wavenumbers are indicative of a relatively high polarizing power of the corresponding sites.

On the Cu dispersion, XRD patterns highlighted the presence of the CuO phase, with diffraction peaks at 2θ=35.5° and 38.6° for both samples (Figure VI.6). Applying the Scherrer equation on the peak at 2θ = 38.6 ° (111) the size of CuO crystallite was estimated at 18 nm for Et-2Ta2Cu, compared to 15 nm for Ac-2Ta2Cu, confirming higher CuO sizes observed in STEM-EDS for Et.

Overall, this characterization survey converges to affirm that Cu active site dispersion is lower in the catalyst prepared by the ether route. In Et-2Ta2Cu, part of the Ta is inserted in the silica network but another part forms independent Ta oxide species. Knowing that Ta_2O_5 tends to be more acidic than silica-dispersed TaO_x species,[234] we tentatively associate the presence of condensed Ta oxide species with the formation of higher and stronger Lewis acid sites (ν(CO) bands at 2191 and 2200 cm^{-1}). In this catalyst, Cu also forms relatively large crystallites, and accumulates in large aggregates. On the other hand, the catalyst formed by the acetamide elimination route (Ac-2Ta2Cu) features evenly dispersed Ta sites, which appear to be well dispersed and inserted in the silica matrix. This catalyst exhibits mild Lewis acid sites (ν(CO) band at 2169 cm^{-1}). Moreover, Cu is highly dispersed, forming small crystallites and no large aggregates. From this characterization study, it also emerges that the mixing and proximity between redox (Cu) and acid (TaO_x) sites is higher in Ac-2Ta2Cu.

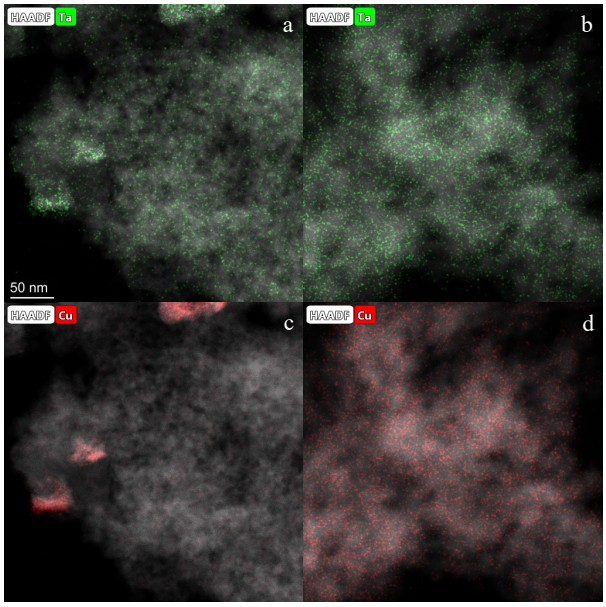

Figure VI.5: STEM-EDS with elemental mapping of (a) Ta atoms for Et-2Ta2Cu, (b) Ta atoms for Ac-2Ta2Cu, (c) Cu atoms for Et-2Ta2Cu and (d) Cu atoms for Ac-2Ta2Cu.

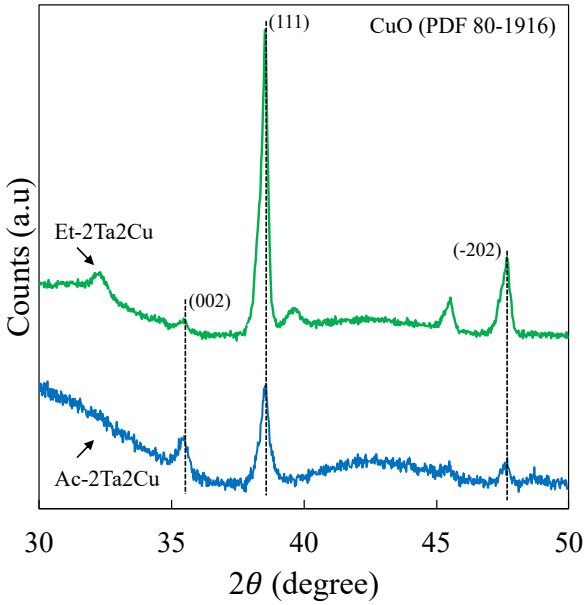

Figure VI.6: Diffractograms of Et-2Ta2Cu (top green curve) and Ac-2Ta2Cu (bottom blue curve).

Catalytic performance relative to the ethanol-to-butadiene reaction is summarized in Table VI.3. For Et-2Ta2Cu, the overall ethanol conversion reached 84 %, while Ac-2Ta2Cu Et 2Ta2Cu only 58 % conversion. Marked differences are noted in terms of selectivity, and overall BD yield. Clearly, Et-2Ta2Cu produces relatively modest amounts of acetaldehyde, but yields a lot of dehydration products (ethylene and diethylether). This appears consistent with the fact that this catalyst made via the ether route features relatively large Cu nanoparticles (lower dehydrogenation activity) and displays higher amount, density, and strength of Lewis acid sites (leading to intense dehydration activity). While Lewis acidic sites are needed to complete the reaction path that leads to BD, an excessive Lewis acidity coupled with lower active sites proximity appears to favour the direct dehydration of ethanol, leading to by-products which do not enter the targeted cascade of reaction. As a result, the BD yield is mediocre (12%).

On the contrary, Ac-2Ta2Cu shows a higher dehydrogenation activity and no production of by-products. As a result, even though the ethanol conversion is lower for Ac-2Ta2Cu, a high BD yield is obtained (29%). This can be correlated with the smaller Cu nanoparticles (which are then more active) and the moderate Lewis acidity (which avoid excessive dehydration activity). It is also possible that the higher proximity between both types of active sites favours a more rapid substrate channelling of reaction intermediates (in particular acetaldehyde) from the redox sites to the acid sites that are responsible for the completion of the ETB reaction, at the expense of side reactions.

In the light of the characterization studies presented above, the higher BD performance obtained with the catalyst prepared via the acetamide elimination route can be correlated with the higher degree of insertion of Ta sites in the silica matrix, forming Lewis acid sites of moderate strength, and to the formation of relatively small and highly dispersed Cu nanoparticles.

Table VI.3: Comparison of ether route and acetamide elimination route catalytic performance in the ETB reaction at 325 °C, WHSV=1.10 h–1 and TOS=3 hours.

Catalyst	Ethanol conversion (%)	Butadiene (%)		Acetaldehyde (%)		Ethylene (%)		Others[a] (%)	
		Yield	Sel	Yield	Sel	Yield	Sel	Yield	Sel
Et-2Ta2Cu	83.5	4.8	12.0	14.5	36.0	30.1	40.7	7.4	8.8
Ac-2Ta2Cu	58.2	29.2	50.2	26.3	45.3	<1%	<1%	<1%	<1%

[a] Other butenes, diethylether and propylene.

6.3.2 *Improving the formulation of catalysts synthesized via the acetamide elimination route*

With the successful acetamide elimination protocol in hand, we attempted to further optimize the formulation by adjusting the relative loading of Cu and Ta, in a search for higher catalytic performance. A total of 7 additional catalysts are studied. One series studies the influence of the Cu loading by fixing the Ta amount to 2 wt.%. The other series inspects the influence of Ta loading by fixing the Cu amount to 4 wt.% and varying the Ta loading from 1 to 4 wt.%.

The influence of the Cu loading on textural properties (Figure VI.7a and Table VI.4) is negligible. From 2 to 5 wt.% of Cu, catalysts remain mesoporous with SSA above 820 $m^2\ g^{-1}$, mesopore volumes higher than 0.50 $cm^3\ g^{-1}$ and average mesopore diameters around 4 nm. Pore size distribution (BJH on the adsorption isotherm) remains centered around 12 nm. Similarly, increasing the Ta loading from 1 to 4 wt.% does not influence the catalysts texture: SSA that stays in the 820-930 $m^2\ g^{-1}$ range with mesopore volumes around 0.60 $cm^3\ g^{-1}$ and average mesopore diameters of ca. 4 nm (Figure VI.7b). Pore size distribution curves are virtually unaffected.

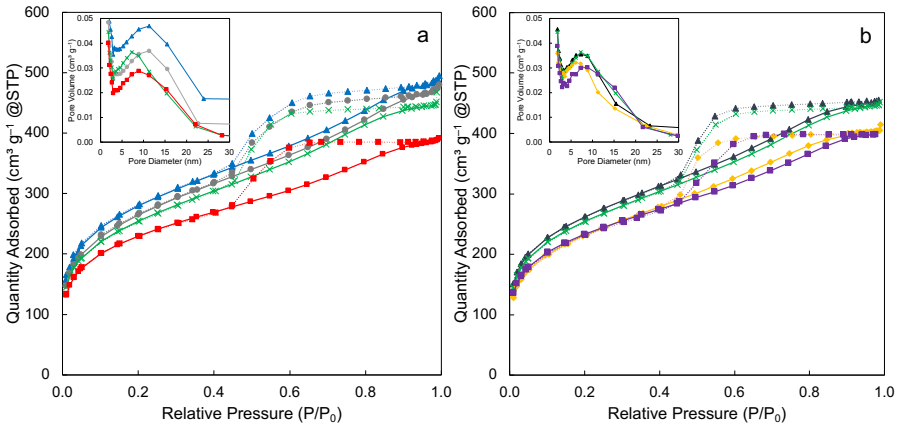

Figure VI.7: (a) N_2-physisorption isotherms and BJH adsorption curves of Ac-2Ta2Cu (blue triangle), Ac-2Ta3Cu (grey circle), Ac-2Ta4Cu (green cross), Ac-2Ta5Cu (red square) ; (b) N_2-physisorption isotherms and BJH adsorption curves of Ac-1Ta4Cu (black triangle), Ac-2Ta4Cu (green cross), Ac-3Ta4Cu (yellow diamond), Ac-4Ta4Cu (purple square). Adsorption isotherms are plotted as solid lines, desorption isotherms are plotted as dotted lines.

Table VI.4: Influence of Cu loading and Ta loading on textural properties (N_2-physisorption).

Sample	S_{BET} (m^2 g^{-1})	V_{meso} (cm^3 g^{-1})[a]	D_{meso} (nm)[b]
Ac-2Ta2Cu	960	0.53	5.9
Ac-2Ta3Cu	940	0.63	3.6
Ac-2Ta4Cu	900	0.60	3.6
Ac-2Ta5Cu	820	0.50	3.5
Ac-1Ta4Cu	930	0.60	3.6
Ac-2Ta4Cu	900	0.60	3.6
Ac-3Ta4Cu	820	0.54	3.5
Ac-4Ta4Cu	830	0.58	4.2

[a] calculated as ((total pore volume) – (micropore volume)) ; [b] calculated as $4V_{meso}/A_{meso}$

All Si/Ta ratios obtained by XPS for samples with varying Cu loadings (Ac-2TaXCu) are similar and hedges towards the fact that Ta dispersion and repartition between the surface and the bulk of the material is unaffected by the presence of copper (Table VI.5). Naturally, as the Ta loading increases, the corresponding Si/Ta ratio decreases. Si/Cu ratios logically decrease as the Cu loading rises. Interestingly, when varying the Ta content, the Si/Cu tends to stay in the same range. Overall, XPS data demonstrate no major influence of one element on the spatial distribution of the other.

Table VI.5: XPS ratios Si/Ta and Si/Cu for acetamide catalysts and CuO crystallite sizes with various Ta and Cu loadings.

Sample	Si/Ta[a]	Si/Cu[a]	CuO Crystallite size (nm)
Cu screening			
Ac-2Ta2Cu	191	123	15
Ac-2Ta3Cu	212	61	15
Ac-2Ta4Cu	231	81	15
Ac-2Ta5Cu	189	42	17
Ta screening			
Ac-1Ta4Cu	496	103	15
Ac-2Ta4Cu	231	122	15
Ac-3Ta4Cu	165	95	18
Ac-4Ta4Cu	119	84	18

[a] Calculated by XPS

In FTIR, no influence of Cu on the absorbance band at 950 cm^{-1}, corresponding to Si–O–Ta bonds, is noted (Figure VI.8a). This corroborates XPS results and the fact that Cu does not influence the insertion or dispersion of Ta atoms in the silica matrix. Furthermore, the intensity of the band clearly increases with the Ta loading (Figure VI.8b).

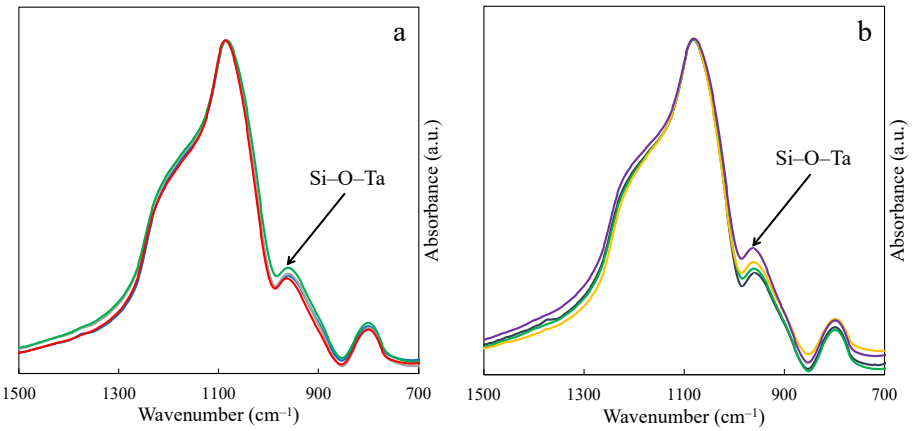

Figure VI.8: FTIR spectra of (a) Ac-2Ta2Cu (blue), Ac-2Ta3Cu (grey), Ac-2Ta4Cu (green), Ac-2Ta5Cu (red) ; (b) Ac-1Ta4Cu (black), Ac-2Ta4Cu (green), Ac-3Ta4Cu (yellow), Ac-4Ta4Cu (purple).

CuO crystallites are detected in XRD in the form of small and relatively broad peaks at 2θ=35.5° and 38.6° (Figure VI.9). Although differences in diffractions intensity can be noted, the width at half-height remains in the same range. Subsequently, even when increasing the Cu loading from 2 wt.% up to 5 wt.%, the CuO crystallite size estimated via the Scherrer equation (on the (111) diffraction peak at 38.5°) stay between 15 and 17 nm (Table VI.5). Finally, an increment in Ta loading appears to cause a decline in diffractions intensity but crystallite sizes are not significantly altered.

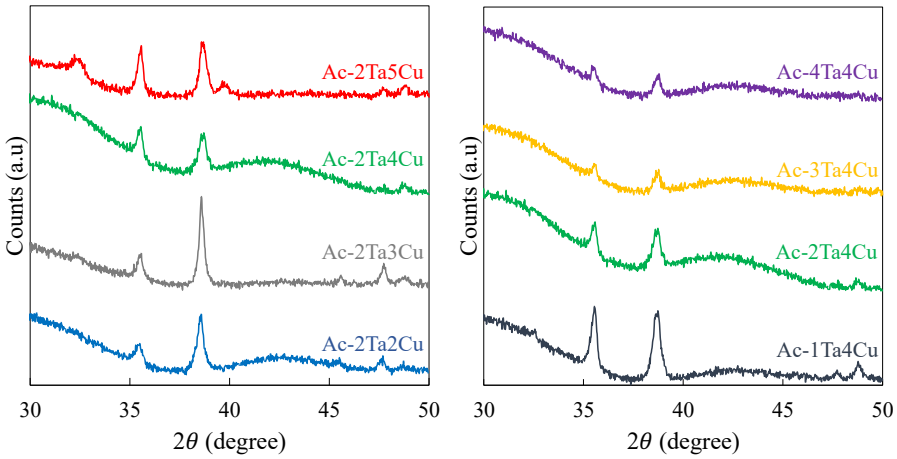

Figure VI.9: Diffractograms of catalysts with various Ta and Cu loadings.

Varying the Cu amount in the catalyst reveals an optimum in BD yield for Ac-2Ta4Cu (Table VI.6). Considering lower Cu loadings (2 and 3 wt.%), the ethanol conversion is lower, penalizing the overall BD yield. On the other side, Ac-2Ta5Cu has a high ethanol conversion but lower BD selectivity in favour of a higher acetaldehyde selectivity of 53 %. This demonstrates a relative default in acidic sites required to convert the acetaldehyde to BD (through cascading condensation, dehydration, and hydrogen transfer reactions). Thus, we considered increasing the Ta loading (Table VI.6, bottom part), and this led to a marked improvement in BD selectivity. Clearly, the decrease in acetaldehyde selectivity goes hand in hand with a boost in BD production, further confirming the importance of Ta in catalysing the acetaldehyde condensation step and the rest of the ETB reaction mechanism. In the end, a BD yield as high as 60% was achieved (ethanol conversion of 82 % and BD selectivity of 74%) with the Ac-4Ta4Cu catalyst (Table VI.6). This corresponds to a BD production yield of 0.39 $g_{BD}\ g_{cat}^{-1}\ h^{-1}$ at WHSV=1.1 h^{-1} which is higher than the productivity (0.25 $g_{BD}\ g_{cat}^{-1}\ h^{-1}$) reported for similar formulations prepared by coprecipitation or wet-kneading and tested at the same temperature and with the same space velocity.[107,139] Concomitantly, other by-products were kept below 10 % of yield. This illustrates the importance of correctly balancing the redox and acidic active sites in bifunctional catalysts, for they have work in a coordinated way to favour the correct reaction pathway and achieve high BD yield.

In terms of stability, Figure VI.10 represents the evolution of ethanol conversion and products selectivity for Ac-4Ta4Cu during the 3 hours of the catalytic run. First, the ethanol conversion steadily decreases from 93 % to 68 %. The same trend, although less pronounced, is observed for butadiene selectivity, with a slight decrease from 74 % to 65 %. Concomitantly, the acetaldehyde selectivity increases from 15 % to 28 %. Such trends can potentially be explained by the coke formation on the catalysts surface, more specifically on the active sites responsible for the aldol condensation. Coking thus prevents the condensation of acetaldehyde, progressively reducing the amount of produced butadiene and explaining the accumulation of acetaldehyde at the outlet of the reactor. Furthermore, the decrease in butadiene selectivity (ca. 10 %) corresponds to the increase in acetaldehyde selectivity (ca. 13 %), indicating that butadiene is formed directly from acetaldehyde and that none of the intermediate steps in the Toussaint-Kagan mechanism is limiting.

Table VI.6: Influence of Ta and Cu loadings on the catalytic performance in the ETB reaction at 325 °C, WHSV=1.10 h^{-1} and TOS=3 hours.

Catalyst	Ethanol conversion (%)	Butadiene (%)		Acetaldehyde (%)		Ethylene (%)		Others (%)	
		Yield	Sel	Yield	Sel	Yield	Sel	Yield	Sel
Cu screening									
Ac-2Ta2Cu	58.2	29.2	50.2	26.3	45.3	<1%	<1%	<1%	<1%
Ac-2Ta3Cu	57.2	29.8	52.1	24.5	42.8	<1%	<1%	<1%	<1%
Ac-2Ta4Cu	73.4	36.5	49.7	31.6	43.1	<1%	<1%	<1%	<1%
Ac-2Ta5Cu	75.3	31.4	41.7	40.2	53.4	<1%	<1%	<1%	<1%
Ta screening									
Ac-1Ta4Cu	67.0	26.2	39.1	31.2	46.5	1.4	2.1	8.2	12.3
Ac-2Ta4Cu	73.4	36.5	49.7	31.6	43.1	<1%	<1%	<1%	<1%
Ac-3Ta4Cu	77.6	54.9	70.7	15.5	20.0	3.0	3.9	4.2	5.5
Ac-4Ta4Cu	81.8	60.1	73.5	13.4	16.4	1.0	1.3	7.2	8.8

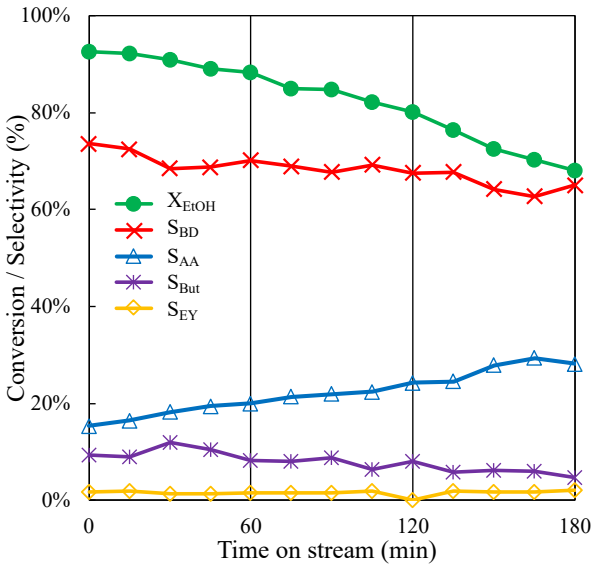

Figure VI.10: Stability of Ac-4Ta4Cu in the ETB reaction ; Reactions conditions: T=325 °C, WHSV=1.1h^{-1}.

6.4 Conclusion

NHSG synthesis routes such as the ether route and the acetamide elimination route were proven effective to obtain – in a one-pot fashion – mesoporous bifunctional Cu-Ta-SiO_2 catalysts featuring Ta species incorporated in the silica matrix and Cu nanoparticles below 20 nm. However, the ether route was shown to lead to imperfect Ta insertion and moderate Cu dispersion. Its relatively higher and stronger Lewis acidity resulted in higher amount of dehydration products (ethylene), at the expense of acetaldehyde and ultimately butadiene. The acetamide elimination route appeared better suited for the ETB reaction, as it leads to appropriate Lewis acidity and Cu nanoparticles below 15 nm, with an apparent spatial proximity between these sites. This advantageous configuration led to significantly higher BD selectivity (up to 74%) and overall productivity, owing to a high dehydrogenation activity towards acetaldehyde and to a mitigation of direct dehydration of ethanol.

The acetamide elimination route was thus further studied with different active sites loadings (Cu loading ranging from 2 to 5 wt % and Ta ranging from 1 to 4 wt %). In all cases, the catalyst texture was preserved, and both the tantalum insertion in the silica matrix and the Cu nanoparticles size were maintained. Upon optimization, a 4 wt % Ta and 4 wt % Cu was shown to reach high BD yield combined with low ethylene selectivity, corresponding to a productivity of 0.39 g_{BD} g_{cat}^{-1} h^{-1}, which compares advantageously with previously reported activity levels in identical reaction conditions.

The use of non-hydrolytic sol-gel routes allowed us to answer some questions asked in the objectives. First, the ether route and the acetamide elimination route yielded Ta sites with different natures and thus, different acidity and catalytic performance (question (i)). Ether-based catalysts formed less dispersed, less active TaOx clusters and acetamide-based catalysts formed more dispersed, more active embedded Ta sites. Same for Cu, as its dispersion in the form of CuO nanoparticles was favorable in the acetamide elimination route, increasing the proximity between the two types of active sites, mitigating unwanted side-products (question (ii)).

CHAPTER 7: Cu–Ta catalysts prepared by advanced non-hydrolytic sol-gel: taking the best out of the ether and acetamide routes

Cu–Ta catalysts prepared by advanced non-hydrolytic sol-gel: taking the best out of the ether and acetamide routes

7.1 Abstract

This chapter tackles the development of a hybrid synthesis protocol, in an attempt to benefit from the respective advantages of the ether route (texture) and the acetamide elimination route (active site dispersion) to obtain a bifunctional Ta-Cu catalyst active in the ethanol-to-butadiene reaction. The one-pot mixing of both synthesis precursors yields catalysts with mesoporous texture (SSA>680 $m^2\ g^{-1}$ and pore diameters above 15 nm) and well dispersed acid sites; yet, catalytic results are unsatisfactory. This appears related to the formation of ether-like acidity, described in the last chapter as not suited for the ETB reaction. Thus, we propose the concept of "delayed addition": adding the "acetamide elimination route" reagents 8 hours after the start of a regular "ether route" synthesis, we obtain catalysts with advantageous properties. Catalysts are mesoporous with high SSA (>850 $m^2\ g^{-1}$), open texture (average pore diameter above 5 nm), and well dispersed Ta sites and Cu nanoparticles below 10 nm. Correspondingly, catalysts reach improved BD yields. By optimizing the Ta loading to reduce dehydration by-products , the ether/acetamide ratio and the delay between the precursors additions, we obtained an optimized 2 wt % Ta and 4 wt % Cu catalyst featuring mesoporous texture (SSA=840 $m^2\ g^{-1}$; V_p=0.70 $cm^3\ g^{-1}$; $D_{p,BJH}$=8 nm) with adequate acidity, incorporated Ta active sites and dispersed Cu nanoparticles. The latter achieved a BD productivity of 0.26 $g_{BD}\ g_{cat}\ h^{-1}$.

7.2 Introduction

In the previous chapter,[126] we compared two non-hydrolytic sol-gel synthesis pathways, the ether route and the acetamide elimination route. The bifunctional catalysts synthesized via the ether route displayed high mesoporous texture but excessive acidity and low proximity between Ta and Cu sites that led to poor catalytic activity. However, the acetamide elimination route also yielded materials with mesoporous texture (through the use of Pluronic F127 as a templating agent) but with moderate Lewis acidity brought by inserted Ta atoms, well dispersed CuO nanoparticles. With close proximity between the two different active sites, catalytic performance of acetamide-made catalysts outclassed ether-made catalysts.

Here, we combine the two NHSG synthesis routes, the ether and acetamide elimination routes to provide a synthesis protocol leveraging the advantages of both synthesis pathways. On the one hand, we are aiming for a mesoporous catalyst without the need of a templating agent, as obtained

through the ether route, and on the other hand, we want to obtain active sites with correct acidity, dispersion and proximity. First, a direct mixing in one-step of the two synthesis routes will be used.

To improve upon it, the concept of "delayed addition" will be introduced and leveraged. Already successfully used in NHSG to improve catalytic performance in ethylene dehydration,[185,203] the "delayed addition" is a two-step synthesis process. In previous examples, only the active sites precursors were added to the reaction mixture 8 hours after the polycondensation between ether-based precursors had started. Here, both the addition of acetamide-based precursors and active sites precursors will take place after a first separate polycondensation between ether-based precursors. To go into more details, we will first mix ether-based precursors with a catalytic amount of Lewis acid to start the polycondensation. After a definite period of polycondensation between the ether precursors, acetamide-based precursors and active sites precursors will be added to the reaction mixture. Doing so, we hope to form an ether-based highly porous silica framework combined with acetamide-based active sites that will display higher Ta insertion and stabilized small CuO nanoparticles with favourable spatial distribution.

7.3 Results and discussion

7.3.1 Direct catalyst synthesis with a mixture of ether route and acetamide elimination route precursors

The first experiments combine precursors of both ether and acetamide elimination routes in different ratios. Figure VII.1 shows type IV isotherms with H3 hysteresis loops for all catalysts. All catalysts are mesoporous, with large SSA's above 680 $m^2\ g^{-1}$, mesopore volume superior to 0.82 $cm^3\ g^{-1}$ and an average mesopore diameter between 5 and 8 nm (Table VII.1). Compared to a catalyst synthesized exclusively via the ether route (Et-2Ta2Cu, Table VI.1), the textural properties are very similar (SSA=640 $m^2\ g^{-1}$; V_p=0.91 $cm^3\ g^{-1}$; D_{meso}=6.2 nm for Et-2Ta2Cu) and indicates that the acetamide fraction do not hinder the mesoporosity of the mixed catalysts. As expected, the pore volume decreases when the ratio ether/acetamide decreases, as the acetamide elimination route natively yield microporous catalysts. The BJH adsorption curves (Figure VII.1) show a similar maximum of pore volume around 15 nm, further confirming the mesoporous nature of ether-acetamide catalysts, despite the absence of surfactant.

XPS ratios of Si/Ta and Si/Cu tend to decrease as the proportion of acetamide precursors increases (Table VII.1), sign that Ta and Cu atoms are less dispersed on the surface when the proportion of acetamide elimination route increases (in line with our observation of the pure “Ac” and “Et” routes (see Section 6.3.1, Table VI.1)).

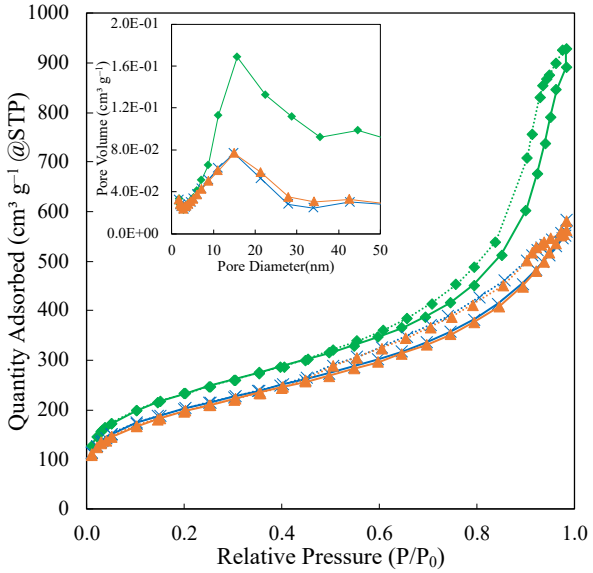

Figure VII.1: N_2-physisorption isotherms and BJH pore size distribution profiles (inset) of 60Et4Ac-4Ta4Cu (green ◊), 58Et6Ac-4Ta4Cu (blue ×), 56Et8Ac-4Ta4Cu (orange Δ).

Table VII.1: Textural properties and XPS ratios for ether-acetamide direct mixing.

Sample	S_{BET} ($m^2\ g^{-1}$)	V_{meso} ($cm^3\ g^{-1}$)[a]	D_{meso} (nm)[b]	Surface Si/Ta[c]	Surface Si/Cu[c]
60Et4Ac-4Ta4Cu	820	1.32	7.6	90	100
58Et6Ac-4Ta4Cu	710	0.82	5.7	62	86
56Et8Ac-4Ta4Cu	680	0.84	5.7	59	76

[a] calculated as ((total pore volume) – (micropore volume)), [b] calculated as $4V_{meso}/A_{meso}$ [c] Calculated by XPS

FTIR analyses on the these 3 catalysts (Figure VII.2) gave very similar spectra, with the main absorption bands typically originating from the amorphous silica matrix.[206-210] The band at 750-850 cm^{-1} is attributed to the symmetric vibration of Si–O–Si bonds whereas the most intense absorption band at 1050-1065 cm^{-1} is ascribed to the antisymmetric stretching vibration of Si–O–Si. Importantly, the distinct band at 950 cm^{-1} can be attributed to the Si–O–Ta stretching mode (even though a contribution of Si–OH vibration is possible too), since this band is not present in the pristine SiO_2

spectrum.[211,212,230] It is a proxy for the good insertion of Ta in silica. Between the different ether to acetamide ratios, the band remains similar and does not allow suspecting a different degree of insertion of Ta in the silica matrix as a function of the precursors proportion.

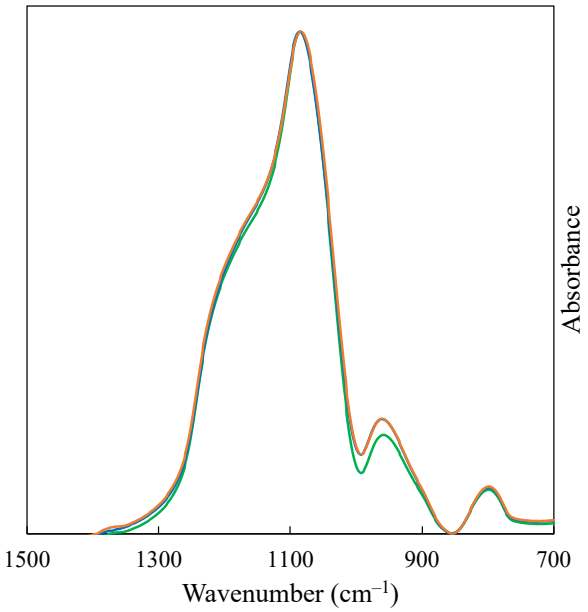

Figure VII.2: FTIR spectra of 60Et4Ac-4Ta4Cu (green curve), 58Et6Ac-4Ta4Cu (blue), 56Et8Ac (orange curve).

Finally, the three catalysts were tested in the ethanol-to-butadiene and poor performance were observed (Table VII.2). Furthermore, no clear trend is observed. Whereas 60Et4Ac and 58Et6Ac mainly produce acetaldehyde and have ethanol conversion around 50 %, 56Et8Ac has ethanol conversion above 80 % and an ethylene selectivity of 66 %. Such results point to an unsatisfactory speciation and dispersion of the active sites, already encountered in the ether-based catalyst Et-2Ta2Cu studied in the previous chapter. Consequently, we can deduce that the addition of acetamide precursors was not sufficient to yield acetamide-like Ta sites in close proximity to dispersed CuO nanoparticles. Additional measurements like FTIR on adsorbed pyridine, close examinations of the Ta peak in XPS could help justify the poor catalytic performance. Here, the priority was given to the study of the delayed addition.

Table VII.2: Catalytic performance of catalysts prepared by direct mixing of ether and acetamide elimination routes. Reaction conditions: T°=325 °C, WHSV=1.1 h^{-1}.

Sample	X_{EtOH} (%)	S_{BD} (%)	S_{AA} (%)	S_{EY} (%)	Y_{BD} (%)	P_{BD} (g_{BD} g_{cat}^{-1} h^{-1})
60Et4Ac-4Ta4Cu	44.6	7.8	87.7	4.4	3.5	0.023
58Et6Ac-4Ta4Cu	58.2	9.4	78.9	11.7	5.5	0.036
56Et8Ac-4Ta4Cu	83.9	6.9	27.3	65.8	5.8	0.039

7.3.2 Delayed addition of the acetamide precursors

Interestingly, when we delay the addition of the acetamide and active sites precursors by 8 hours (56Et8Ac-4Ta4Cu-D8h), allowing for a first preliminary polycondensation between the ether precursors, the SSA increases to 850 m^2 g^{-1} and the mesopore volume reaches 1.05 cm^3 g^{-1} without the need for Pluronic F127 as templating agent. Practically, it means that the delayed addition of the active sites and acetamide precursors successfully allowed for the separate polycondensation of the ether precursors to form an advantageous texture.

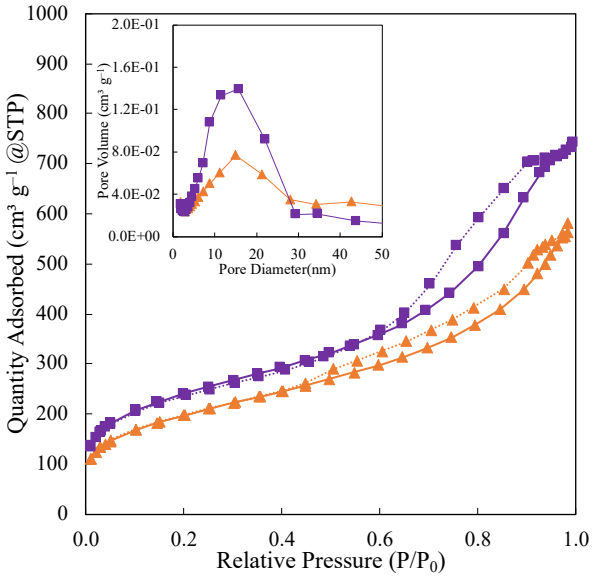

Figure VII.3: N_2-physisorption isotherms and BJH pore size distribution profiles (inset) of 56Et8Ac-4Ta4Cu (orange Δ), 56Et8Ac-4Ta4Cu-D8h (purple ■).

Table VII.3: Textural properties and XPS ratios for the study of the delayed addition of acetamide and active sites precursors.

Sample	S_{BET} ($m^2\ g^{-1}$)	V_{meso} ($cm^3\ g^{-1}$)[a]	D_{meso} (nm)[b]	Surface Si/Ta[c]	Surface Si/Cu[c]
56Et8Ac-4Ta4Cu	680	0.84	5.7	59	76
56Et8Ac-4Ta4Cu-D8h	850	1.05	6.7	50	81

[a] calculated as ((total pore volume) – (micropore volume)), [b] calculated as $4V_{meso}/A_{meso}$ [c] Calculated by XPS

Si/Ta ratio obtained by XPS is higher for 56Et8Ac-4Ta4Cu compared to 56Et8Ac-4Ta4Cu-D8h, sign that Ta is more present on the catalysts surface when the ether precursors are allowed to react before the addition of the acetamide precursors (Table VII.1). This can be explained by the separate polycondensation of the ether precursors, already preforming the structure of the silica matrix. After addition of the acetamide precursors with the silica oligomers, tantalum is less likely to concentrate in the bulk of the material compared to the surface. However, no significant difference is observed for the Si/Cu ratios since the calcination process is responsible for the spatial re-distribution of copper and for the formation of copper nanoparticles. Any difference in Cu location is probably levelled off by the applied thermal treatment.

In FTIR, all catalysts feature the characteristic band at 950 cm^{-1} but no significant difference is observed between the samples (Figure VII.4), indicating a similar Ta insertion between the delayed catalyst and non-delayed catalyst.

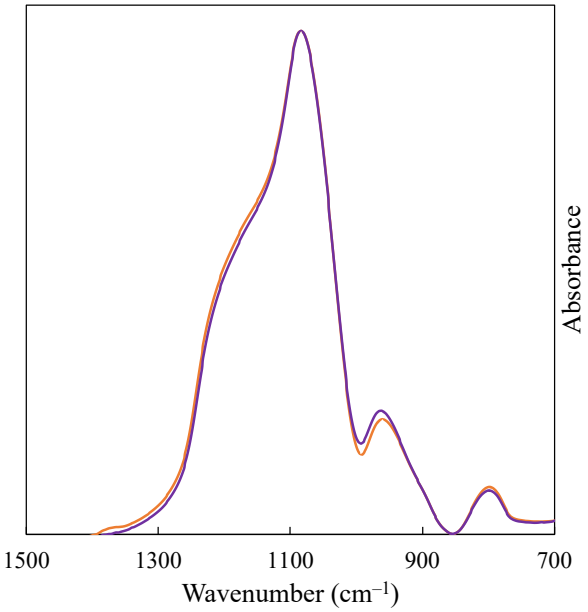

Figure VII.4: FTIR spectra of 56Et8Ac-4Ta4Cu (orange curve) and 56Et8Ac-4Ta4Cu-D8h (purple curve).

In terms of total acidity, NH_3-TPD measurements point out a practically identical quantity of acid sites between the two samples (ca. 2.4 10^{-1} mmol g^{-1}, Table VII.4). Furthermore, both catalysts display a similar desorption profile (Figure VII.5). Both curves display a maximum of desorption around 250 °C, illustrating the presence of only one type of acid sites of moderate strength. Interestingly, we showed in the previous chapter the catalysts prepared via the ether route yielded a shoulder in the NH_3-TPD desorption curve (Figure VI.1c). This feature – which was associated to the presence of poorly dispersed TaO_x oligomers – is still present here, while it was absent in the thermograms of the catalysts prepared by the acetamide elimination route. This leads us to believe that the catalysts may not contain enough acetamide precursors to obtain in sufficient quantity the homogeneous and active Ta sites that yielded better catalytic performance. Another hypothesis is that even after 8 hours of separate polycondensation, unreacted ether precursors are still in large abundance and still react with the Ta precursors and give rise to sites responsible of that shoulder in the NH_3-TPD desorption profiles.

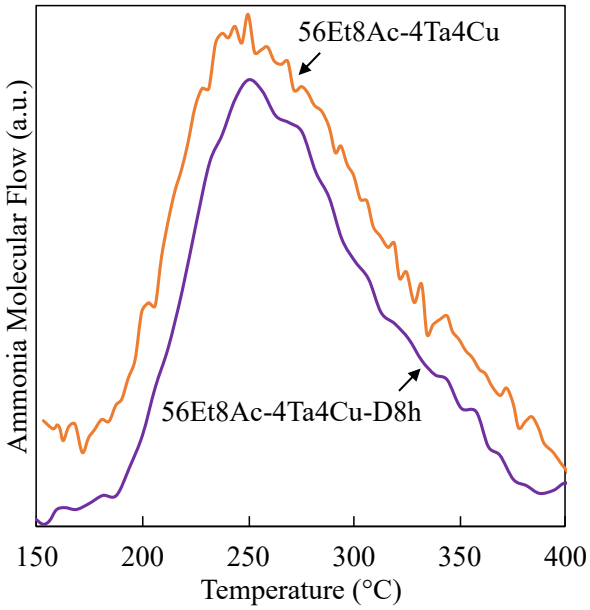

Figure VII.5: NH_3-TPD profiles of 56Et8Ac-4Ta4cu (top orange curve) and 56Et8Ac-4Ta4Cu-D8h (bottom purple curve).

Table VII.4: Acidity measurements by NH_3-TPD for catalysts with and without the use of a delayed synthesis process.

Sample	Acid sites (mmol g^{-1})	Acid sites (mmol m^{-2})
56Et8Ac-4Ta4Cu	2.3 10^{-1}	3.3 10^{-4}
56Et8Ac-4Ta4Cu-D8h	2.5 10^{-1}	2.9 10^{-4}

Figure VII.6 and Table VII.5 describe the influence of an 8-hour delayed addition of the acetamide precursors on the catalytic performance. Even though the overall ethanol conversion decreases from 84 to 71 % for 56Et8Ac-4Ta4Cu-D8h compared to 56Et8Ac-4Ta4Cu, a substantial increase in BD selectivity, from 7 to 36 %, is observed. In parallel, a decrease in acetaldehyde and ethylene selectivity is observed for 56Et8Ac-4Ta4Cu-D8h. These two catalytic tests hint at the advantage of using a delayed synthesis approach to control the type of active sites our catalyst possesses. Indeed, the delayed addition favours the formation of more abundant Ta sites active in the aldol condensation, as proven by the decrease in acetaldehyde selectivity combined with the increased BD selectivity, resulting in a 4-fold improvement in BD productivity. However, this also results in a relatively large selectivity for the direct (unwanted) dehydration to ethylene. Since acetamide-based catalysts yielded a EY selectivity below 5 % (Table VI.6), we can argue that

the acetamide fraction is too small or the Ta loading is too high. On this basis, we decided to further improve the protocol.

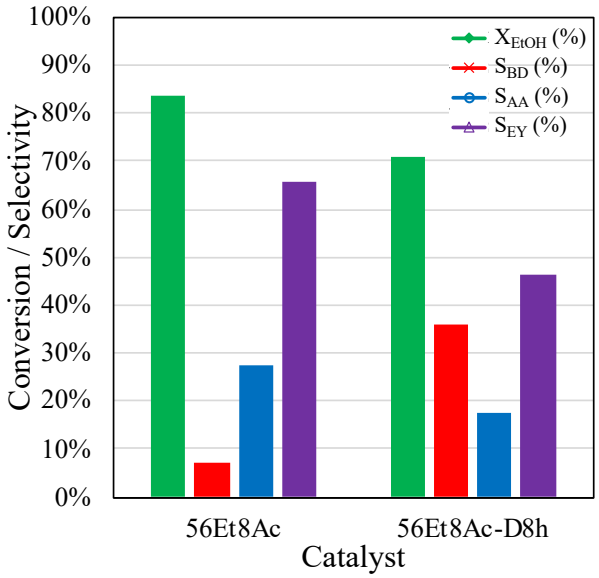

Figure VII.6: Influence of the delayed addition of acetamide and active sites precursors on the catalytic performance. Reaction conditions: T°=325 °C, WHSV=1.1 h^{-1}.

Table VII.5: Catalytic performance of catalysts studying the influence of the delayed addition of acetamide and active sites precursors. Reaction conditions: T°=325 °C, WHSV=1.1 h^{-1}.

Sample	X_{EtOH} (%)	S_{BD} (%)	S_{AA} (%)	S_{EY} (%)	Y_{BD} (%)	P_{BD} (g_{BD} g_{cat}^{-1} h^{-1})
56Et8Ac-4Ta4Cu	83.9	6.9	27.3	65.8	5.8	0.04
56Et8Ac-4Ta4Cu-D8h	70.8	35.8	17.4	46.5	25.3	0.17

7.3.3 First optimization of the delayed addition protocol

In this section, the synthesis protocol is modified by decreasing the Ta loading (to decrease the ethylene production) and increasing the delay between the first polycondensation of the ether precursors and the addition of the active sites and acetamide precursors. The idea behind these modifications is to increase the quality of the Ta sites, meaning Lewis acid sites of moderate acidity formed through the acetamide elimination route.

Figure VII.7 shows type IV isotherms with a H3 hysteresis loop for both 4Ta4Cu-D8h and 2Ta4Cu-D24h. Both catalysts have a SSA of 850 $m^2\ g^{-1}$ (Table VII.6). However, the mesopore volume and average mesopore diameters are higher for 2Ta4Cu-D24h. Interestingly, BJH pore size distribution profiles (Figure VII.7, inset) depict a similar maximum of pore volume around 15 nm, consistent with pure ether route samples like Et-2Ta2Cu described on Figure VI.1a. The higher pore volume at 15 nm indicates that by giving more time to the first polycondensation between ether precursors, we managed to increase the overall pore volume of our resulting material.

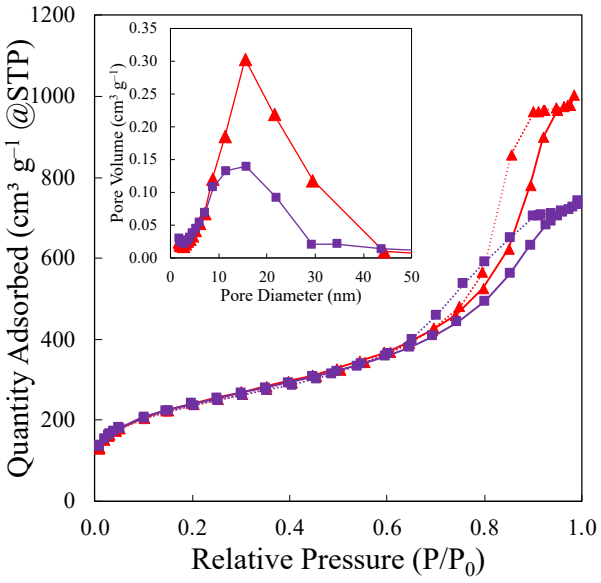

Figure VII.7: N_2-physisorption data and BJH pore size distribution profiles (inset) of 56Et8Ac-4Ta4Cu-D8h (purple ■) and 56Et8Ac-2Ta4Cu-D24h (red Δ).

Table VII.6: Textural properties and XPS ratios for the study of the delayed addition conditions.

Sample	S_{BET} ($m^2\ g^{-1}$)	V_{meso} ($cm^3\ g^{-1}$)[a]	D_p (nm)[b]	Surface Si/Ta[c]	Surface Si/Cu[c]
56Et8Ac-4Ta4Cu-D8h	850	1.05	6.7	50	81
56Et8Ac-2Ta4Cu-D24h	850	1.59	9.7	102	68

[a] calculated as ((total pore volume) – (micropore volume)), [b] calculated as $4V_{meso}/A_{meso}$ [c] Calculated by XPS

Acidity measurements by NH_3-TPD highlight the correlation between the Ta loading and the total acidity of the catalyst, as the quantity of acid sites decrease from $2.5\ 10^{-1}$ to $1.1\ 10^{-1}$ mmol g^{-1} for 4Ta4Cu-D8h and 2Ta4Cu-D24h respectively. However, the decrease is not exactly proportional to the Ta loading. A hypothesis is that the Ta precursors had a higher likelihood of reacting with uncondensed ether precursors on the D8h sample than on the D24h, resulting in higher “ether” acidity, known to yield more acid sites than acetamide as seen in the previous chapter (Table VI.2). Nevertheless, both samples have a maximum of ammonia desorption around 250 °C, sign of acid sites of similar strength. Arguably, we can still observe in Figure VII.8 the shoulder explained previously in Figure VI.1c, leading us to believe that it might be interesting to further decrease the ether/acetamide ratio to even further favour the formation of acid sites resulting from the reaction between the Ta and the acetamide precursors.

Si/Ta ratios are proportional to the Ta loading (Table VII.6). Indeed, as the Ta loading decreases by half from 4 wt % to 2 wt %, the Si/Ta surface ratio increases from 50 to 102. This indicates that the longer delay between the first ether polycondensation and the addition of the acetamide precursors did not modify the spatial distribution of Ta. However, Si/Cu ratio decreased when the delay switched from 8 hours to 24 hours, from 81 to 68. This could highlight a higher presence of small CuO nanoparticles on the surface of the catalysts, as the size of these nanoparticles also influences the Si/Cu ratio.

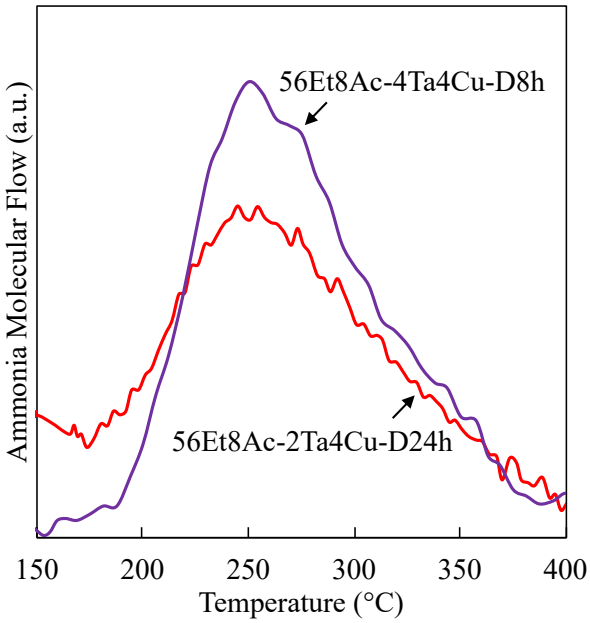

Figure VII.8: NH_3-TPD profiles of 56Et8Ac-4Ta4Cu-D8h (purple curve) and 56Et8Ac-2Ta4Cu-D24h (red curve).

Table VII.7: Acidity measurements by NH_3-TPD for different delayed synthesis conditions.

Sample	Acid sites (mmol g^{-1})	Acid sites (mmol m^{-2})
56Et8Ac-4Ta4Cu-D8h	2.5 10^{-1}	2.9 10^{-4}
56Et8Ac-2Ta4Cu-D24h	1.1 10^{-1}	1.3 10^{-4}

The decrease in Ta loading and the longer time allowed for the first polycondensation markedly improved the catalytic performance (Figure VII.7). Even though the ethanol conversion decreased slightly, an impressive BD selectivity of 60 % was reached for 56Et8Ac-2Ta4Cu-D24h. Along this, a notable decrease in ethylene selectivity was observed, sign of a better balance between the two types of active sites. Consequently, we can state than letting the polycondensation occur between the ether precursor for the first 24 hours gave us a catalyst with improved pore volumes and more adequate acidity resulting in a 47 % increase in BD productivity, reaching 0.25 g_{BD} g_{cat} h^{-1} (Table VII.8).

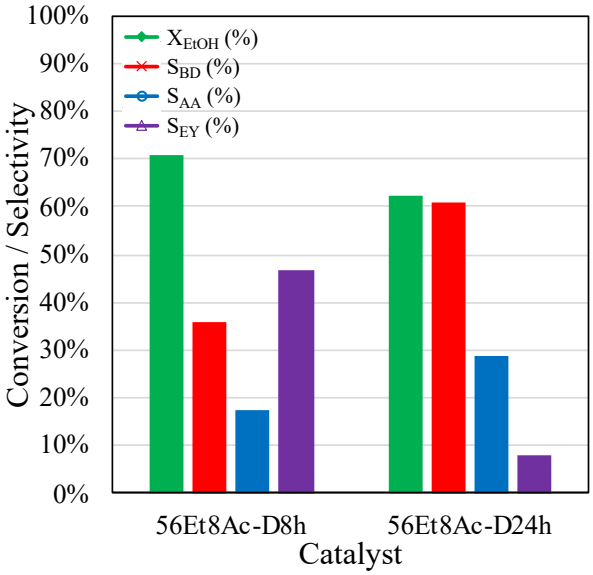

Figure VII.9: Optimization of delayed addition conditions on catalytic performance. Reaction conditions: T°=325 °C, WHSV=1.1h^{-1}.

Table VII.8: Catalytic performance of catalysts for the optimization of the delayed addition procedure. Reaction conditions: T°=325 °C, WHSV=1.1 h^{-1}.

Sample	X_{EtOH} (%)	S_{BD} (%)	S_{AA} (%)	S_{EY} (%)	Y_{BD} (%)	P_{BD}[a]
56Et8Ac-4Ta4Cu-D8h	70.8	35.8	17.4	46.5	25.3	0.17
56Et8Ac-2Ta4Cu-D24h	62.2	60.9	28.6	8.2	37.9	0.25

[a] P_{BD} is in (g_{BD} g_{cat}^{-1} h^{-1})

7.3.4 Further improvement of the delayed addition protocol

The final section of this chapter will study the influence of different ether/acetamide precursors ratios by keeping the Ta and Cu loadings constant (2 wt % Ta and 4 wt % Cu), as well as the delay between the ether polycondensation and the addition of the Ta, Cu and acetamide precursors (24 hours). Figure VII.10 highlights type IV isotherms for all catalysts. Following IUPAC classification of hysteresis loops, 48Et16Ac, 40Et24Ac and 32Et32Ac follow a H2 loop, corresponding to ordered mesoporous materials. For 56Et8Ac, we observe a H3 loop, characterizing aggregates of plate-like particles giving rise to slit-shaped pores.[224] Interestingly, as the acetamide proportion increases, the SSA and micropore volume stays relatively constant but the average mesopore size decreases, from 9.7 nm for 56Et8Ac to 4.0 nm for 32Et32Ac (Table VII.9). 48Et16Ac does not follow this trend and seemed

to have undergone a sort of pore collapse, leading to a fast decrease in SSA, pore volume and pore diameters. One hypothesis might be an unusual calcination process that should be remade to ensure the data in Figure VII.10 and Table VII.9. Apart from this exception, the increase in acetamide abundance decreased the average pore diameter determined by the BJH profiles (Figure VII.10, inset), from ca. 15 nm for 56Et8Ac to ca. 8 nm for 32Et32Ac. These results make sense since the ether route natively yields mesoporous materials[76,126,185,203,214] whereas the acetamide elimination route will yield microporous materials in the absence of templating agents.[7,225,226]

Table VII.9: Textural properties and XPS ratios for "delayed" catalysts with different ether/acetamide ratios.

Sample	S_{BET} ($m^2\ g^{-1}$)	V_μ ($m^2\ g^{-1}$)[a]	V_{meso} ($cm^3\ g^{-1}$)[b]	D_{meso} (nm)[c]	Surface Si/Ta[d]	Surface Si/Cu[d]
56Et8Ac-2Ta4Cu-D24h	850	150	1.59	9.7	102	68
48Et16Ac-2Ta4Cu-D24h	670	200	0.72	6.2	87	63
40Et24Ac-2Ta4Cu-D24h	750	180	1.04	7.1	108	75
32Et32Ac-2Ta4Cu-D24h	840	260	0.60	4.0	103	63

[a] Calculated via t-plot, [b] calculated as ((total pore volume) – (micropore volume)), [c] calculated as $4V_{meso}/A_{meso}$ [d] Calculated by XPS

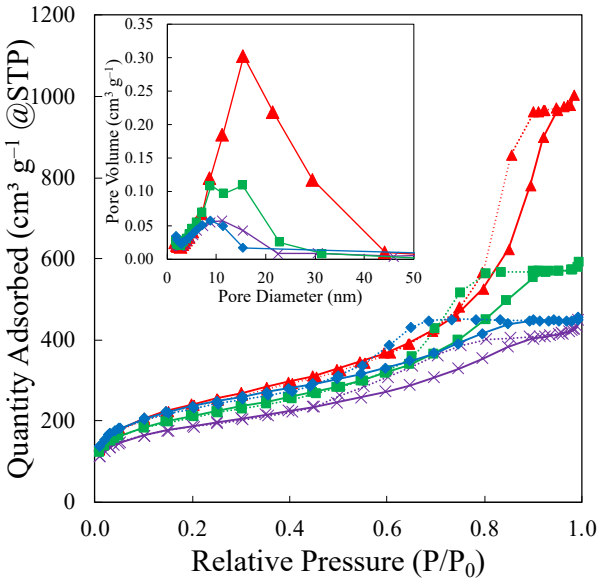

Figure VII.10: N_2-physisorption isotherms and BJH pore size distribution profiles (inset) of 56Et8Ac-2Ta4Cu-D24h (red Δ) , 48Et16Ac-2Ta4Cu-D24h (purple ×), 40Et24Ac-2Ta4Cu-D24h (green ■), 32Et32Ac-2Ta4Cu-D24h (blue ○).

NH_3-TPD desorption profiles on Figure VII.11 depict a similar thermogram all catalysts except 32Et32Ac-2Ta4Cu-D24h. The peak for 32Et32Ac-2Ta4Cu-D24h appears sharper and is slightly shifted to a lower temperature, in accordance with the desorption profile of Ac-2Ta2Cu shown on Figure VI.1c. Furthermore, the total quantity of acid sites is lower for 32Et32Ac-2Ta4Cu-D24h (Table VII.10). The combination of N_2-physisorption data and NH_3-TPD measurements lead us to consider that 32Et32Ac-2Ta4Cu-D24h possesses the texture attributed to a catalyst obtained by the ether route and the Ta active sites configuration obtained by using the acetamide elimination route. For the three other samples, a similar acidity is observed.

Table VII.10: Acidity measurements by NH_3-TPD for “delayed” catalysts with different ether/acetamide ratios.

Sample	Acid sites (mmol g^{-1})	Acid sites (mmol m^{-2})
56Et8Ac-2Ta4Cu-D24h	$1.1\ 10^{-1}$	$1.3\ 10^{-4}$
48Et16Ac-2Ta4Cu-D24h	$9.6\ 10^{-2}$	$1.4\ 10^{-4}$
40Et24Ac-2Ta4Cu-D24h	$6.5\ 10^{-2}$	$9.3\ 10^{-5}$
32Et32Ac-2Ta4Cu-D24h	$5.0\ 10^{-2}$	$5.7\ 10^{-5}$

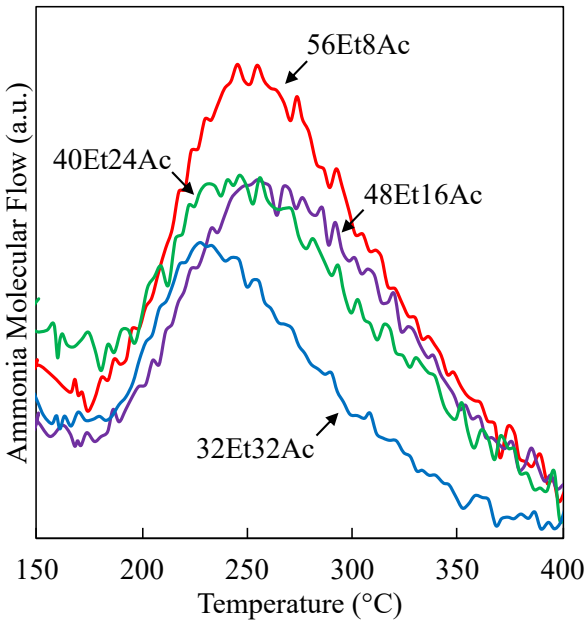

Figure VII.11: NH_3-TPD of “delayed” catalysts with different ether/acetamide ratios.

FTIR spectra on Figure VII.12 features the distinct band at 950 cm^{-1} originating from Si–O–Ta bonds for all catalysts, although less marked for 56Et8Ac. The origin of this diminished signal is unknown as all catalysts contain the same amount of Ta and should therefore form these typical bonds. Furthermore, we showed on Figure VI.1b that the nature of the synthesis routes did not influence the intensity of the IR band at 950 cm^{-1}. Apart from 56Et8Ac, all studied catalysts have this distinct shoulder, sign of a good interaction and incorporation of Ta in the silica matrix.

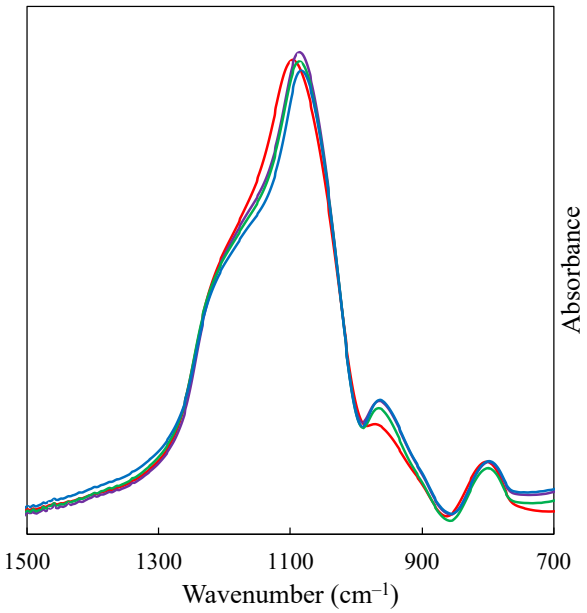

Figure VII.12: FTIR spectra of 56Et8Ac-2Ta4Cu-D24h (red), 48Et16Ac-2Ta4Cu-D24h (purple), 40Et24Ac-2Ta4Cu-D24h (green) and 32Et32Ac-2Ta4Cu-D24h (blue).

In terms of catalytic performance, all catalysts except 40Et24Ac have similar ethanol conversion, close acetaldehyde selectivity and low ethylene selectivity (Figure VII.13). However, a slightly higher BD selectivity of 67 % is observed for 32Et32Ac; attributed again to a higher tendency of converting acetaldehyde to perform the second half of the reaction cascade. Consequently, a satisfactory BD productivity of 0.26 g_{BD} g_{cat} h^{-1} is achieved at 325 °C and WHSV=1.1 h^{-1} (Table VII.11). The 40Et24Ac sample has higher ethylene selectivity than the other materials, with 33 % instead of less than 10 % (Table VII.11). This modest catalytic performance does not fit the narrative told by N_2-physisorption, NH_3-TPD and FTIR, hinting at a great texture, well dispersed Ta and a suitable acidity for the ETB reaction.

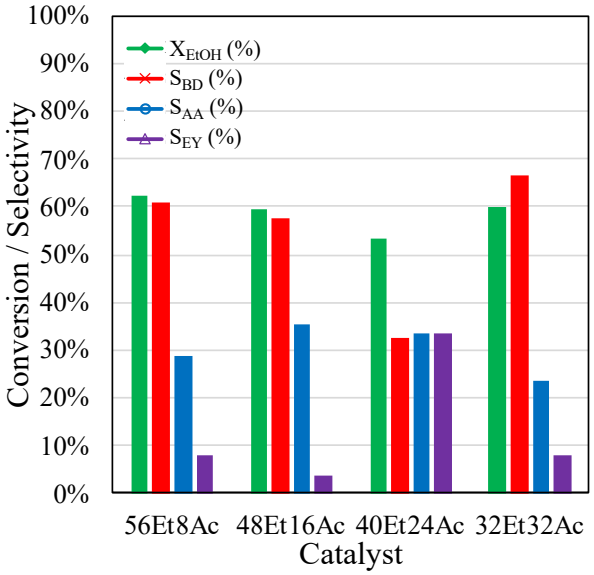

Figure VII.13: Catalytic performance of "delayed" catalysts with different ether/acetamide ratios. Reaction conditions: T°=325 °C, WHSV=1.1 h^{-1}, time-on-stream=4 hours.

Table VII.11: Catalytic performance and BD productivity of "delayed" catalysts with different ether/acetamide ratios. Reaction conditions: T°=325 °C, WHSV=1.1 h^{-1}, time-on-stream=4 hours.

Sample	X_{EtOH} (%)	S_{BD} (%)	S_{AA} (%)	S_{EY} (%)	Y_{BD} (%)	P_{BD}[a]
56Et8Ac-2Ta4Cu-D24h	62.2	60.9	28.6	8.2	37.9	0.25
48Et16Ac-2Ta4Cu-D24h	59.6	57.7	35.6	3.9	34.4	0.23
40Et20Ac-2Ta4Cu-D24h	53.4	32.6	33.4	33.3	17.4	0.12
32Et32Ac-2Ta4Cu-D24h	59.8	66.5	23.4	8.0	39.7	0.26

[a] P_{BD} is in (g_{BD} g_{cat}^{-1} h^{-1})

The stability of the four best catalysts in this chapter is depicted for the first 4 hours of the catalytic run on Figure VII.14. Overall, the same trend as all other catalysts tested in this work is observed. A steady decrease in ethanol conversion and BD selectivity combined with an increase in acetaldehyde selectivity is featured in all catalysts. However, the decrease in BD selectivity is less pronounced for 32Et32Ac, with a 38 % relative decrease, potentially indicating a more stable and coke resistant catalyst. In the future, the optimal reaction conditions found in section 5.3.4 could be applied to these catalysts to increase overall performance and stability of the NHSG-made "delayed" catalysts.

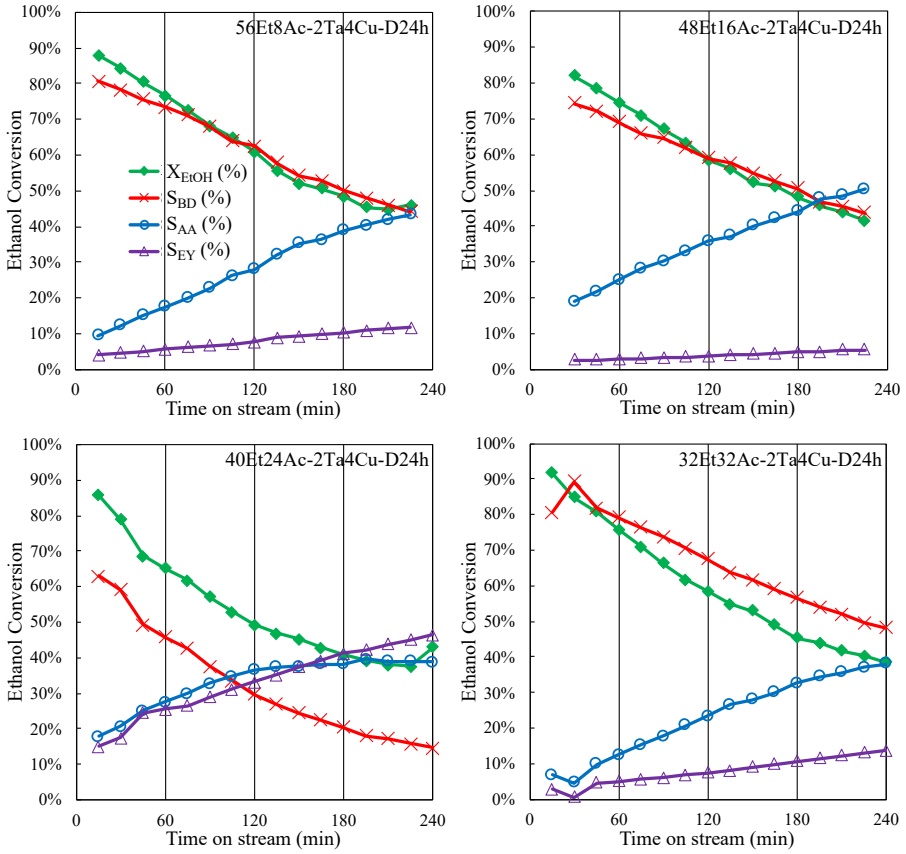

Figure VII.14: Evolution of ethanol conversion and main products selectivities over time at different ether/acetamide ratios. Reaction conditions: T°=325 °C, WHSV=1.1 h^{-1}.

7.4 Conclusion

The last chapter of this PhD thesis built upon previous results comparing distinct NHSG synthesis routes, the ether route and the acetamide elimination route, by developing a synthesis protocol that merged both families of molecular precursors. For this, a first direct one-step mixing of different ether/acetamide precursors ratio was studied and deemed poorly effective in the ethanol-to-butadiene reaction. A distinct synthesis procedure was then developed to first trigger a separate polycondensation between the precursors from the ether route for a defined amount of time before adding the active sites and the acetamide elimination route precursors. This “delayed addition” procedure allowed for an improved texture and catalytic performance

compared to the direct mixing. After an optimization of the “delayed addition” protocol, our best catalyst with an equimolar amount of ether and acetamide precursors, 2 wt % of Ta and 4 wt % of Cu, and after delaying the addition of Ta, Cu and acetamide precursors for 24 hours achieved a BD productivity of 0.26 g_{BD} g_{cat} h^{-1}.

Looping back to the research questions debated in the objectives, the delayed addition procedure allowed for a control on the Ta speciation and a successful insertion in the silica matrix (question (i)). By using such synthesis protocol, the quantity of Ta was able to be decreased by a factor 2 while keeping correct catalytic performance with low selectivity in dehydration by-products, hinting at a great dispersion of Ta sites and Cu nanoparticles (question (ii)).

CHAPTER 8: GENERAL CONCLUSION AND PERSPECTIVES

8.1 General conclusion

In this PhD thesis, we displayed the need for an alternative sustainable catalytic production pathway of 1,3-butadiene from bioethanol, mitigating our dependence towards the heavily polluting and energy-consuming steam cracking of naphtha, responsible for more than 95 % of current 1,3-butadiene supply.

In this goal, we aimed at developing a new synthesis method to synthesize in an easy, elegant and straight-forward approach a catalyst active in the ethanol-to-butadiene reaction. Through a review of recent and key literature, we managed to extract limitations of currently used catalysts synthesis protocols: most of them either rely on long, intricate and multi-step processes that sometimes require the use of toxic compounds. To respond to those limitations, we investigated sol-gel chemistry, and more specifically the aerosol-assisted sol-gel and the non-hydrolytic sol-gel, to develop innovative synthesis protocols to synthesize in a limited number of steps a bifunctional catalyst active in the ethanol-to-butadiene reaction. The challenges were to avoid mass transfer limitations by synthesizing mesoporous materials, correctly incorporate the first metal in the silica matrix to bring moderate Lewis acidity, allow for the formation of metal nanoparticles close to the other type of active site to maximize our chances to a productive catalyst.

The first chapter tackled the use of the aerosol-assisted sol-gel to synthesize highly homogeneous bifunctional Ag-Ta catalysts with a mesoporous texture, highly inserted Ta species and well dispersed Ag nanoparticles. These properties allowed for the direct production of 1,3-butadiene from pure ethanol. Even after modifying the Ta and Ag loadings to improve catalytic performance, the bifunctional kept its advantageous properties. However, a limited BD productivity of 0.085 g_{BD} g_{cat} h^{-1} was achieved.

Building upon these take-aways, the second chapter studied the use of Cu instead of Ag as a redox agent in the aerosol-assisted sol-gel. Here, the diffusion limitations were assessed and no mass transfer problems were observed, showing the benefits of using mesoporous materials. The optimization of the Ta and Cu loadings allowed for a correct balance between acid and redox sites by keeping a mesoporous texture, highly dispersed Ta and Cu species even at higher nominal loadings, resulting in a superior catalyst with a BD productivity of 0.28 $g_{BD}\ g_{cat}^{-1}\ h^{-1}$. After investigation of the catalytic reaction parameters such as reaction temperatures, pre-reduction temperature and the co-feeding of gases, we were able to conduct a catalytic test in which we co-fed oxygen at a low concentration and a remarkable 1,3-butadiene productivity of 0.38 $g_{BD}\ g_{cat}^{-1}\ h^{-1}$ was achieved with a catalyst containing 4 wt % Ta and 4 wt % of Cu.

For the third chapter, two different non-hydrolytic sol-gel synthesis routes, the ether route and the acetamide elimination route, were used to effectively obtain Cu-Ta catalysts with incorporated Ta atoms in the silica matrix and small Cu nanoparticles below 20 nm. Comparing both routes, it appeared that the acetamide elimination route yielded a catalyst with appropriate Lewis acidity and smaller Cu nanoparticles of ca. 15 nm, resulting in better catalytic performance. In the second part, the Ta and Cu loadings were optimized in the acetamide elimination route to improve catalytic results. By doing so, the mesoporous texture was preserved, the Ta sites kept their adequate Lewis acidity and Cu nanoparticles remained small. In the end, a catalyst containing 4 wt % Ta and 4 wt % of Cu reached a 1,3-butadiene productivity of 0.38 $g_{BD}\ g_{cat}^{-1}\ h^{-1}$. Interestingly, that value is identical to the best productivity found in our best aerosol-made catalyst.

The final chapter tackled the development of an innovative synthesis protocol that combined the fundamentals of the ether route and the acetamide elimination route. First, precursors from both routes were mixed directly in precise proportions but the obtained catalysts produced minuscule amounts of 1,3-butadiene. Another approach of “delayed addition” was then developed where we first triggered a polycondensation of the ether precursors separately for 8 hours before adding acetamide, Ta and Cu precursors to the reaction mixture. Doing so, the catalyst was mesoporous, with well dispersed Ta sites resulting in a 1,3-butadiene productivity of 0.17 $g_{BD}\ g_{cat}^{-1}\ h^{-1}$. Further improvement of the “delayed addition” synthesis protocol allowed us to develop our best catalyst with an equimolar amount of ether and acetamide precursors, 2 wt % of Ta and 4 wt % of Cu, and after delaying the addition of

Ta, Cu and acetamide precursors for 24 hours achieved a BD productivity of 0.26 g_{BD} g_{cat} h^{-1}.

To finalize this study, Table C.1 summarizes the best catalysts obtained in each chapter in similar reaction conditions. Interestingly, the best catalyst in terms of ethanol conversion, 1,3-butadiene selectivity and thus 1,3-butadiene productivity is the non-hydrolytic sol-gel-made Ac-4Ta4Cu, with 0.39 g_{BD} g_{cat}^{-1} h^{-1} of productivity.

Table C.1: Comparison of our best catalysts studied in each chapter. Reaction conditions: T°=325 °C, WHSV=1.1 h^{-1}. AASG=aerosol-made, NH=non-hydrolytic sol-gel-made.

Sample	TOS (h)	X_{EtOH} (%)	S_{BD} (%)	Y_{BD} (%)	P_{BD} (g_{BD} g_{cat}^{-1} h^{-1})
AASG-2Ta5Ag	3	68.6	12.3	8.5	0.055
AASG-4Ta4Cu	3	81.7	53.3	44.1	0.28
AASG-4Ta4Cu (Co-Feed O_2)	4	91.3	64.0	58.4	0.38
NH-Ac-4Ta4Cu	4	81.8	73.5	60.1	0.39
NH-32Et32Ac-2Ta4Cu-D24h	4	59.8	66.5	39.7	0.26

Out of these catalytic results, trends have been researched to potentially find a link between great BD performance and certain properties. Since different Ta loadings were used throughout Table C.1 and Ta is known to catalyse the rate limiting step of the acetaldehyde condensation to acetaldol, the BD productivity was normalized per wt % of Ta in Table C.2. Figure C.1a puts into evidence the advantages of a porous material, with the normalized BD productivity (P_{BD}*) being correlated with the SSA. Even more so, the P_{BD}* increases as the mesoporous volume of the catalyst rises (Figure C.1b). Here, the catalyst synthesized by delayed addition in non-hydrolytic sol-gel markedly outperforms the bifunctional catalyst obtained via the simple acetamide elimination route since both have similar textural properties but the first one contains half the amount of Ta. This result points towards a higher accessibility of Ta active sites in the delayed synthesis protocol.

Table C.2: Relationship between normalized BD productivity and textural properties of our best catalysts.

Sample	S_{BET} (m^2 g^{-1})	V_{meso} (cm^3 g^{-1})	D_{meso} (nm)	P_{BD} (g_{BD} g_{cat}^{-1} h^{-1})	P_{BD}* (g_{BD} g_{cat}^{-1} wt% Ta^{-1} h^{-1})
AASG-2Ta5Ag	300	0.33	8.9	0.055	0.028
AASG-4Ta4Cu	520	0.37	6.9	0.28	0.070
NH-Ac-4Ta4Cu	830	0.58	4.2	0.39	0.098
NH-32Et32Ac-2Ta4Cu-D24h	840	0.59	4.0	0.26	0.13

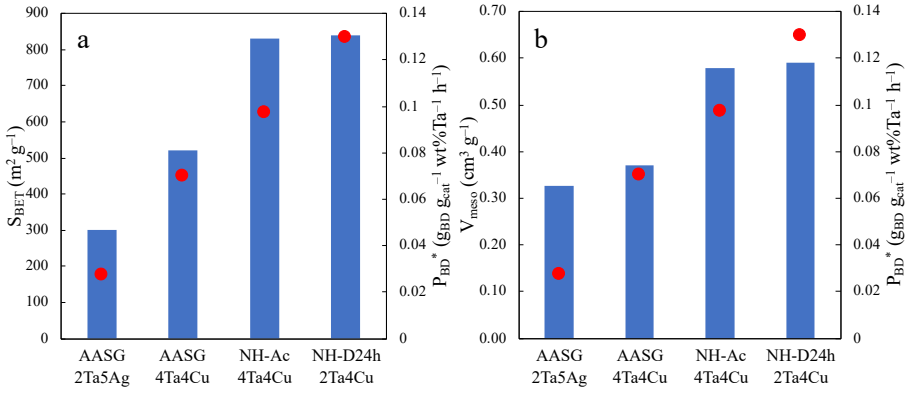

Figure C.1: Influence of the specific surface area (a) and the mesoporous volume (b) on the normalized BD productivity of the best catalysts. Blue histograms represent the specific surface area and red dots represent the BD productivity.

Besides the textural properties, the repartition of the different active sites between the surface of the catalyst and the bulk plays a significant part in the BD productivity (Table C.3 and Figure C.2). It is noted that since ICP proved that experimental values were close to nominal values for both aerosol and non-hydrolytic sol-gel, we assume the experimental ratios to be close to the nominal ones. Interestingly, when a higher Si/Ta XPS/Theo (Table C.3) is observed, BD productivity is systematically higher (Figure C.2a). As this ratio is higher, the absolute amount of Ta on the surface is lower than the overall composition, so this trend is counter intuitive. However, we can surmise that as the relative amount of neighbour Ta is smaller, the chance of forming isolated Ta sites is increased. Since such isolated Ta sites are the active sites in the rate-determining step of the BD formation (aldol condensation), it can be put forward that a high BD productivity is not only dependent from Ta present on the catalysts surface but also on the Ta configuration in these surface sites (linked to dispersion).

Even though the same trend is observed for Cu (Table C.3), the explanation is different since small dispersed CuO nanoparticles on the catalysts surface will result in a lower Si/Cu ratio compared to larger less dispersed CuO nanoparticles. Thus, we apparently observe here a better BD productivity with less dispersed CuO nanoparticles (Figure C.2b). But we must remember that the catalytic step catalysed by the CuO nanoparticles is not the rate limiting step and other characterisation methods have already proven the CuO nanoparticles to be small (under 15 nm) and well dispersed throughout our different catalysts. As a result, Si/Cu does not appear, here, as a determining factor in the catalytic performance.

Table C.3: Relationship between XPS molecular ratios and BD productivity.

Sample	Si/Ta XPS	Si/Ta XPS/Theo	Si/Cu XPS	Si/Cu XPS/Theo	P_{BD} (g_{BD} g_{cat}^{-1} h^{-1})
AASG-4Ta4Cu	64	0.85	68	2.62	0.28
NH-Ac-4Ta4Cu	119	1.59	84	3.23	0.39
NH-32Et32Ac-2Ta4Cu-D24h	103	0.68	63	2.42	0.26

Theo=Theoretical ratio ; XPS= ratio determined by XPS

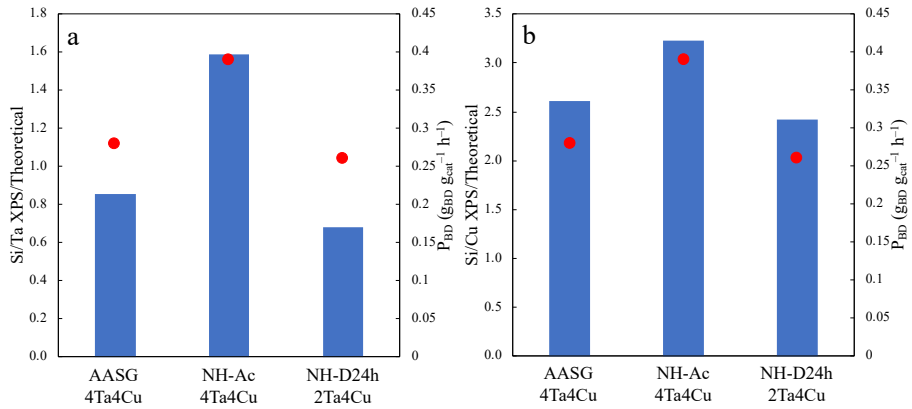

Figure C.2: Influence of the difference between the theoretical and experimental Si/Ta (a) and Si/Cu (b) ratios on the BD productivity. Blue histograms represent the atomic ratios and the red dots represent the BD productivity.

Besides catalytic data, the focus of this work was also brought on controlling certain catalysts properties through different synthesis protocols. Among them, we showed the influence of the Ta speciation on the acidity of the catalyst (Sections 4.3.1 and 6.3.1). TaOx clusters were shown to be less acidic than Ta imbedded in the silica matrix of spray-dried samples. However, different conclusions were drawn when comparing catalysts obtained via the ether and the acetamide elimination routes. Even though the acetamide elimination route yielded a catalyst with more dispersed Ta (i.e. more Si–O–Ta bonds), its Lewis acidity was lower than a similar catalyst obtained by the ether route, containing a combination of TaOx clusters and imbedded Ta, seemingly contradicting what was understood in the aerosol-assisted sol-gel. We first assumed that the higher electronegativity of Si compared to Ta resulted in a higher Lewis acidity for the Si–O–Ta bonds compared to Ta–O–Ta, which seemed true for spray-dried catalysts. But the samples obtained by non-hydrolytic sol-gel bring to light another determining factor potentially influencing the acidity: the configuration of Ta. The different solvents used during the synthesis protocols could influence the Ta coordination during the polycondensation process, for example forming different coordination spheres

around the element, giving rise to Ta integrated in the silica matrix (hence the Si–O–Ta detected among all catalysts) but with different configurations. Like shown on Scheme I.11, these different configurations possess different environments that should influence the acidity of the material. Thus, we hypothesize that the aerosol-assisted sol-gel technique and both non-hydrolytic sol-gel routes used yielded embedded Ta with different configurations, some better suited for the ETB reaction than others. In the future, more experiments such as CO-FTIR or EXAFS should be conducted on all samples, eventually leading to understand the exact configurations of embedded Ta in the different silica matrixes.

To conclude, our current best synthesis protocol, the non-hydrolytic sol-gel acetamide elimination route gave rise to a catalysts formulation possessing great open texture avoiding mass transfer limitations, ideal Lewis acidity brought by incorporated and well distributed Ta open sites active in the rate-limiting step of the reaction cascade and active redox sites in the form of dispersed small Cu nanoparticles. Here, the acetamide elimination route was applied in a one-step protocol with advanced control on the textural properties, active sites speciation and dispersion, allowing for an impressive 1,3-butadiene productivity.

8.2 Perspectives

In the future, the versatility of the aerosol-assisted sol-gel can be applied to synthesize more bifunctional pairs. Ta could be replaced with Nb, Zr and Y. Cu could be substituted with Zn, in a search for higher productivities (though, in this case, at the expense of the sustainability of the resource for catalyst manufacturing, and possibly at the expense of lower selectivity for BD). More recent literature tends to put Zr-Zn as the most effective combination to produce 1,3-butadiene and the aerosol-assisted sol-gel could easily be leveraged to obtain such formulations. Once the best formulation is selected and the loadings of the different metals optimized, the influence of the molecular precursors should be studied, namely on the degree of insertion in the silica matrix for acidic metals such as Zr. Although the rate-limiting step of the ETB reaction is catalysed by Lewis acidic metals such as Zr, the state and especially the dispersion of the other active site should be studied. The introduction of functionalized silica precursors like (3-mercaptopropyl)-trimethoxysilane (MPTMS) or (3-aminopropyl)-triethoxysilane (APTES) in the synthesis protocol could improve the dispersion of metal nanoparticles responsible for the acetaldehyde production and enhance the proximity between the different types of active sites in the bifunctional catalyst.

GENERAL CONCLUSION AND PERSPECTIVES

To deepen the improvement of an aerosol-made bifunctional catalyst, basic metal promoters could be added and studied. Metals such as Cs, Ce, Li, Na and K have already proven to enhance catalytic properties in some cases and could thus be interesting to add to the best formulation.

In terms of texture, we discussed the potential occurrence of internal diffusion limitations in our catalysts. The use of the different templating agents like Brij-58 or calibrated polymer beads should provide a range of catalysts with different porosity to better understand the relationship between pore size and catalytic performances, leading to an optimal synthesis protocol yielding a (hierarchically) porous catalyst with improved butadiene productivity.

In the non-hydrolytic sol-gel system, the optimal reaction conditions studied in section 5.3.4. should be applied to our current best catalyst to assess if similar improvements are observed. Ideally, the optimal formulation of bifunctional metals + basic promoter found via the aerosol-assisted so-gel could also be synthesized through the acetamide elimination route and studied. As the delayed addition protocol proved to be promising for optimizing catalytic performance with smaller loadings of active sites, deeper research should be conducted on the ideal timing for the first polycondensation between the ether precursors before the addition of the acetamide precursors.

More generally, the arguments discussed in section 1.4.6 about the availability and the sustainability of the different metals considered in the catalysts formulation should be weighted in regard to their catalytic performance, stability and reusability. For this, long term catalytic tests should be conducted with regeneration cycles or co-feeding of coke burning gases. Testing different formulations in those tests could highlight the ideal balance to achieve between scarcity of the active sites, BD productivity and catalyst life-time.

Finally, the testing of catalysts in aqueous ethanol would give more credibility to a potential future industrial application, as the majority of produced bioethanol still contain a fraction of water. The understanding of the influence of water in the catalytic process would be beneficial for the design of the material and potentially the choice of active elements.

CHAPTER 9: Appendix

9.1 Influence of the calcination temperature on catalytic performance for spray-dried catalysts

Table IX.1: Influence of the calcination temperature on the catalytic performance for 5Cu5Ta-SiO_2; Reaction Conditions: T°=325 °C; WHSV=1.1 h^{-1} TOS=1 h.

Calcination Temperature	Ethanol conversion (%)	Butadiene (%)		Acetaldehyde (%)		Ethylene (%)		Others (%)	
		Yield	Sel	Yield	Sel	Yield	Sel	Yield	Sel
500 °C	85,7	24,7	28.8	31.8	37.1	13.9	16.2	15.4	18.0
550 °C	52.2	7.3	14.0	26.0	49.8	7.8	15.0	11.1	21.2
600 °C	71.6	18.0	25.1	28.3	39.6	10.2	14.3	15.1	21.1
650 °C	60.5	16.7	27.6	26.6	44.1	5.6	9.3	11.5	19.1
700 °C	51.2	13.1	26.7	24.9	48.6	4.0	7.8	9.1	17.8
750 °C	57.9	16.5	28.4	27.5	47.4	2.5	4.4	11.5	19.8

9.2 Precursors molar amounts for all catalysts in this work

Table IX.2: Precursors molar amounts for the spray-dried catalysts.

Catalyst	TEOS	F127	$Ta(OEt)_5$	$AgNO_3$	$Cu(NO_3)_2 \cdot 2.5H_2O$
1Ag1Ta-SiO2	2.90E-02	1.54E-04	9.60E-05	1.70E-04	
2Ag1Ta-SiO2	2.88E-02	1.54E-04	9.67E-05	3.36E-04	
5Ag1Ta-SiO2	2.88E-02	1.55E-04	9.65E-05	8.54E-04	
1Ag2Ta-SiO2	2.90E-02	1.54E-04	1.97E-04	1.66E-04	
2Ag2Ta-SiO2	2.88E-02	1.53E-04	1.98E-04	3.27E-04	
5Ag2Ta-SiO2	2.88E-02	1.54E-04	2.04E-04	8.48E-04	
2Cu2Ta-SiO2	2.88E-02	1.53E-04	1.99E-04		5.63E-04
3Cu2Ta-SiO2	2.88E-02	1.54E-04	1.98E-04		8.47E-04
4Cu2Ta-SiO2	2.88E-02	1.55E-04	1.99E-04		1.15E-03
5Cu2Ta-SiO2	2.88E-02	1.55E-04	1.97E-04		1.43E-03
6Cu2Ta-SiO2	2.88E-02	1.54E-04	1.97E-04		1.75E-03
4Cu1Ta-SiO2	2.88E-02	1.56E-04	1.01E-04		1.14E-03
4Cu3Ta-SiO2	2.88E-02	1.55E-04	3.08E-04		1.14E-03
4Cu4Ta-SiO2	2.88E-02	1.53E-04	4.09E-04		1.14E-03

Table IX.3: Precursors molar amounts for ether-based catalysts.

Catalyst	$SiCl_4$	DIPE	$TaCl_5$	$Cu(AcAc)_2$
Et-2Ta2Cu	4.600	5.527	0.0651	0.137

Table IX.4: Precursors molar amounts for acetamide-based catalysts.

Catalyst	$Si(OAc)_4$	F127	$Ta(NMe_2)_5$	$Cu(AcAc)_2$
Ac-2Ta2Cu	7.099	3.630	0.0730	0.136
Ac-2Ta3Cu	7.106	3.639	0.0745	0.207
Ac-2Ta4Cu	7.101	3.638	0.0744	0.280
Ac-2Ta5Cu	7.102	3.632	0.0745	0.355
Ac-1Ta4Cu	7.093	3.631	0.0370	0.277
Ac-3Ta4Cu	7.095	3.641	0.111	0.279
Ac-4Ta4Cu	7.094	3.634	0.150	0.280

Table IX.5: Precursors molar amounts for catalysts synthesized via the direct mixing and delayed protocol.

Catalyst	$SiCl_4$	DIPE (1)	$TaCl_5$	$Si(OAc)_4$	$Ta(NMe_2)_5$	$Cu(AcAc)_2$	DIPE (2)
4Ac60Et-4Ta4Cu	3.00 E-02	5.83 E-02	-	2.02 E-03	4.63E-04	1.30E-03	-
6Ac58Et-4Ta4Cu	2.90 E-02	5.32 E-02	-	3.02 E-03	4.76E-04	1.30E-03	-
8Ac56Et-4Ta4Cu	2.81 E-02	4.91 E-02	-	4.02 E-03	4.66E-04	1.32E-03	-
56Et8Ac-4Ta4Cu-D8h	2.80 E-02	4.92 E-02	5.58 E-05	4.05 E-03	4.09E-04	1.30E-03	-
56Et8Ac-1Ta4Cu-D24h	3.52 E-02	3.54 E-02	1.95 E-05	5.03 E-03	1.22E-04	1.43E-03	2.38 E-02
56Et8Ac-2Ta4Cu-D24h	3.52 E-02	3.54 E-02	1.95 E-05	5.03 E-03	2.57E-04	1.42E-03	2.37 E-02
56Et8Ac-4*Ta4Cu-D24h	3.52 E-02	3.53 E-02	1.12 E-05	5.03 E-03	6.48E-05	1.42E-03	2.38 E-02
48Et16Ac-1Ta4Cu-D24h	3.02 E-02	3.02 E-02	8.37 E-06	1.01 E-02	1.30E-04	1.42E-03	8.62 E-03
48Et16Ac-2Ta4Cu-D24h	3.02 E-02	3.02 E-02	1.67 E-05	1.01 E-02	2.47E-04	1.43E-03	8.66 E-03
48Et16Ac-4*Ta4Cu-D24h	3.02 E-02	3.03 E-02	1.40 E-05	1.01 E-02	1.25E-04	1.44E-03	8.65 E-03
40Et24Ac-1Ta4Cu-D24h	2.52 E-02	2.53 E-02	1.40 E-05	1.51 E-02	1.22E-04	1.44E-03	-
40Et24Ac-2Ta4Cu-D24h	2.52 E-02	2.52 E-02	1.95 E-05	1.51 E-02	2.49E-04	1.43E-03	-
40Et24Ac-4*Ta4Cu-D24h	2.52 E-02	2.52 E-02	2.79 E-05	1.52 E-02	1.92E-04	1.43E-03	-
32Et32Ac-1Ta4Cu-D24h	2.02 E-02	2.01 E-02	1.40 E-05	2.01 E-02	1.22E-04	1.43E-03	-
32Et32Ac-2Ta4Cu-D24h	2.02 E-02	2.02 E-02	2.23 E-05	2.01 E-02	2.47E-04	1.44E-03	-
32Et32Ac-4*Ta4Cu-D24h	2.02 E-02	2.01 E-02	3.63 E-05	2.01 E-02	2.57E-04	1.44E-03	-

9.3 Thermogravimetry analysis combined with mass spectrometry

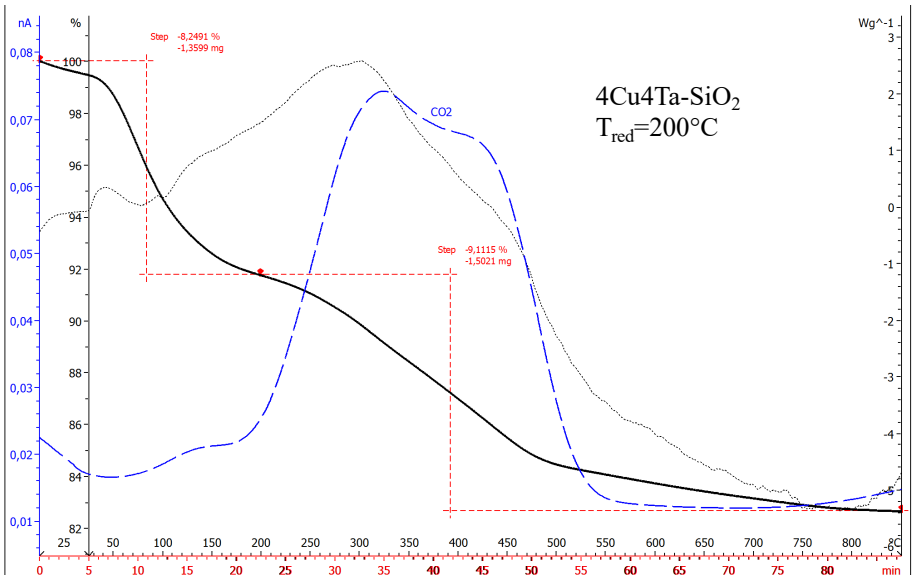

Figure IX.1: TGA-MS analysis of spent 4Cu4Ta-SiO_2 after a catalytic run with pre-reduction under hydrogen at 350 °C.

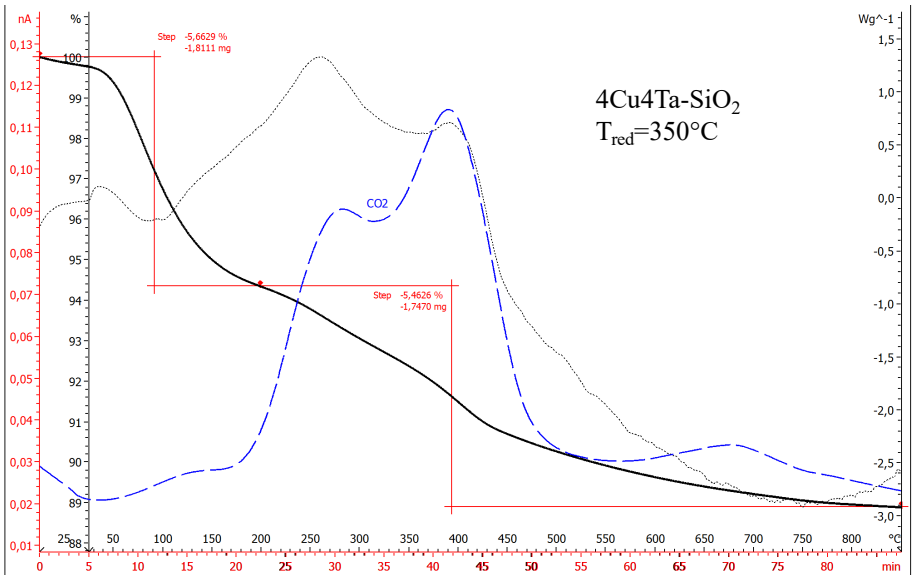

Figure IX.2: TGA-MS analysis of spent 4Cu4Ta-SiO_2 after a catalytic run with pre-reduction under hydrogen at 200 °C.

CHAPTER 10: References

1 Research, D. B. M. *Global 1,3-Butadiene Market - Industry Trends and Forecast to 2029*, <https://www.databridgemarketresearch.com/reports/global-1-3-butadiene-market> (Oct 2022).

2 OECD, Food & Nations, A. O. o. t. U. *OECD-FAO Agricultural Outlook 2023-2032*. (2023).

3 Cespi, D., Passarini, F., Vassura, I. & Cavani, F. Butadiene from biomass, a life cycle perspective to address sustainability in the chemical industry. *Green Chem.* **18**, 1625-1638 (2016).

4 Kyriienko, P., Larina, O., Soloviev, S. & Orlyk, S. Catalytic Conversion of Ethanol Into 1, 3-Butadiene: Achievements and Prospects: A Review. *Theoretical and Experimental Chemistry*, 1-30 (2020).

5 Makshina, E. V. *et al.* Review of old chemistry and new catalytic advances in the on-purpose synthesis of butadiene. *Chem. Soc. Rev.* **43**, 7917-7953 (2014).

6 Pomalaza, G., Ponton, P. A., Capron, M. & Dumeignil, F. Ethanol-to-butadiene: the reaction and its catalysts. *Catalysis Science & Technology* **10**, 4860-4911 (2020).

7 Dochain, D. D., Stýskalík, A. & Debecker, D. P. Ag-and Cu-promoted mesoporous Ta-SiO2 catalysts prepared by non-hydrolytic sol-gel for the conversion of ethanol to butadiene. *Catalysts* **9**, 920 (2019).

8 Makshina, E. V. *et al.* Review of old chemistry and new catalytic advances in the on-purpose synthesis of butadiene. *Chem. Soc. Rev.* **43**, 7917-7953 (2014).

9 Plotkin, J. S. The continuing quest for butadiene. (2016).

10 Dahlmann, M., Grub, J. & Löser, u. E. Butadiene. *Ullmann's Encyclopedia of Industrial Chemistry; Wiley-VCH Verlag GmbH & Co. KGaA: Weinheim, Germany* **100**, 1-24 (2011).

11 Grub, J. & Löser, E. Butadiene. *Ullmann's Encyclopedia of Industrial Chemistry*, 1-17 (2005).

12 Sun, H. & Wristers, J. Butadiene. *Kirk-Othmer Encyclopedia of Chemical Technology* (2000).

13 Threadingham, D. J. *et al.* Synthetic Rubbers, Producers and World Market of. *Biopolymers Online: Biology• Chemistry• Biotechnology• Applications* **2** (2005).

14 Morton, M. History of synthetic rubber. *Journal of Macromolecular Science—Chemistry* **15**, 1289-1302 (1981).

15 Egloff, G. & Hulla, G. Errata-Conversion of Hydrocarbons into Butadiene (V. 35, I. 2 p. 283-287). *Chemical Reviews* **36**, 144-144 (1945).

16 Nef, J. Dissociationsvorgänge bei den einatomigen alkoholen, aethern und salzen. *Justus Liebigs Annalen der Chemie* **318**, 137-230 (1901).

17 Ostromislensky, I. A process for making butadiene by condensing ethanol with acetaldehyde over an oxide catalyst at 360 to 440 C. *Journal of Russian Physical and Chemical Society* **47**, 1885 (1915).

18 Corson, B. B., Jones, H. E., Welling, C. E., Hinckley, J. A. & Stahly, E. E. Butadiene from Ethyl Alcohol. Catalysis in the One-and Two-Stop Processes. *Ind. Eng. Chem.* **42**, 359-373 (1950).

19 Kampmeyer, P. & Stahly, E. Butadiene from ethyl alcohol: improved production processes. *Ind. Eng. Chem.* **41**, 550-555 (1949).

20 Whitlock, M., Haddad, G. & Stahly, E. System for Rapid Evaluation of Catalysts for Production of Butadiene from Ethanol. *Analytical Chemistry* **19**, 767-770 (1947).

21 Bhattacharyya, S. & Avasthi, B. One-step catalytic conversion of ethanol to butadiene in a fluidized bed. *Industrial & Engineering Chemistry Process Design and Development* **2**, 45-51 (1963).

22 Bhattacharyya, S. & Ganguly, N. One-step catalytic conversion of ethanol to butadiene in the fixed bed. II BINARY-AND TERNARY-OXIDE CATALYSTS. *Journal of Applied Chemistry* **12**, 105-110 (1962).

23 Bhattacharyya, S. & Sanyal, S. Kinetic study on the mechanism of the catalytic conversion of ethanol to butadiene. *Journal of Catalysis* **7**, 152-158 (1967).

24 Kvisle, S., Aguero, A. & Sneeden, R. Transformation of ethanol into 1, 3-butadiene over magnesium oxide/silica catalysts. *Applied catalysis* **43**, 117-131 (1988).

25 Niiyama, H., Morii, S. & Echigoya, E. Butadiene formation from ethanol over silica-magnesia catalysts. *Bulletin of the chemical Society of Japan* **45**, 655-659 (1972).

26 Kitayama, Y. & Michishita, A. Catalytic activity of fibrous clay mineral sepiolite for butadiene formation from ethanol. *Journal of the Chemical Society, Chemical Communications*, 401-402 (1981).

27 Angelici, C., Weckhuysen, B. M. & Bruijnincx, P. C. A. Chemocatalytic Conversion of Ethanol into Butadiene and Other Bulk Chemicals. *ChemSusChem* **6**, 1595-1614 (2013).

28 Jones, M. D. *et al.* Investigations into the conversion of ethanol into 1, 3-butadiene. *Catalysis Science & Technology* **1**, 267-272 (2011).

29 Tian, P., Wei, Y., Ye, M. & Liu, Z. Methanol to olefins (MTO): from fundamentals to commercialization. *ACS Catal.* **5**, 1922-1938 (2015).

30 DeRosa, S. E. & Allen, D. T. Impact of natural gas and natural gas liquids supplies on the United States chemical manufacturing industry: production cost effects and identification of bottleneck intermediates. *ACS Sustainable Chem. Eng.* **3**, 451-459 (2015).

31 White, W. C. Butadiene production process overview. *Chem. Biol. Interact.* **166**, 10-14 (2007).

32 Ren, T., Patel, M. & Blok, K. Olefins from conventional and heavy feedstocks: Energy use in steam cracking and alternative processes. *Energy* **31**, 425-451 (2006).

33 Haribal, V. P., Chen, Y., Neal, L. & Li, F. Intensification of ethylene production from naphtha via a redox oxy-cracking scheme: Process simulations and analysis. *Engineering* **4**, 714-721 (2018).

34 Al-Douri, A., Sengupta, D. & El-Halwagi, M. M. Shale gas monetization – A review of downstream processing to chemicals and fuels. *Journal of Natural Gas Science and Engineering* **45**, 436-455 (2017).

35 Wells, G. M. *Handbook of petrochemicals and processes*. (Routledge, 2018).

36 Adiya, Z. I. S., Dupont, V. & Mahmud, T. Steam reforming of shale gas in a packed bed reactor with and without chemical looping using nickel based oxygen carrier. *international journal of hydrogen energy* **43**, 6904-6917 (2018).

37 Pring, M. Condensate Tank Oil and Gas Activities. *Final Report* (2012).

38 Weissermel, K. & Arpe, H.-J. *Industrial organic chemistry*. (John Wiley & Sons, 2008).

39 Ren, T., Patel, M. K. & Blok, K. Steam cracking and methane to olefins: Energy use, CO2 emissions and production costs. *Energy* **33**, 817-833 (2008).

40 Gielen, D., Moriguchi, Y. & Yagita, H. CO2 emission reduction for Japanese petrochemicals. *Journal of Cleaner Production* **10**, 589-604 (2002).

41 IPPC. Climate Change 2021: The Physical Science Basis. Contribution of Working Group I to the Sixth Assessment Report of the Intergovernmental Panel on Climate Change. (2021).

42 Duan, H., Yamada, Y. & Sato, S. Future prospect of the production of 1, 3-butadiene from butanediols. *Chemistry Letters* **45**, 1036-1047 (2016).

43 Ghiaci, P., Norbeck, J. & Larsson, C. 2-Butanol and butanone production in Saccharomyces cerevisiae through combination of a B12 dependent dehydratase and a secondary alcohol dehydrogenase using a TEV-based expression system. *PLoS One* **9**, e102774 (2014).

44 Yim, H. *et al.* Metabolic engineering of Escherichia coli for direct production of 1, 4-butanediol. *Nature chemical biology* **7**, 445-452 (2011).

45 Bruijnincx, P. C. & Weckhuysen, B. M. Shale gas revolution: an opportunity for the production of biobased chemicals? *Angewandte Chemie International Edition* **52**, 11980-11987 (2013).

46 Bailey, M. P. The future of butadiene. *Chemical Engineering* **121**, 19 (2014).

47 Murakami, S., Harada, T. & Tai, A. The Enantioface-differentiating Hydrogenation of the C= O Double Bond with Asymmetrically Modified Raney Nickel. XXXIII. The Preparation of (R)-and (S)-1, 3-Butanediol from 4-Hydroxy-2-butanone. *Bulletin of the Chemical Society of Japan* **53**, 1356-1360 (1980).

48 Matsumura, Y., Matsuda, A., Yamada, Y. & Sato, S. Selective production of 1, 3-butadiene from 1, 3-butanediol over Y2Zr2O7 catalyst. *Bulletin of the Chemical Society of Japan* **94**, 1651-1658 (2021).

49 Lee, J. H. & Hong, S. B. Dehydration of 1, 3-butanediol to butadiene over medium-pore zeolites: Another example of reaction intermediate

shape selectivity. *Applied Catalysis B: Environmental* **280**, 119446 (2021).

50 Jing, F. *et al.* Direct dehydration of 1, 3-butanediol into butadiene over aluminosilicate catalysts. *Catalysis Science & Technology* **6**, 5830-5840 (2016).

51 Rodríguez, A. C., Sad, M. E. & Padró, C. L. Acid site requirement and reaction pathway for selective bio-butadiene synthesis by 1, 3-butanediol dehydration. *Applied Catalysis A: General*, 119349 (2023).

52 Fang, L., Jing, F., Lu, J., Hu, B. & Pera-Titus, M. Nano-flowered Ce@ MOR hybrids with modulated acid properties for the vapor-phase dehydration of 1, 3-butanediol into butadiene. *Green Chem.* **19**, 4610-4621 (2017).

53 Alegre-Requena, J. V. *et al.* Experimental and computational studies of the production of 1, 3-butadiene from 2, 3-butanediol using SiO2-supported H3PO4 derivatives. *Chemical Engineering Journal* **466**, 143346 (2023).

54 Yang, S. *et al.* Metabolic engineering of Zymomonas mobilis for 2, 3-butanediol production from lignocellulosic biomass sugars. *Biotechnology for biofuels* **9**, 1-15 (2016).

55 Yang, Z. & Zhang, Z. Recent advances on production of 2, 3-butanediol using engineered microbes. *Biotechnology advances* **37**, 569-578 (2019).

56 Tsukamoto, D., Sakami, S., Ito, M., Yamada, K. & Yonehara, T. Production of bio-based 1, 3-butadiene by highly selective dehydration of 2, 3-butanediol over SiO2-supported cesium dihydrogen phosphate catalyst. *Chemistry Letters* **45**, 831-833 (2016).

57 Kim, W. *et al.* 2, 3-Butanediol dehydration catalyzed by silica-supported alkali phosphates. *Applied Catalysis A: General* **570**, 148-163 (2019).

58 Duan, H., Yamada, Y. & Sato, S. Efficient production of 1, 3-butadiene in the catalytic dehydration of 2, 3-butanediol. *Applied Catalysis A: General* **491**, 163-169 (2015).

59 Nakazono, K., Takahashi, R., Yamada, Y. & Sato, S. Dehydration of 2, 3-butanediol to produce 1, 3-butadiene over Sc2O3 catalyst prepared through hydrothermal aging. *Molecular Catalysis* **516**, 111996 (2021).

60 Liu, X. *et al.* One-Step Production of 1, 3-Butadiene from 2, 3-Butanediol Dehydration. *Chemistry–A European Journal* **22**, 12290-12294 (2016).

61 Song, D., Yoon, Y.-G. & Lee, C.-J. Techno-economic evaluation of the 2, 3-butanediol dehydration process using a hydroxyapatite-alumina catalyst. *Korean Journal of Chemical Engineering* **35**, 2348-2354 (2018).

62 Chaudhary, L., Pradhan, P., Soni, N., Singh, P. & Tiwari, A. Algae as a feedstock for bioethanol production: new entrance in biofuel world. *International Journal of ChemTech Research* **6**, 1381-1389 (2014).

63 Muktham, R., K. Bhargava, S., Bankupalli, S. & S. Ball, A. A Review on 1st and 2nd Generation Bioethanol Production-Recent Progress. *Journal of Sustainable Bioenergy Systems* **06**, 72-92 (2016).

64 Gérardy, R. *et al.* Sustaining the Transition from a petrobased to a Biobased Chemical Industry with Flow Chemistry. *Topics in Current Chemistry* **377**, 1 (2019).

65 Gallezot, P. Conversion of biomass to selected chemical products. *Chem. Soc. Rev.* **41**, 1538-1558 (2012).

66 Hidzir, N. S., Som, A. & Abdullah, Z. in *International conference on global sustainability and chemical engineering (ICGSE).* 1-6.

67 Roozbehani, B., Moqadam, S. I., Mirdrikvand, M. & Roshan, A. C. Modeling direct ethylene hydration over zirconium tungsten catalyst: Fundamental of ethanol production using the biggest global ethylene feeding pipeline in Iran. *Energy and environment research* **2**, 28 (2012).

68 Huang, H., Qureshi, N., Chen, M.-H., Liu, W. & Singh, V. Ethanol production from food waste at high solids content with vacuum recovery technology. *Journal of agricultural and food chemistry* **63**, 2760-2766 (2015).

69 Baeyens, J. *et al.* Challenges and opportunities in improving the production of bio-ethanol. *Progress in Energy and Combustion Science* **47**, 60-88 (2015).

70 Lau, M. W. & Dale, B. E. Cellulosic ethanol production from AFEX-treated corn stover using Saccharomyces cerevisiae 424A (LNH-ST). *Proceedings of the National Academy of Sciences* **106**, 1368-1373 (2009).

71 Kazi, F. K. *et al.* Techno-economic comparison of process technologies for biochemical ethanol production from corn stover. *Fuel* **89**, S20-S28 (2010).

72 Saha, B. C., Iten, L. B., Cotta, M. A. & Wu, Y. V. Dilute acid pretreatment, enzymatic saccharification and fermentation of wheat straw to ethanol. *Process biochemistry* **40**, 3693-3700 (2005).

73 Binod, P. *et al.* Bioethanol production from rice straw: an overview. *Bioresource technology* **101**, 4767-4774 (2010).

74 Bozell, J. J. & Petersen, G. R. Technology development for the production of biobased products from biorefinery carbohydrates—the US Department of Energy's "Top 10" revisited. *Green Chem.* **12**, 539-554 (2010).

75 Abdulrazzaq, H. T. & Schwartz, T. J. Catalytic conversion of ethanol to commodity and specialty chemicals. *Ethanol*, 3-24 (2019).

76 Styskalik, A. *et al.* Non-hydrolytic sol–gel route to a family of hybrid mesoporous aluminosilicate ethanol dehydration catalysts. *J Mater Sci*, 1-18 (2021).

77 Zhang, M. & Yu, Y. Dehydration of Ethanol to Ethylene. *Ind. Eng. Chem. Res.* **52**, 9505-9514 (2013).

78 Wu, X. *et al.* Catalytic upgrading of ethanol to n-butanol: progress in catalyst development. *ChemSusChem* **11**, 71-85 (2018).

79 Dumeignil, F. *et al.* Biomass-derived platform molecules upgrading through catalytic processes: yielding chemicals and fuels. *Journal of the Japan Petroleum Institute* **58**, 257-273 (2015).

80 Sun, J. & Wang, Y. Recent Advances in Catalytic Conversion of Ethanol to Chemicals. *ACS Catal.* **4**, 1078-1090 (2014).

81 Kim, T.-W. *et al.* Butadiene production from bioethanol and acetaldehyde over tantalum oxide-supported spherical silica catalysts for circulating fluidized bed. *Chemical Engineering Journal* **278**, 217-223 (2015).

82 Pomalaza, G. *et al.* Recent Breakthroughs in the Conversion of Ethanol to Butadiene. *Catalysts* **6**, 203 (2016).

83 Shylesh, S. *et al.* From Sugars to Wheels: The Conversion of Ethanol to 1,3-Butadiene over Metal-Promoted Magnesia-Silicate Catalysts. *ChemSusChem* **9**, 1462-1472 (2016).

84 Sushkevich, V. L. & Ivanova, I. I. Mechanistic study of ethanol conversion into butadiene over silver promoted zirconia catalysts. *Applied Catalysis B: Environmental* **215**, 36-49 (2017).

85 Müller, P. *et al.* Mechanistic Study on the Lewis Acid Catalyzed Synthesis of 1,3-Butadiene over Ta-BEA Using Modulated Operando DRIFTS-MS. *ACS Catal.* **6**, 6823-6832 (2016).

86 Miyake, N., Brezicki, G. & Davis, R. J. Cascade reaction of ethanol to butadiene over multifunctional silica-supported Ag and ZrO2 Catalysts. *ACS Sustainable Chem. Eng.* **10**, 1020-1035 (2022).

87 Gao, M., Liu, Z., Zhang, M. & Tong, L. Study on the Mechanism of Butadiene Formation from Ethanol. *Catal Lett* **144**, 2071-2079 (2014).

88 Ezinkwo, G. O., Tretyakov, V. P., Aliyu, A. & Ilolov, A. M. Fundamental Issues of Catalytic Conversion of Bio-Ethanol into Butadiene. *ChemBioEng Reviews* **1**, 194-203 (2014).

89 Quattlebaum, W., Toussaint, W. & Dunn, J. Deoxygenation of certain aldehydes and ketones: preparation of butadiene and styrene1. *Journal of the American Chemical Society* **69**, 593-599 (1947).

90 Toussaint, W., Dunn, J. & Jachson, D. Production of butadiene from alcohol. *Ind. Eng. Chem.* **39**, 120-125 (1947).

91 Kagan, M., Lyubarskii, G. & Podurovskaya, O. Mechanism of the catalytic synthesis of bivinyl from ethyl alcohol. *Izv. Akad. Nauk SSSR, Ser. Khim*, 173-181 (1947).

92 Gorin, Y. A. Catalytic conversions of alcohols into bivinyl hydrocarbons. XV. General laws of formation of diethylenic hydrocarbons with a conjugate bond system. *Zhurnal Obshchei Khimii* **19**, 877-883 (1949).

93 Kyriienko, P. I., Larina, O. V., Balakin, D. Y., Soloviev, S. O. & Orlyk, S. M. Influence of Copper and Silver on Catalytic Performance of MgO–SiO2 System for 1, 3-Butadiene Production from Aqueous Ethanol. *Catal Lett*, 1-10 (2021).

94 Makshina, E., Janssens, W., Sels, B. & Jacobs, P. Catalytic study of the conversion of ethanol into 1, 3-butadiene. *Catalysis today* **198**, 338-344 (2012).

95 Sushkevich, V. L., Ivanova, I. I. & Taarning, E. Mechanistic Study of Ethanol Dehydrogenation over Silica-Supported Silver. *ChemCatChem* **5**, 2367-2373 (2013).

96 Wang, Z.-T. *et al.* Surface structure dependence of the dry dehydrogenation of alcohols on Cu (111) and Cu (110). *The Journal of Physical Chemistry C* **121**, 12800-12806 (2017).

97 Kumar, A. Ethanol decomposition and dehydrogenation for hydrogen production: a review of heterogeneous catalysts. *Ind. Eng. Chem. Res.* **60**, 16561-16576 (2021).

98 Larina, O. *et al.* Influence of Acid–Base Characteristics of Hierarchical Cu/Zr-MTW Zeolites on their Catalytic Properties in 1, 3-Butadiene Production from Ethanol–Water Mixtures. *Theoretical and Experimental Chemistry* **57**, 343-350 (2021).

99 Akhade, S. A. *et al.* Influence of Ag metal dispersion on the thermal conversion of ethanol to butadiene over Ag-ZrO2/SiO2 catalysts. *Journal of Catalysis* **386**, 30-38 (2020).

100 Giannakakis, G. *et al.* NiAu single atom alloys for the non-oxidative dehydrogenation of ethanol to acetaldehyde and hydrogen. *Topics in Catalysis* **61**, 475-486 (2018).

101 Pampararo, G. *et al.* Ethanol dehydrogenation to acetaldehyde with mesoporous Cu-SiO2 catalysts prepared by aerosol-assisted sol–gel. *Chemical Engineering Journal* **465**, 142715 (2023).

102 Pang, J. *et al.* Advances in catalytic dehydrogenation of ethanol to acetaldehyde. *Green Chem.* **23**, 7902-7916 (2021).

103 Da Ros, S. *et al.* Microkinetic analysis of ethanol to 1, 3-butadiene reactions over MgO-SiO2 catalysts based on characterization of experimental fluctuations. *Chemical Engineering Journal* **308**, 988-1000 (2017).

104 Larina, O., Kyriienko, P. & Soloviev, S. Effect of lanthanum in Zn-La (-Zr)-Si oxide compositions on their activity in the conversion of ethanol into 1, 3-butadiene. *Theoretical and Experimental Chemistry* **52**, 51-56 (2016).

105 Sushkevich, V. L., Ivanova, I. I., Ordomsky, V. V. & Taarning, E. Design of a Metal-Promoted Oxide Catalyst for the Selective Synthesis of Butadiene from Ethanol. *ChemSusChem* **7**, 2527-2536 (2014).

106 Kyriienko, P. I., Larina, O. V., Soloviev, S. O., Orlyk, S. M. & Dzwigaj, S. High selectivity of TaSiBEA zeolite catalysts in 1,3-butadiene production from ethanol and acetaldehyde mixture. *Catalysis Communications* **77**, 123-126 (2016).

107 Sushkevich, V. L. & Ivanova, I. I. Ag-Promoted ZrBEA Zeolites Obtained by Post-Synthetic Modification for Conversion of Ethanol to Butadiene. *ChemSusChem* **9**, 2216-2225 (2016).

108 Wang, K. *et al.* Hierarchical nano-sized ZnZr-Silicalite-1 multifunctional catalyst for selective conversion of ethanol to butadiene. *Applied Catalysis B: Environmental* **301**, 120822 (2022).

109 Wang, K. *et al.* Probing the promotional roles of lanthanum in physicochemical properties and performance of ZnZr/Si-beta catalyst

for direct conversion of aqueous ethanol to butadiene. *Catalysis Today* **411**, 113800 (2023).

110 Dang, S.-X. *et al.* Reaction mechanism of one-step conversion of ethanol to 1, 3-butadiene over Zn-Y/BEA and superior catalysts screening. *Chinese Journal of Chemical Physics* **35**, 600-610 (2022).

111 De Baerdemaeker, T. *et al.* Bimetallic Zn and Hf on silica catalysts for the conversion of ethanol to 1, 3-butadiene. *ACS Catal.* **5**, 3393-3397 (2015).

112 Patil, P. T., Liu, D., Liu, Y., Chang, J. & Borgna, A. Improving 1, 3-butadiene yield by Cs promotion in ethanol conversion. *Applied Catalysis A: General* **543**, 67-74 (2017).

113 Wang, K. *et al.* One-pot hydrothermal synthesis of multifunctional ZnZrTUD-1 catalysts for highly efficient direct synthesis of butadiene from ethanol. *ACS Sustainable Chem. Eng.* **9**, 10569-10578 (2021).

114 Kyriienko, P. I. *et al.* Ethanol Conversion into 1,3-Butadiene by the Lebedev Method over MTaSiBEA Zeolites (M = Ag, Cu, Zn). *ACS Sustainable Chem. Eng.* **5**, 2075-2083 (2017).

115 Ahn, C.-I. *et al.* Ethanol conversion into 1, 3-butadiene over ZnZr mixed oxide catalysts supported on ordered mesoporous materials. *Fuel Processing Technology* **200**, 106317 (2020).

116 Cheong, J. L. *et al.* Highly active and selective Zr/MCF catalyst for production of 1, 3-butadiene from ethanol in a dual fixed bed reactor system. *ACS Sustainable Chem. Eng.* **4**, 4887-4894 (2016).

117 Da Ros, S. *et al.* Ethanol to 1, 3-butadiene conversion by using ZrZn-containing MgO/SiO2 systems prepared by co-precipitation and effect of catalyst acidity modification. *ChemCatChem* **8**, 2376-2386 (2016).

118 Kurmach, M. M. *et al.* Hierarchical Zr-MTW Zeolites Doped with Copper as Catalysts of Ethanol Conversion into 1, 3-Butadiene. *ChemistrySelect* **3**, 8539-8546 (2018).

119 Larina, O. V. *et al.* Design of Effective Catalysts Based on ZnLaZrSi Oxide Systems for Obtaining 1, 3-Butadiene from Aqueous Ethanol. *ACS Sustainable Chem. Eng.* **8**, 16600-16611 (2020).

120 Pomalaza, G., Vofo, G., Capron, M. & Dumeignil, F. ZnTa-TUD-1 as an easily prepared, highly efficient catalyst for the selective conversion of ethanol to 1, 3-butadiene. *Green Chem.* **20**, 3203-3209 (2018).

121 Sushkevich, V. L., Ivanova, I. I. & Taarning, E. Ethanol conversion into butadiene over Zr-containing molecular sieves doped with silver. *Green Chem.* **17**, 2552-2559 (2015).

122 Yan, T. *et al.* Mechanistic Insights into One-Step Catalytic Conversion of Ethanol to Butadiene over Bifunctional Zn–Y/Beta Zeolite. *ACS Catal.* **8**, 2760-2773 (2018).

123 Sushkevich, V. L., Palagin, D. & Ivanova, I. I. With open arms: open sites of ZrBEA zeolite facilitate selective synthesis of butadiene from ethanol. *ACS Catal.* **5**, 4833-4836 (2015).

124 Taifan, W. E., Bučko, T. & Baltrusaitis, J. Catalytic conversion of ethanol to 1, 3-butadiene on MgO: A comprehensive mechanism elucidation using DFT calculations. *Journal of Catalysis* **346**, 78-91 (2017).

125 Lewandowski, M. *et al.* Investigations into the conversion of ethanol to 1, 3-butadiene using MgO: SiO2 supported catalysts. *Catalysis Communications* **49**, 25-28 (2014).

126 Dochain, D. D. *et al.* Non-hydrolytic Sol–Gel Routes to Bifunctional Cu–Ta–SiO2 Catalysts for the Upgrading of Ethanol to Butadiene. *Chemistry of Materials* **35**, 7113-7124 (2023).

127 Angelici, C. *et al.* Ex situ and operando studies on the role of copper in Cu-promoted SiO2–MgO catalysts for the Lebedev ethanol-to-butadiene process. *ACS Catal.* **5**, 6005-6015 (2015).

128 Dussol, D., Cadran, N., Laloue, N., Renaudot, L. & Schweitzer, J.-M. New insights of butadiene production from ethanol: Elucidation of concurrent reaction pathways and kinetic study. *Chemical Engineering Journal* **391**, 123586 (2020).

129 Larina, O. *et al.* Influence of Modification of Zn-Mg (Zr) Si Oxide Systems by Sodium and Potassium on their Catalytic Properties in the Process of Obtaining 1, 3-Butadiene from Ethanol. *Theoretical and Experimental Chemistry* **57**, 443-450 (2022).

130 Weisz, P. & Prater, C. in *Advances in catalysis* Vol. 6 143-196 (Elsevier, 1954).

131 Jones, H., Stahly, E. & Corson, B. Butadiene from ethanol. Reaction mechanism. *Journal of the American Chemical Society* **71**, 1822-1828 (1949).

132 Ushikubo, T. & Wada, K. Catalytic properties of hydrated tantalum oxide. *Applied catalysis* **67**, 25-38 (1990).

133 Da Ros, S. *et al.* Modelling the effects of reaction temperature and flow rate on the conversion of ethanol to 1, 3-butadiene. *Applied Catalysis A: General* **530**, 37-47 (2017).

134 Dai, H. *et al.* Enhanced Performance and Stability of a Trimetallic CuZnY/SiBEA Catalyst in Ethanol to Butadiene Reaction by Introducing Copper to Optimize Acid/Base Ratio. *Catalysts* **12**, 1147 (2022).

135 Ochoa, J. V. *et al.* An analysis of the chemical, physical and reactivity features of MgO–SiO2 catalysts for butadiene synthesis with the Lebedev process. *Green Chem.* **18**, 1653-1663 (2016).

136 Chieregato, A. *et al.* On the chemistry of ethanol on basic oxides: revising mechanisms and intermediates in the Lebedev and Guerbet reactions. *ChemSusChem* **8**, 377-388 (2015).

137 González, G. C. *et al.* Ethanol conversion into 1, 3-butadiene over a mixed Hf-Zn catalyst: Effect of reaction conditions and water content in ethanol. *Fuel Processing Technology* **193**, 263-272 (2019).

138 Yan, T. *et al.* On the deactivation mechanism of zeolite catalyst in ethanol to butadiene conversion. *Journal of Catalysis* **367**, 7-15 (2018).

139 González, G. C. *et al.* Ethanol conversion into 1, 3-butadiene over a mixed Hf-Zn catalyst: A study of the reaction pathway and catalyst deactivation. *Applied Catalysis A: General* **570**, 96-106 (2019).

140 Zhao, Y. *et al.* New ZnCe catalyst encapsulated in SBA-15 in the production of 1, 3-butadiene from ethanol. *Chinese Chemical Letters* **31**, 535-538 (2020).

141 Dai, W. *et al.* Zeolite structural confinement effects enhance one-pot catalytic conversion of ethanol to butadiene. *ACS Catal.* **7**, 3703-3706 (2017).

142 Corson, B., Stahly, E., Jones, H. & Bishop, H. Butadiene from ethyl alcohol. *Ind. Eng. Chem.* **41**, 1012-1017 (1949).

143 Tielens, F., Shishido, T. & Dzwigaj, S. What do tantalum framework sites look like in zeolites? A combined theoretical and experimental investigation. *The Journal of Physical Chemistry C* **114**, 9923-9930 (2010).

144 Ob-eye, J., Praserthdam, P. & Jongsomjit, B. Dehydrogenation of ethanol to acetaldehyde over different metals supported on carbon catalysts. *Catalysts* **9**, 66 (2019).

145 Huang, Y. *et al.* The catalytic dehydrogenation of ethanol by heterogeneous catalysts. *Catalysis Science & Technology* **11**, 1652-1664 (2021).

146 Conesa, J., Morales, M., López-Olmos, C., Rodríguez-Ramos, I. & Guerrero-Ruiz, A. Comparative study of Cu, Ag and Ag-Cu catalysts over graphite in the ethanol dehydrogenation reaction: Catalytic activity, deactivation and regeneration. *Applied Catalysis A: General* **576**, 54-64 (2019).

147 Zhang, M., Guan, X., Zhuang, J. & Yu, Y. Insights into the mechanism of ethanol conversion into 1, 3-butadiene on Zr-β zeolite. *Applied Surface Science* **579**, 152212 (2022).

148 Sushkevich, V. L., Vimont, A., Travert, A. & Ivanova, I. I. Spectroscopic evidence for open and closed Lewis acid sites in ZrBEA zeolites. *The Journal of Physical Chemistry C* **119**, 17633-17639 (2015).

149 Pomalaza, G., Simon, P., Addad, A., Capron, M. & Dumeignil, F. Properties and activity of Zn–Ta-TUD-1 in the Lebedev process. *Green Chem.* **22**, 2558-2574 (2020).

150 Wang, J., Okumura, K., Jaenicke, S. & Chuah, G.-K. Post-synthesized zirconium-containing Beta zeolite in Meerwein–Ponndorf–Verley reduction: Pros and cons. *Applied Catalysis A: General* **493**, 112-120 (2015).

151 Tolborg, S. *et al.* Incorporation of tin affects crystallization, morphology, and crystal composition of Sn-Beta. *Journal of Materials Chemistry A* **2**, 20252-20262 (2014).

152 Kyriienko, P. I. *et al.* The effect of lanthanum in Cu/La (-Zr)-Si oxide catalysts for aqueous ethanol conversion into 1, 3-butadiene. *Molecular Catalysis* **518**, 112096 (2022).

153 Taifan, W. E. *et al.* Operando structure determination of Cu and Zn on supported MgO/SiO2 catalysts during ethanol conversion to 1, 3-butadiene. *ACS Catal.* **9**, 269-285 (2019).

154 Debecker, D. P. *et al.* Vol. 9 4936-4940 (ACS Publications, 2021).

155 EuChemS. *Element Scarcity - EuChemS Periodic Table*, <https://www.euchems.eu/euchems-periodic-table> (2023).

156 Debecker, D. P. Innovative Sol-Gel Routes for the Bottom-Up Preparation of Heterogeneous Catalysts. *The Chemical Record* **18**, 662-675 (2018).

157 Livage, J. Sol–gel synthesis of heterogeneous catalysts from aqueous solutions. *Catalysis Today* **41**, 3-19 (1998).
158 Rex, A. & Dos Santos, J. The use of Sol–Gel processes in the development of supported catalysts. *J Sol-Gel Sci Technol* **105**, 30-49 (2023).
159 Smeets, V., Ben Mustapha, L., Schnee, J., Gaigneaux, E. M. & Debecker, D. P. Mesoporous SiO2-TiO2 epoxidation catalysts: Tuning surface polarity to improve performance in the presence of water. *Molecular Catalysis* **452**, 123-128 (2018).
160 Van der Verren, M. *et al.* Airborne Preparation of Small Gold Nanoparticles Dispersed on Mesoporous Silica for the Catalytic Oxidation of Glycerol to Dihydroxyacetone. *ACS Applied Nano Materials* **5**, 18977-18985 (2022).
161 Smeets, V. *et al.* Aerosol route to TiO2–SiO2 catalysts with tailored pore architecture and high epoxidation activity. *Chemistry of Materials* **31**, 1610-1619 (2019).
162 Nandiyanto, A. B. D. & Okuyama, K. Progress in developing spray-drying methods for the production of controlled morphology particles: From the nanometer to submicrometer size ranges. *Advanced Powder Technology* **22**, 1-19 (2011).
163 Debecker, D. P., Le Bras, S., Boissière, C., Chaumonnot, A. & Sanchez, C. Aerosol processing: a wind of innovation in the field of advanced heterogeneous catalysts. *Chem. Soc. Rev.* **47**, 4112-4155 (2018).
164 Debecker, D. P. *et al.* One-Pot Aerosol Route to MoO3-SiO2-Al2O3 Catalysts with Ordered Super Microporosity and High Olefin Metathesis Activity. *Angewandte Chemie International Edition* **51**, 2129-2131 (2012).
165 Maksasithorn, S., Praserthdam, P., Suriye, K. & Debecker, D. P. Preparation of super-microporous WO3–SiO2 olefin metathesis catalysts by the aerosol-assisted sol–gel process. *Microporous and Mesoporous Materials* **213**, 125-133 (2015).
166 Pega, S. *et al.* Direct Aerosol Synthesis of Large-Pore Amorphous Mesostructured Aluminosilicates with Superior Acid-Catalytic Properties. *Angewandte Chemie International Edition* **48**, 2784-2787 (2009).
167 Vivian, A., Fusaro, L., Debecker, D. P. & Aprile, C. Mesoporous methyl-functionalized Sn-silicates generated by the aerosol process for the sustainable production of ethyl lactate. *ACS Sustainable Chem. Eng.* **6**, 14095-14103 (2018).
168 Troyano, J. *et al.* Spray-drying synthesis of MOFs, COFs, and related composites. *Accounts of chemical research* **53**, 1206-1217 (2020).
169 Shoinkhorova, T. *et al.* Shaping of ZSM-5-based catalysts via spray drying: effect on methanol-to-olefins performance. *ACS applied materials & interfaces* **11**, 44133-44143 (2019).
170 Paris, C. *et al.* CO2 hydrogenation to methanol with Ga-and Zn-doped mesoporous Cu/SiO2 catalysts prepared by the aerosol-assisted sol-gel process. *ChemSusChem* **13**, 6409-6417 (2020).
171 Kuai, L. *et al.* (Rep, 2015).

172 Hampsey, J. E., Arsenault, S., Hu, Q. & Lu, Y. One-Step Synthesis of Mesoporous Metal− SiO2 Particles by an Aerosol-Assisted Self-assembly Process. *Chemistry of materials* **17**, 2475-2480 (2005).

173 Mitsuka, Y. *et al.* Fabrication of Integrated Copper-Based Nanoparticles/Amorphous Metal–Organic Framework by a Facile Spray-Drying Method: Highly Enhanced CO2 Hydrogenation Activity for Methanol Synthesis. *Angewandte Chemie International Edition* **60**, 22283-22288 (2021).

174 Wintzheimer, S. *et al.* Multifunctional, Hybrid Materials Design via Spray-Drying: Much more than Just Drying. *Advanced Materials*, 2306648 (2023).

175 Debecker, D. P., Hulea, V. & Mutin, P. H. Mesoporous mixed oxide catalysts via non-hydrolytic sol–gel: A review. *Applied Catalysis A: General* **451**, 192-206 (2013).

176 Debecker, D. P. & Mutin, P. H. Non-hydrolytic sol-gel routes to heterogeneous catalysts. *Chem Soc Rev* **41**, 3624-3650 (2012).

177 Skoda, D., Styskalik, A., Moravec, Z., Bezdicka, P. & Pinkas, J. Templated non-hydrolytic synthesis of mesoporous zirconium silicates and their catalytic properties. *J Mater Sci* **50**, 3371-3382 (2015).

178 Styskalik, A. *et al.* The Power of Non-Hydrolytic Sol-Gel Chemistry: A Review. *Catalysts* **7**, 168 (2017).

179 Styskalik, A., Skoda, D., Pinkas, J. & Mathur, S. Non-hydrolytic synthesis of titanosilicate xerogels by acetamide elimination and their use as epoxidation catalysts. *J Sol-Gel Sci Technol* **63**, 463-472 (2012).

180 Mutin, P. H. & Vioux, A. Nonhydrolytic processing of oxide-based materials: simple routes to control homogeneity, morphology, and nanostructure. *Chemistry of Materials* **21**, 582-596 (2009).

181 Saltarelli, M. *et al.* Aminoiron(III)–porphyrin–alumina catalyst obtained by non-hydrolytic sol-gel process for heterogeneous oxidation of hydrocarbons. *Molecular Catalysis* **462**, 114-125 (2019).

182 Capeletti, L. B., Alves, M. d. C. M., Cardoso, M. B. & dos Santos, J. H. Z. Hybrid silica based catalysts prepared by the encapsulation of zirconocene compound via non-hydrolytic sol-gel method for ethylene polymerization. *Applied Catalysis A: General* **560**, 225-235 (2018).

183 Bilecka, I. & Niederberger, M. New developments in the nonaqueous and/or non-hydrolytic sol–gel synthesis of inorganic nanoparticles. *Electrochimica Acta* **55**, 7717-7725 (2010).

184 Bourget, L., Corriu, R., Leclercq, D., Mutin, P. & Vioux, A. Non-hydrolytic sol–gel routes to silica. *Journal of Non-Crystalline Solids* **242**, 81-91 (1998).

185 Styskalik, A. *et al.* Hybrid mesoporous aluminosilicate catalysts obtained by non-hydrolytic sol–gel for ethanol dehydration. *Journal of Materials Chemistry A* **8**, 23526-23542 (2020).

186 Hradsky, D. *et al.* Catalytic performance of micro-mesoporous zirconosilicates prepared by non-hydrolytic sol-gel in ethanol-acetaldehyde conversion to butadiene and related reactions. *Applied Catalysis A: General* **652**, 119037 (2023).

187 Skoda, D. *et al.* Novel non-hydrolytic templated sol–gel synthesis of mesoporous aluminosilicates and their use as aminolysis catalysts. *RSC Advances* **6**, 24273-24284 (2016).
188 Skoda, D. *et al.* Mesoporous SnO2–SiO2 and Sn–silica–carbon nanocomposites by novel non-hydrolytic templated sol–gel synthesis. *RSC advances* **6**, 68739-68747 (2016).
189 Bouchmella, K., Stoyanova, M., Rodemerck, U., Debecker, D. P. & Hubert Mutin, P. Avoiding rhenium loss in non-hydrolytic synthesis of highly active Re–Si–Al olefin metathesis catalysts. *Catalysis Communications* **58**, 183-186 (2015).
190 Maksasithorn, S., Praserthdam, P., Suriye, K., Devillers, M. & Debecker, D. P. WO3-based catalysts prepared by non-hydrolytic sol-gel for the production of propene by cross-metathesis of ethene and 2-butene. *Applied Catalysis A: General* **488**, 200-207 (2014).
191 Lafond, V., Mutin, P. & Vioux, A. Non-hydrolytic sol–gel routes based on alkyl halide elimination: Toward better mixed oxide catalysts and new supports: Application to the preparation of a SiO2–TiO2 epoxidation catalyst. *Journal of Molecular Catalysis A: Chemical* **182**, 81-88 (2002).
192 Cojocariu, A. M. *et al.* Non-hydrolytic synthesis of mesoporous silica–titania catalysts for the mild oxidation of sulfur compounds with hydrogen peroxide. *Chemical Communications*, 5357-5359 (2008).
193 Hamden, Z. *et al.* In situ generation of TiO2 nanoparticles using chitosan as a template and their photocatalytic activity. *Journal of Photochemistry and Photobiology A: Chemistry* **321**, 211-222 (2016).
194 Barbieri, F. *et al.* Mixed-oxide catalysts involving V, Nb and Si obtained by a non-hydrolytic sol–gel route: preparation and catalytic behaviour in oxydative dehydrogenation of propane. *Catalysis today* **61**, 353-360 (2000).
195 Nadji, L. *et al.* Gas phase dehydration of glycerol to acrolein over WO 3-based catalysts prepared by non-hydrolytic sol–gel synthesis. *RSC advances* **8**, 13344-13352 (2018).
196 Héroguel, F., Silvioli, L., Du, Y.-P. & Luterbacher, J. S. Controlled deposition of titanium oxide overcoats by non-hydrolytic sol gel for improved catalyst selectivity and stability. *Journal of Catalysis* **358**, 50-61 (2018).
197 Van der Verren, M. *et al.* Bifunctional Au-Sn-SiO2 catalysts promote the direct upgrading of glycerol to lactates. (2023).
198 Balthis, J., Rochow, E. & White, D. Silicon Tetraacetate. *Inorganic Syntheses* **4**, 45-47 (1953).
199 Bradley, D. C. & Thomas, I. M. METALLO-ORGANIC COMPOUNDS CONTAINING METAL–NITROGEN BONDS: PART III. DIALKYLAMINO COMPOUNDS OF TANTALUM. *Canadian Journal of Chemistry* **40**, 1355-1360 (1962).
200 Wakuda, D., Hatamura, M. & Suganuma, K. Novel method for room temperature sintering of Ag nanoparticle paste in air. *Chemical Physics Letters* **441**, 305-308 (2007).
201 Tuler, F. E., Gaigneaux, E. M., Miró, E. E., Milt, V. G. & Debecker, D. P. Catalytic ceramic papers for diesel soot oxidation: A spray method

for enhanced performance. *Catalysis Communications* **72**, 116-120 (2015).

202 Jacquemin, M., Genet, M. J., Gaigneaux, E. M. & Debecker, D. P. Calibration of the X-Ray Photoelectron Spectroscopy Binding Energy Scale for the Characterization of Heterogeneous Catalysts: Is Everything Really under Control? *ChemPhysChem* **14**, 3618-3626 (2013).

203 Styskalik, A. *et al.* Highly porous hybrid metallosilicate materials prepared by non-hydrolytic sol-gel: hydrothermal stability and catalytic properties in ethanol dehydration. *Microporous and Mesoporous Materials*, 110028 (2020).

204 Debecker, D. P. *et al.* First acidic macro-mesocellular aluminosilicate monolithic foams "SiAl (HIPE)" and their catalytic properties. *Chemical Communications* **51**, 14018-14021 (2015).

205 Phung, T. K. & Busca, G. Ethanol dehydration on silica-aluminas: Active sites and ethylene/diethyl ether selectivities. *Catalysis Communications* **68**, 110-115 (2015).

206 Beganskienė, A., Sirutkaitis, V., Kurtinaitienė, M., Juškėnas, R. & Kareiva, A. FTIR, TEM and NMR investigations of Stöber silica nanoparticles. *Mater Sci (Medžiagotyra)* **10**, 287-290 (2004).

207 Majewski, A. J., Wood, J. & Bujalski, W. Nickel–silica core@ shell catalyst for methane reforming. *International journal of hydrogen energy* **38**, 14531-14541 (2013).

208 Wang, X.-D. *et al.* Preparation of spherical silica particles by Stöber process with high concentration of tetra-ethyl-orthosilicate. *Journal of colloid and interface science* **341**, 23-29 (2010).

209 Singh, L., Agarwal, S., Bhattacharyya, S., Sharma, U. & Ahalawat, S. Preparation of silica nanoparticles and its beneficial role in cementitious materials. *Nanomaterials and Nanotechnology* **1**, 9 (2011).

210 Lehmann, T. *et al.* Physico-chemical characterization of Ni/MCM-41 synthesized by a template ion exchange approach. *Microporous and Mesoporous Materials* **151**, 113-125 (2012).

211 Blanc, D., Zhang, W., Massard, C. & Mugnier, J. Synthesis and characterisation of tantalum-incorporating silica hybrid sol–gel thin films for optical applications. *Optical Materials* **28**, 331-335 (2006).

212 Ko, Y. S. & Ahn, W. S. Synthesis and characterization of tantalum silicalite molecular sieves with MFI structure. *Microporous and mesoporous materials* **30**, 283-291 (1999).

213 Li, X. *et al.* Conversion of ethanol to 1, 3-butadiene over high-performance Mg–ZrO x/MFI nanosheet catalysts via the two-step method. *Green Chem.* **22**, 2852-2861 (2020).

214 Hradsky, D. *et al.* Catalytic Performance of Micro-Mesoporous Zirconosilicates Prepared by Non-Hydrolytic Sol-Gel in Ethanol-To-Butadiene Transformation and Related Reactions. *ChemRxiv* (2022).

215 Janssens, W. *et al.* Ternary Ag/MgO-SiO2 Catalysts for the Conversion of Ethanol into Butadiene. *ChemSusChem* **8**, 994-1008 (2015).

216 Godard, N. *et al.* High-Yield Synthesis of Ethyl Lactate with Mesoporous Tin Silicate Catalysts Prepared by an Aerosol-Assisted Sol–Gel Process. *ChemCatChem* **9**, 2211-2218 (2017).

217 Zheng, A., Huang, S.-J., Liu, S.-B. & Deng, F. Acid properties of solid acid catalysts characterized by solid-state 31P NMR of adsorbed phosphorous probe molecules. *Phys. Chem. Chem. Phys.* **13**, 14889-14901 (2011).

218 Leonova, L. *et al.* Hydrophobicity Boosts Catalytic Activity: The Tailoring of Aluminosilicates with Trimethylsilyl Groups. *ChemCatChem* **15**, e202300449 (2023).

219 García-Sánchez, J. T. *et al.* Calculation of Mass Transfer Limitations for a Gas-Phase Reaction in an Isothermal Fixed Bed Reactor: Tutorial and Sensitivity Analysis. *ACS Catal.* **13**, 6905-6918 (2023).

220 Shan, J. *et al.* Selective non-oxidative dehydrogenation of ethanol to acetaldehyde and hydrogen on highly dilute NiCu alloys. *Applied Catalysis B: Environmental* **205**, 541-550 (2017).

221 Pang, J. *et al.* Hierarchical echinus-like Cu-MFI catalysts for ethanol dehydrogenation. *ACS Catal.* **10**, 13624-13629 (2020).

222 Styskalik, A., Abbott, J. G., Orick, M. C., Debecker, D. P. & Barnes, C. E. Synthesis, characterization and catalytic activity of single site, Lewis acidic aluminosilicates. *Catalysis Today* **334**, 131-139 (2019).

223 Skoda, D. *et al.* Mesoporous titanosilicates by templated non-hydrolytic sol–gel reactions. *J Sol-Gel Sci Technol* **74**, 810-822 (2015).

224 Yurdakal, S., Garlisi, C., Özcan, L., Bellardita, M. & Palmisano, G. in *Heterogeneous photocatalysis* 87-152 (Elsevier, 2019).

225 Dochain, D. D., Van Den Daelen, A., Styskalik, A., Vykoukal, V. & Debecker, D. P. Aerosol-assisted sol–gel synthesis of mesoporous Ag–Ta–SiO 2 catalysts for the direct upgrading of ethanol to butadiene. *RSC Sustainability* (2023).

226 Styskalik, A., Vykoukal, V., Fusaro, L., Aprile, C. & Debecker, D. P. Mildly acidic aluminosilicate catalysts for stable performance in ethanol dehydration. *Applied Catalysis B: Environmental* **271**, 118926 (2020).

227 Bouchmella, K. *et al.* Olefin metathesis with mesoporous rhenium–silicium–aluminum mixed oxides obtained via a one-step non-hydrolytic sol–gel route. *Journal of Catalysis* **301**, 233-241 (2013).

228 Simpson, R., White, R. G., Watts, J. F. & Baker, M. A. XPS investigation of monatomic and cluster argon ion sputtering of tantalum pentoxide. *Applied Surface Science* **405**, 79-87 (2017).

229 Arnould, C. *et al.* Titanium modified with layer-by-layer sol–gel tantalum oxide and an organodiphosphonic acid: A coating for hydroxyapatite growth. *Journal of colloid and interface science* **336**, 497-503 (2009).

230 Dzwigaj, S., Millot, Y. & Che, M. Ta (V)-single site BEA zeolite by two-step postsynthesis method: preparation and characterization. *Catal Lett* **135**, 169-174 (2010).

231 Cordeiro, P. J. & Tilley, T. D. Enhancement of epoxidation efficiencies for Ta-SBA15 catalysts. The influence of modification with–EMe3 (E= Si, Ge, Sn) groups. *Langmuir* **27**, 6295-6304 (2011).

232 Kondo, J. N. *et al.* IR characterization of mesoporous tantalum oxide, Ta-TMS-1. *Bulletin of the Chemical Society of Japan* **73**, 1123-1129 (2000).

233 Schumann, J., Kröhnert, J., Frei, E., Schlögl, R. & Trunschke, A. IR-spectroscopic study on the interface of Cu-based methanol synthesis catalysts: evidence for the formation of a ZnO overlayer. *Topics in Catalysis* **60**, 1735-1743 (2017).

234 Jiménez-Morales, I., Santamaría-González, J., Maireles-Torres, P. & Jiménez-López, A. Methanolysis of sunflower oil catalyzed by acidic Ta2O5 supported on SBA-15. *Applied Catalysis A: General* **405**, 93-100 (2011).